ABSTRACT

Title of dissertation: DRAG AND NOISE REDUCTION
OF FLATBACK AIRFOIL
BY SPAN-WISE WAVY TRAILING EDGE

Seung Joon Yang
Doctor of Philosophy, 2019

Dissertation directed by: Professor James D. Baeder
Department of Aerospace Engineering

The flatback airfoil is a promising idea for future large wind turbine blade structure design; however, it causes notable drag increase and low frequency tonal noise due to the presence of span-wise coherent standing flow and Karman vortex shedding at the trailing edge. Current dissertation proposes a span-wise wavy trailing edge design as a solution to flatback airfoil drag and noise, and provides relevant CFD results. Proposed span-wise wavy trailing edge prevents the span-wise coherent standing flow and vortex shedding, and results in a decrease of the tonal noise and pressure drag of the airfoil. Delayed Detached Eddy Simulation is employed in HPC environments. In-house developed N-S solvers, OVERTURNS (CPU-based) and GPURANS3D (GPGPU) are used for the computation.

A design parametric study for the span-wise wavy trailing edge is conducted in the first half of the dissertation. Aerodynamic and aeroacoustic performance of a particular flatback airfoil (FB3500-1750, t_{TE} is 17.5% of a chord length) and various span-wise wavy trailing edge modifications are investigated, regarding the influence

of the major wave design parameters. A total of 16 design variations of the wavy trailing edge are investigated. For a Reynolds number 666,000 and Mach number 0.3, the best trailing edge wave design is a combination of the less portion - more than 0.25c length - shallow wave depth; the best design reduces 60% (maximum) of the flatback airfoil with only 7% lift loss, and results in about 150% (maximum) of lift/drag ratio increase. Measured tonal noise is also reduced by about 20-25dB(SPL) with the best performance design.

In the second half of the dissertation, the isolated rotor simulation is performed for a straight-flat trailing edge wind turbine blade and its wavy trailing edge modification. In the simulation, the Blunt-Wavy trailing edge (a combination of *te* augmentation and wavy modification) is proposed and applied at the inboard of baseline blade (SNL100-03FB). Applying the best performance wavy design, overall turbine power generation is increased by 2.62% and tonal noise is decreased by 5-15dB.

DRAG AND NOISE REDUCTION OF FLATBACK AIRFOIL BY SPAN-WISE WAVY TRAILING EDGE

by

Seung Joon Yang

Dissertation submitted to the Faculty of the Graduate School of the
University of Maryland, College Park in partial fulfillment
of the requirements for the degree of
Doctor of Philosophy
2019

Advisory Committee:
Professor James D. Baeder, Chair/Advisor
Professor Inderjit Chopra
Professor Kenneth H. Yu
Professor Christopher P. Cadou
Professor James H. Duncan, Dean's Representative

Acknowledgments

I owe my gratitude to all the people who have made this study possible.

First, I'd like to thank my advisor, Professor James Baeder for giving me an invaluable opportunity to work on this exciting project over the past few years. Most part of the work is strongly inspired by him, and he has never hesitated sharing his great insights and advices with me when I was stuck in the research obstacles. It has been a pleasure to work with and learn from such an extraordinary individual.

I would also like to thank Professor Inderjit Chopra, Professor Anubhav Datta, Professor Kenneth Yu, Professor Christoper Cadou and Professor James Duncan for agreeing to serve on my thesis committee and for giving me great instructions and advices.

My colleagues at the UMD Aerospace Engineering have enriched my graduate life in many ways and deserve a special mention. Camli Badrya and Nishan Jain, they are the oldest friends of mine at the school, and helped me a lot to start as a rotorcraft CFD enginner. Chatting and drink with two Korean geniuses, Yong-Su Jung and Bum-Seok Lee was always the best time and they made me homesick-free. Soon to be PhDs in the Baeder's group, Dylan Jude, Vera Klimchenko, Alex Costanoble, they are perfect examples how the top-notch PhD students can work efficiently and excellently without loosing their beautiful smile. I also learned a lot from two part-time PhDs, but also full-time professional engineers (or scientists), Ryan Catlett and Jon Holland.

I owe my deepest thanks to my family - my mother and father who have always

stood by me, supported me and protected me through my entire life. Any human word won't be enough to express the gratitude I owe my mom and dad. My mom always knew what I have in my mind, and always understand me. My dad, he has been and will be my greatest supporter. I truly thank to him for being my mountain climbing friend when I was a young child, and playing soccer / baseball with me when I was an elementary school boy, and playing basketball with me as I'm in a high school, and now being the best golf buddy of mine.

I also owe my special thanks to my mother and father in law. They gave me a perfect trust and support, so that I can walk forward to my career even though I haven't been a best husband and son in law of their precious little one and themselves. I would also like to thank my only sister and brother in law. It was another God's present to have them in Philly which is just 2 hours driving distance away from the school.

Lastly, I am truly thank to my lovely wife, Janice and beautiful children, Zoe and Eden who are walking on the road of life together with holding my hands. You are all of my life in the present, tomorrow and forever.

I would like to acknowledge financial support from the State of Maryland (MHEC/MEA program) for all the projects discussed herein.

Thank you all and thank God!

Dedication

To Uri-halmooni, Ms. Sim Eun-Taek who always be with me.

Table of Contents

List of Tables

List of Figures

List of Abbreviations

AoA	Angle of Attack
APG	Adverse Pressure Gradient
BDF	Backward Differentiation Formula
BEM	Blade Element Method
BTE	Blunt Trailing Edge
BWC	Blunt-Wavy Combined
CFD	Computational Fluid Dynamics
CUDA	Compute Unified Device Architecture
DADI	Diagonal Alternating Direction Implicit
DDES	Delayed Detached Eddy Simulation
DES	Detached Eddy Simulation
DNS	Direct Numerical Simulation
DOE	Department of Energy
FVM	Finite Volume Method
GIS	Grid Induced Separation
GPU	Graphics Processing Unit
HAWT	Horizontal Axis Wind Turbine
LBL	Laminar Boundary Layer
LE	Leading Edge
LES	Large Eddy Simulation
LUSGS	Lower-Upper Symmetric Gauss Seidel
MPI	Message Passing Interface
MSD	Modeled-Stress Depletion
MUSCL	Monotonic Upwind Scheme for Conservation Laws
NREL	National Renewable Energy Laboratory
N-S	Navier-Stokes
PDE	Partial Deferential Equation
RANS	Reynolds Averaged Navier-Stokes

SA	Spalart-Allmaras turbulent model
SGS	Sub-Grid Scale
SNL	Sandia National Laboratory
SPL	Sound Pressure Level, dB (reference Pressure: 20 μPa)
SST	Shear Stress Transport
STP	Standard Temperature and Pressure
TBL	Turbulent Boundary Layer
TE	Trailing Edge
VAWT	Vertical Axis Wind Turbins
VS	Vortex Shedding
WENO	Weighted Essentially Non-Oscillatory

Chapter 1: Introduction

1.1 Modern Wind Turbines

1.1.1 Size of Future Wind Turbines

The most distinguishing character of modern wind turbines may be their gigantic sizes. From the beginning, their size has been growing continuously. According to the DOE (Department of Energy) report published in 2017, the average rotor diameter has grown by a factor of two during the last two decades in the US [1]. The trend is very well described in the following two graphs from the report. As seen in Figure 1.1, the average rotor diameter of US commercial turbines was only 50 meter in 1998, but it became around 110 meter in the last year. In Figure 1.2, the portion of US commercial turbines larger than 100meter diameter was only less than 10% in 2010. six years later, more than 90% of the commercial turbines have an over 100meter diameter rotor.

In the near future, rotor sizing up will be even more dramatic. Many of new turbine blade development projects are targeting more than 200meter diameter today. In the US, the SNL (Sandia National Laboratory) has developed a deign for an 100meter radius blade for [2]. Similarly in Europe, a 102meter radius blade

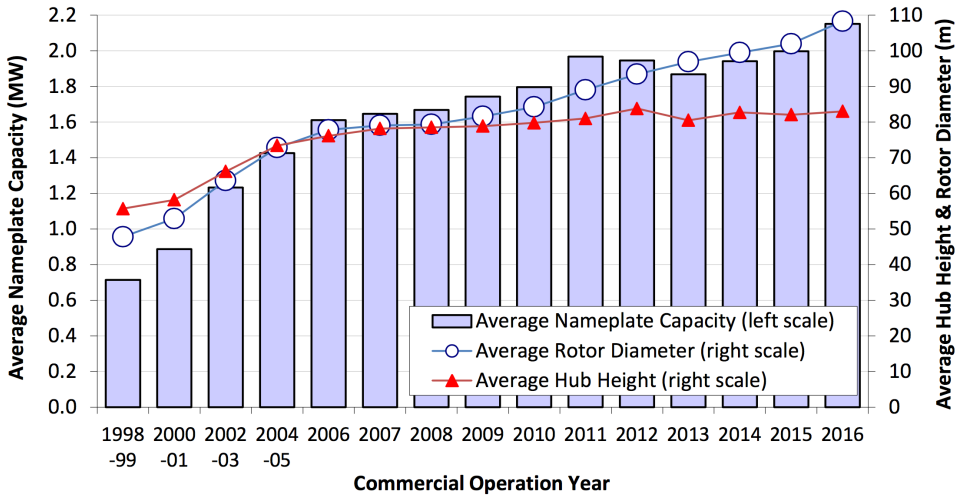

Figure 1.1: History of turbine nameplate capacity, hub height, and rotor diameter, Courtesy of Report: R.Wiser and M.Bolinger, "2016 Wind Technologies Market Report:Summary", Office of Energy Efficiency and Renewable Energy, U.S. Department of Energy [1]

is being investigated as a part of the AVATAR project [3]. Most recently, in the spring of 2018, GE Renewable Energy announced their plan for a future turbine, which features a 107meter length blade manufactured by LM Wind Power [4]. These turbines are twice as larger as current average commercial turbines, and will produce multi mega watts of power.

1.1.2 Large Mass of Large Wind Turbine Blade

One of the most challenging design tasks in the development of future large blades must be the structure design. According to the classic wind turbine design theories, a relation between the blade length - area - mass follows the square-cube law. It means the blade will have 8 times larger mass when the blade length is extended by twice. Recent innovative breakthroughs of airfoil designs and the use of

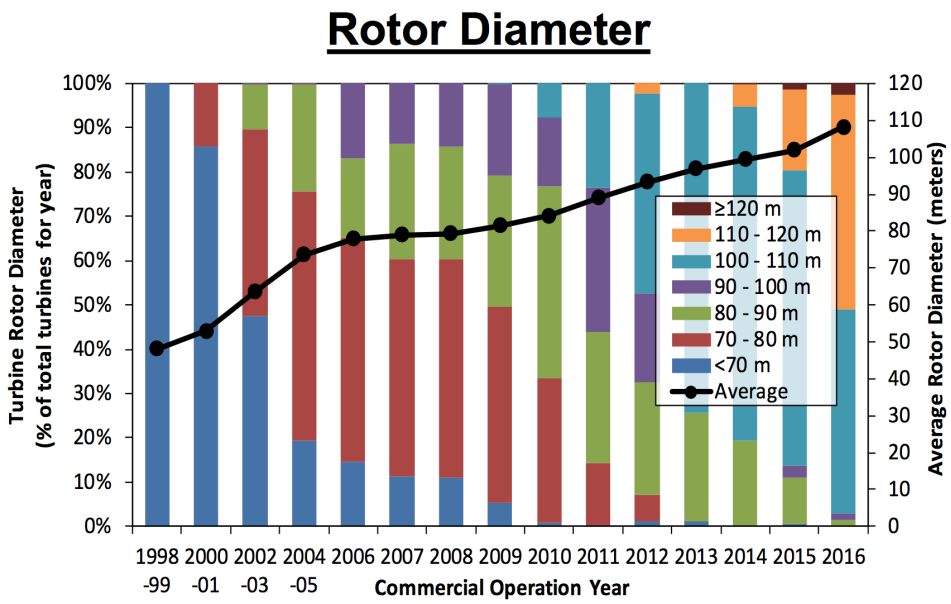

Figure 1.2: Growth in rotor diameter for modern turbines, Courtesy of Report: R.Wiser and M.Bolinger, "2016 Wind Technologies Market Report:Summary", Office of Energy Efficiency and Renewable Energy, U.S. Department of Energy [1]

new materials, has meant that the theory is not exactly correct for modern turbines. However, it is still valid for most larger blade designs, and it is true that the mass increase is one of the most serious concerns in larger blade designs.

Here is an example of the weight increase of the modern wind turbine blade. In Table 1.1, mass and size of two Siemens blades are compared. 53meter long, B53 blade weighs approximately 10tons, but 75meter long, B75 blade weighs about 25tons. Approximately 1.4 times longer length made the blade 2.5 times heavier in this case. Again, it is not exactly valid with the classic square-cube law, but it is still a large amount of mass increase.

Table 1.1: Comparison between the Siemens B53 and B75

Type	Blade length (m)	Rotor sweep area (m^2)	Blade weight (ton)
Siemens B53	53	91,50	approx. 10
Siemens B75	75	18,600	approx. 25

1.1.3 Thick Airfoils for Modern Wind Turbine Blade Root

A wind turbine rotor blade is structurally similar to the cantilever beam [5]. Thus, the stress and bending moments are the maximum at the blade root and inboard. For this reason, modern large wind turbine blades use relatively thick airfoils for their inboard design. Examples of the thick airfoils are presented in Figure 1.3. Thickness of these airfoils (developed by F. Grasso [6]) are about 34 - 40% of chord length; these are extremely thick compared to typical airfoils. In recent blade design, use of these thick airfoils are getting more popular for commercial

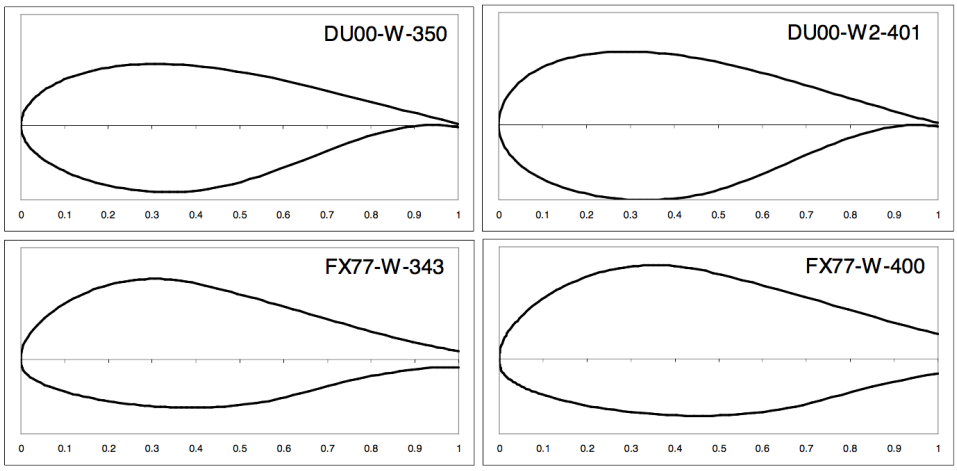

Figure 1.3: Examples of thick airfoil designs for modern wind turbine blade inboard, Courtesy of F. Grasso, "Development of Thick Airfoils for Wind Turbines," 50th AIAA Aerospace Meeting, Nashville, TN, 2012 [6]

turbine blades.

Use of the thick airfoils enhances structural strength and increases the airfoil lift at the blade inboard. Their larger leading edge radius and thickness increase the lift of airfoil especially at high angles of attack. And generally the separation curve is much smoother compared to the thin airfoils. In Figure 1.4, an example of the thick airfoil aerodynamics(published by A. Munoz et al [7]) is presented. The DU97-W-350 airfoil (cyan) is one of the most popular thick airfoils which is often used in the modern turbine blade inboard design. The DU95-W-180 (blue) is also a popular airfoil, but it tends to be used more in the outboard design. The lift curves of both airfoils are similar with each other until the moderate angle of attacks, but the thick airfoil produces more lift than the thin airfoil near the separation curve. There is a small increase of the drag because of the thicker profile of the airfoil.

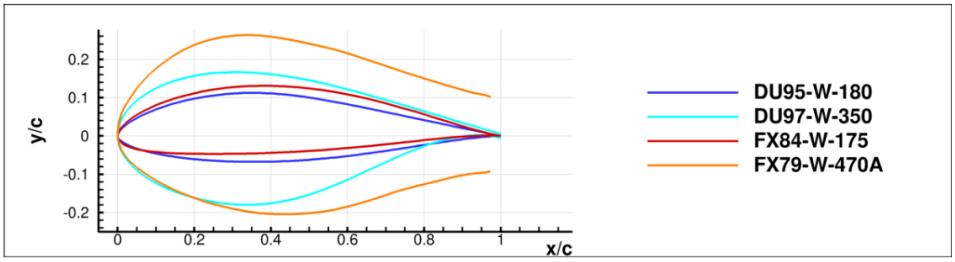

(a) Geometry

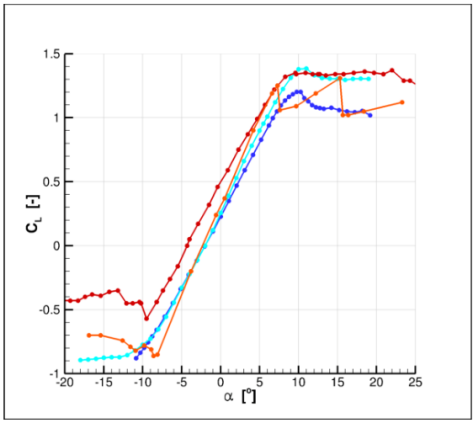

(b) Experimental C_L vs α

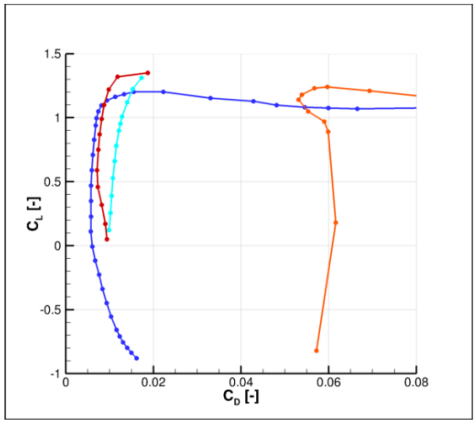

(c) Experimental C_L vs C_D

Figure 1.4: Comparison of aerodynamic performance between thick and thin airfoils, Courtesy of A. Munoz et al, "Thick airfoil designs for the root of the 10MW INNWIND.EU wind turbine," Journal of Physics: Conference Series 753 022046 (2016) [7]

However, using thick airfoils may increase blade weight a lot. For an example, airfoil thickness and mass distribution of the NREL 5MW(63meter long) are presented in Table 1.2 and Figure 1.5 [8, 9]. For this case, about 32% of blade fraction is consisted with thick airfoils which thicknesses are more than 35% t/c. Because of the thick (or even cylinder) airfoils, the blade mass is much larger at the inboard compared to the outboard.

Table 1.2: Span-wise airfoil thickness distribution of the NREL 5MW blade [9]

Airfoil Designation	Thickness(t/c)	Begin Radius(m)	End Radius(m)
Cylinder1	100%	1.8	5.98
Cylinder2	100%	5.98	10.15
DU40-A17	40.5%	10.15	15.00
DU35-A17	35.09%	15.00	20.49
DU30-A17	30%	20.49	26.79
DU25-A17	25%	26.79	34.22
DU21-A17	21%	34.22	42.47
NA64-A17	18%	42.47	64.50

1.1.4 Blade Mass Reduction

As it mentioned in the section 1.1.2, in the modern turbines, blade mass doesn't exactly follow the square-cube law today by efforts of the blade design innovations. Most effective way to reduce the blade mass is to use advanced material. For an example, use of carbon fiber, instead of glass fiber materials, reduces the blade mass very much. According to the recent Sandia Report [2], use of the carbon fiber reduces the weight of Sandia 100meter blade by 35%, and additional 13% of the mass is reduced by use of the advanced core material.

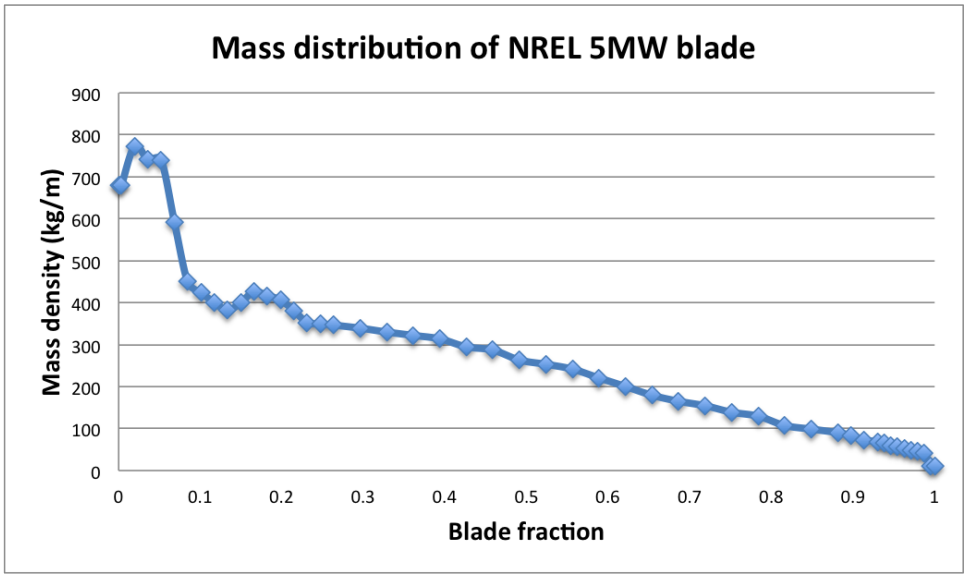

Figure 1.5: Mass distribution of the NREL 5MW blade [8]

Another wavy to reduce the mass is to use advanced airfoil design. Comprehensive studies of the airfoil geometries can make the blade much slender, and the much slender blade is obviously much lighter. Flatback airfoil is a good example of the advanced airfoil to use for the mass reduction. In the previous Sandia Report [2], use of the flatback airfoil reduces blade mass approximately 10tons. In Figure 1.6 and 1.7, the slender version of the Sandia 100meter blade designed with the flatback airfoil (for Figure 1.7, Rev1 and 2 in the legends) is presented, and the Sandia 100 meter blade mass reduction through this design processes is presented in Table 1.3 as well. In his research, the chord length of the new version of the SNL 100 meter blade is much reduced compared to the previous version of the SNL blade (SNL100-00 and 02). This re-design process includes structural and aerodynamic optimizations, and reduces about 10tons of blade mass by reducing the blade chord

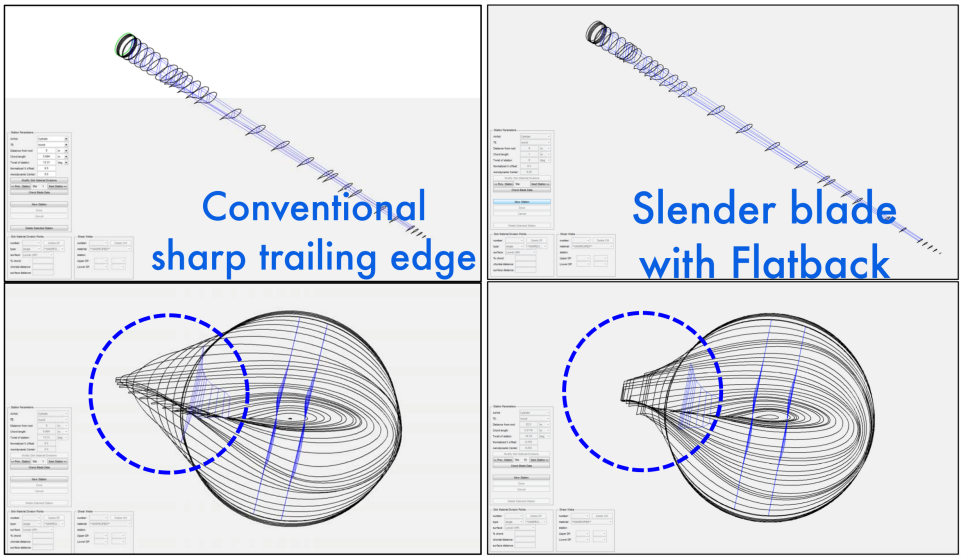

Figure 1.6: Blade chord difference by applying flatback airfoil, edited images courtesy of T. Griffith [2]

length as shown in Figure 1.17.

Table 1.3: Sandia 100meter blade mass reduction by advanced materials and airfoil geometries [2]

Blade	Technique	Blade weight (ton)
SNL100-00	All glass material	114
SNL100-01	Carbon fiber	74
SNL100-02	Advanced core material	59
SNL100-03	Advanced Geometry(Flatback)	49

1.2 Flatback Airfoil for Wind Turbine Blade Design

Flatback airfoil is a type of a blunt trailing edge airfoil, and it is one of innovative idea in the modern wind turbine blade design. As we mentioned in the previous section, the flatback airfoil can make a blade much slender, and consequently helps

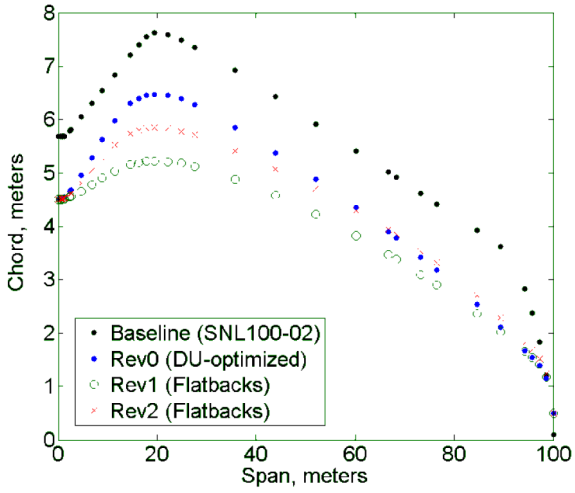

Figure 1.7: Blade chord reduction of SNL 100 meter blade series by flatback airfoils, edited images courtesy of T. Griffith [2]

to reduce blade mass. However, its aerodynamic efficiency might be controversial. In the past researches, it has been revealed that the flatback airfoil helps to delay the flow separation onset and increases the airfoil lift. However it also increases the airfoil drag as well.

In fact, drag increase of the blunt trailing edge had been found in 1950-60s. Comprehensive studies of the blunt trailing edge had been conducted by many researchers such as Roshko [10, 11], Nash [12, 13], and Hoerner [14]. More recently, aerodynamics of thick and blunt trailing edge airfoils have been mainly focused for the wind turbine application, and various research groups have worked for this topic. Remarkable common results of the recent studies are an increase of pressure drag and Karman-like trailing edge vortex shedding. The research history of the flatback airfoil is presented in Table 1.4.

Table 1.4: Research history of the flatback airfoil

Flatback airfoils	National Physics Lab. Nash et al. (experimental)	First comprehensive study about base drag	1960
	Ohio State / NASA / DOE Law, Gregorek (experimental)	First truncated NACA 64-621 (flatback airfoil)	1987
	UC-Davis C.P.vanDam, Standish, Chao, Baker (experimental & CFD)	Blunt trailing edge modification on various thick airfoils Blunt trailing edge modification on the NREL phase 6 rotor UC-Davis: Wind turnnel tests / CFD	2003 2007 2008 2010
	Virginia Tech / Sandia National Lab. / DOE Devenport, Burdisso, Barone, Berg (experimental & CFD)	Blunt trailing edge modification on the DU97-W-300 Virginia Tech: Wind tunnel tests (<Re 3,000,000) Sandia Lab: Field tests (blunt trailing edge SNL BSDS rotor)	2010
	Washington University in St.Louis Chen, Agarwal (CFD)	Optimization of blunt trailing edge	2012
	UC-Davis Chow, C.P. vanDam (CFD)	Blunt trailing edge moficiation on the NREL 5MW rotor	2012
	Sandia National Lab. Griffith et al. (Conceptual Design)	Conceptual design of 100m length flatback blade (SNL100-03FB)	2014
	Siemense Obrecht et al. (experimental)	Industrial level blunt trailing edge field test (SWT-2.3-108)	2015

Figure 1.8 is an example of comparisons between a thick airfoil and its flatback version. The FB3500-0050 airfoil is designed with 35% t/c of airfoil thickness, and 0.5% t_{te}/c of trailing edge thickness, where the t is airfoil thickness, t_{te} is trailing edge thickness, and c is airfoil chord length. The FB3500-1750 airfoil is a flatback version of the FB3500-0050. The airfoil thickness is same as the FB3500-0050, but its trailing edge thickness is 17.5% t_{te}/c.

Lift and drag of the airfoils are compared in Figure 1.9. The experimental results (blank markers) are obtained in the wind tunnel test conducted by Baker and van Dam [15]. The DDES results (solid markers) are the authors own simulation. The test was performed in a Reynold number 666,000 and a Mach number 0.3. The augmented trailing edge increases the lift, but the drag as well. At the moderate angle of attack (8-12°), the lift increases by 50%. However, the drag increases more than 3 times in the particular case. The major source of the drag increase is a pressure drag rise caused by a flow recirculation at the augmented trailing edge. In Figure 1.10, massive flow recirculation of the flatback trailing edge airfoil is presented.

1.3 Modern Wind Turbine Noise

1.3.1 Influences of Wind Turbine Noise

The environmental effect of wind turbine noise might be a controversial. The wind turbine noise is usually in very low frequencies. Depending on the turbine size, rotation speed and machine system, it is audible or sometimes infra-sound. Any type

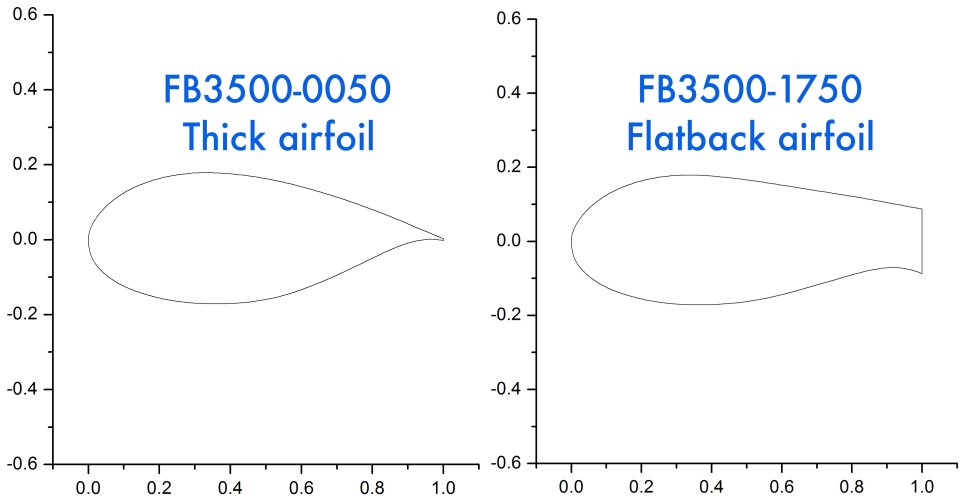

Figure 1.8: Comparison of airfoil coordinates between FB3500-0050 and FB3500-1750

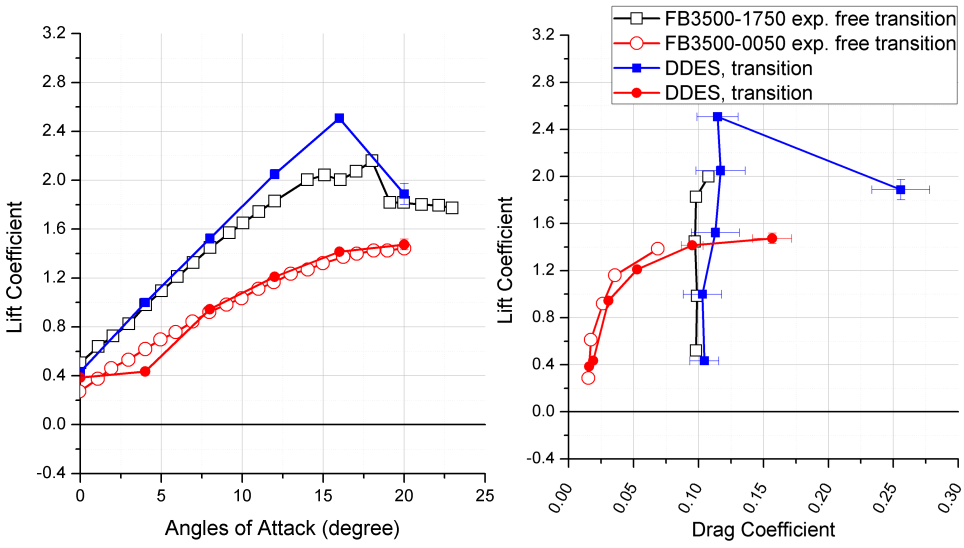

Figure 1.9: Lift and Drag polar of the FB3500-0050 and the FB3500-1750; Experiment by J.P. Baker et al [15]

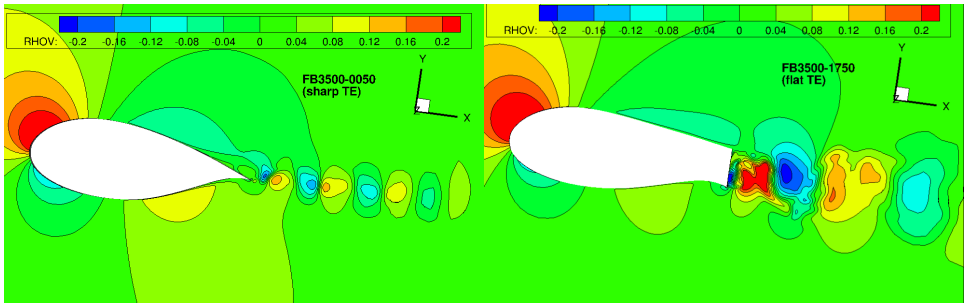

Figure 1.10: Comparison of trailing edge vortex shedding between the FB3500-0050 and the FB3500-1750 at the angles of attack 8°

of wind turbines are much more tranquil than other fossil fuel power stations.

However, the wind turbine noise has been one of big concerns for the every wind farm projects so far. Negative effects on the households and other environments caused by the wind turbine noise have been repeatedly reported nearby wind farms [16]. For example, its low frequency noise can affect to the human body or can be harmful to sea mammals for the offshore case. In UK, experiences of sleep disturbances and life quality reductions have been reported from the residents nearby wind farms. And the wind turbine noise was suspected as a reason [17]. These support a claim that wind turbine noise reduction technique should be accompanied for the future wind turbine design.

1.3.2 Sources of Wind Turbine Noise

The wind turbine noise can be categorized with two major sources; mechanical noises from a nacelle and aero-acoustic noise from rotor blades (as shown in Figure 1.11). Most usually, the mechanical noise is louder than the aero-acoustic noise of

the blades. Most of the mechanical noise is generated by a generator or gearbox in a nacelle. This is sometimes tonal and low-frequency noise, and not related with blade design [18]. The aero-acoustic noise is usually much lower frequency than the mechanical noise. And it might be low frequency 'whooshing' sound when it becomes tonal noise. This is sometimes more annoying sound, while people feels the mechanical noise more likely common electric home appliances.

The sources of the blade acoustic noise are; inflow turbulence, tip vortex, flow separation, boundary layer instability, and trailing edge vortex. These can be explained by airfoil self noises as shown in Figure 1.12.

1.3.3 Airfoil Self-Noise

Types of the airfoil self-noise are explained in detail by Brooks et al [19]. The airfoil self-noise can be categorized with; 1.turbulent boundary layer - trailing edge (TBL-TE) noise, 2.laminar boundary layer - vortex shedding (LBL-VS) noise, 3.blunt trailing edge (BTE) noise, and 4.tip noise. The TBL-TE noise is causes by interaction between the turbulent boundary layer and trailing edge wakes. Depending on the angle of attack, it becomes more flow separation dominant noise as shown in the Figure 1.12. Characteristics of the LBL-VS and the BTE noise are similar. Trailing edge vortex shedding may involves in the cases of both noises. Thus, it can be a tonal sound depending on the vortex frequency and magnitude. Lastly, the tip noise is caused by the blade tip vortex, and it is usually higher frequency band.

At tip of the wind turbine blade, the tip noise is dominant. At the mid-board

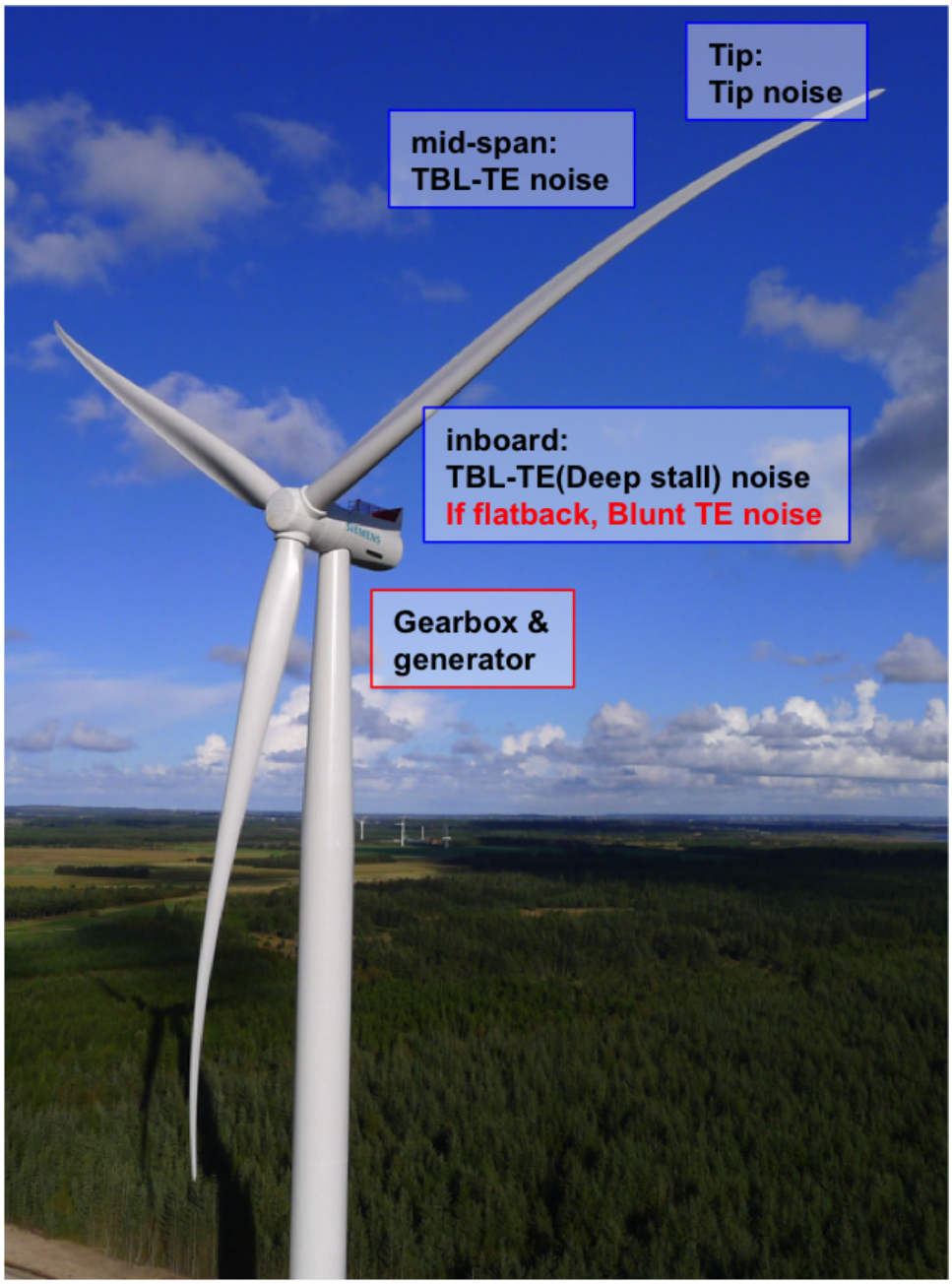

Figure 1.11: Major wind turbine noise sources; background image is the Siemense SWP-8.0-154 with B75 blade wind turbine, edited image courtesy of Siemense Renewable Energy

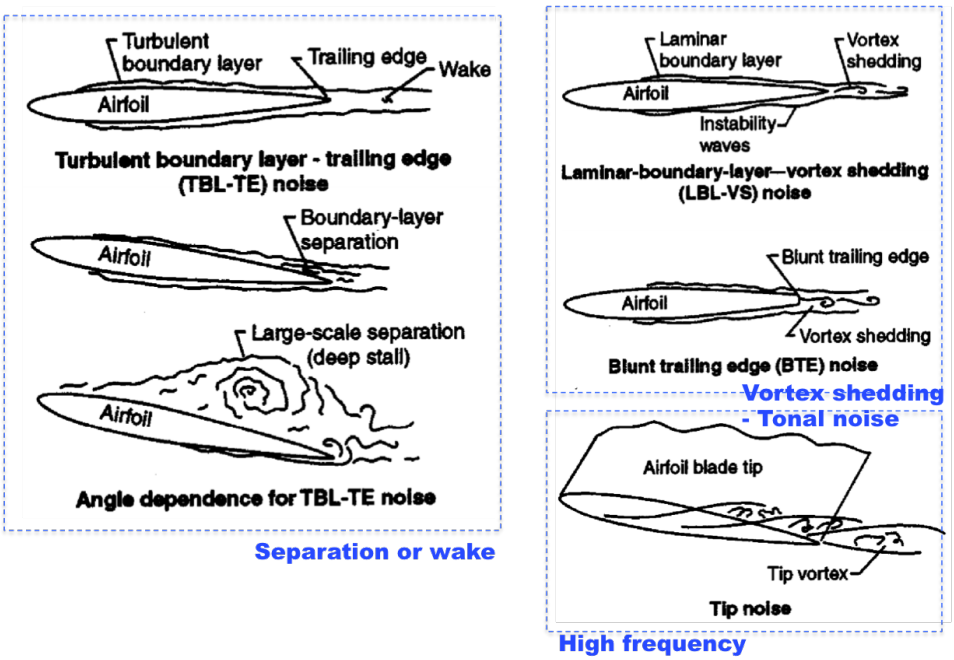

Figure 1.12: Categories of the airfoil self noise, edited images courtesy of Brooks, Pope, and Marcolini, NASA-RP-1218, 1989 [19]

of blade, the TBL-TE or LBL-VS noise is dominant depending on the blade profile and rotating speed. At the inboard of blade, the aero-acoustic noise is the TBL-TE with massive separation or the BTE noise, or both.

1.3.4 Blade Inboard Noise

Thick profile of modern blade inboard is easy to get flow separation. In many cases, the separation is massive, and it causes the TBL-TE with deep stall noise. In this case, high magnitude noise emits in broad frequency band, therefore the noise isn't very much tonal. As we discussed in the previous section, one can design the flatback trailing edge instead of the conventional sharp trailing edge for the aerodynamic benefit. This will help to delay or prevent the massive separation. However, now its blunt trailing edge will cause the strong trailing edge vortex shedding which may affect the noise characteristics as shown in Figure 1.13. If the vortex shedding is vivid and strong, the noise becomes a tonal sound. Now it is a conundrum, since both the massive separation and the strong tonal noise are undesired.

1.4 Drag and Noise Reduction Devices for Flatback Airfoil

There have been many attempts to develop drag and noise reduction devices for the flatback airfoil. Common idea of the devices is a modification of blunt trailing edge (specifically 'add-on's). From the ages of Nash et al. to the recent days, various types of trailing edge modification have been investigated as shown in Figure 1.14 [13, 20, 21]. Briefly, successful add-on type devices reduce 40-50% of

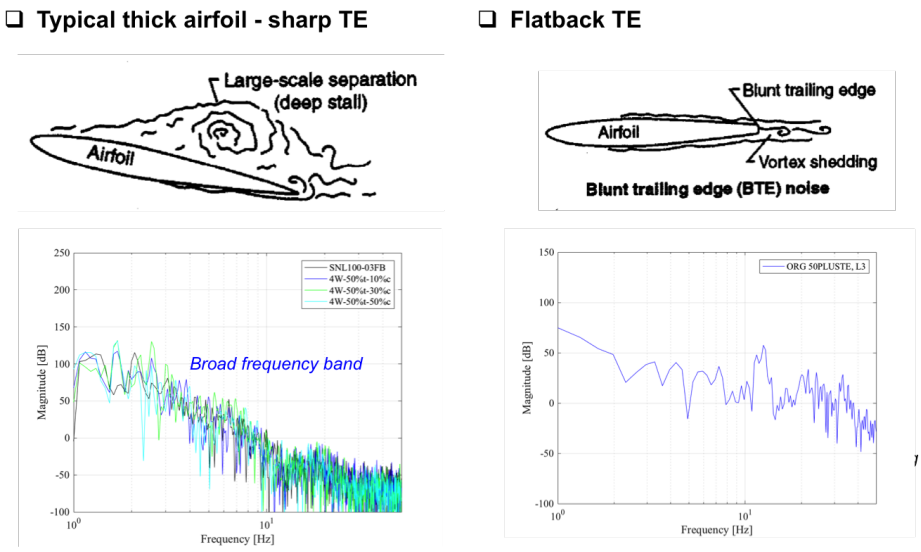

Figure 1.13: Two different blade inboard noise depending on the trailing edge type; airfoil self-noise captured from the Brooks' report [19], signal analysis plots are authors own results

the base drag, and 10-20% of the tonal noise peak [22]. Notable research history of the drag and noise reduction add-ons for the flatback airfoil is presented in Table 1.5, and researches of the add-ons for the sharp trailing edge airfoils (for currently available or prototype wind turbine blades) are presented in Table 1.6. More specific characteristics of these drag reducers are introduced in the next chapter.

These aerodynamic and aero-acoustic benefits are definitely positive points. Some negatives of the add-on drag reducers are; risk of part failure (part fall off, as shown in Figure 1.15), additional manufacturing and management process, additional weight, so on. Structural failure of wind turbine blade isn't frequent event. However, any add-on parts of the blade will increase possibility of the blade failure, which is also undesirable.

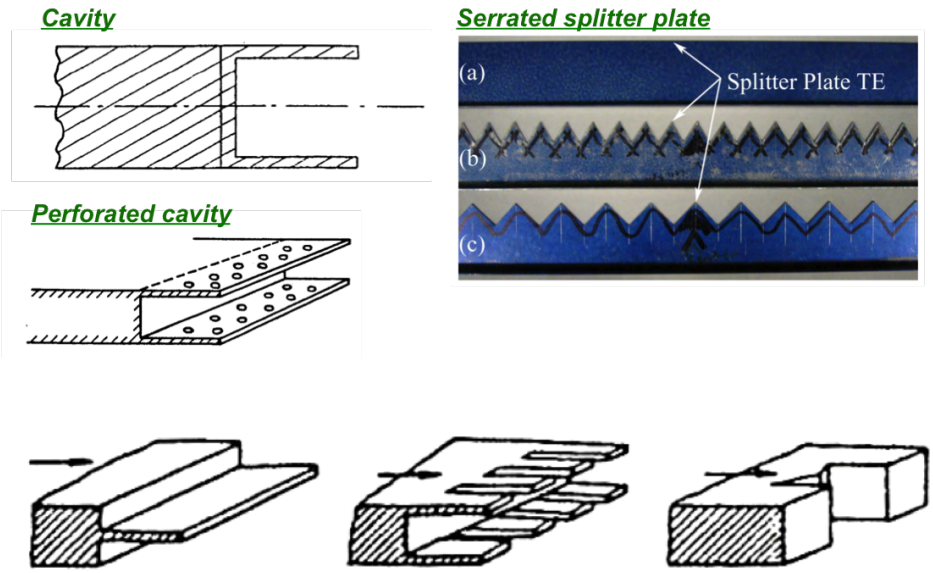

Figure 1.14: Various types of drag and noise reduction add-ons for flat-back airfoil; images courtesy of Nash [13], Tanner [20], van Dam [21]

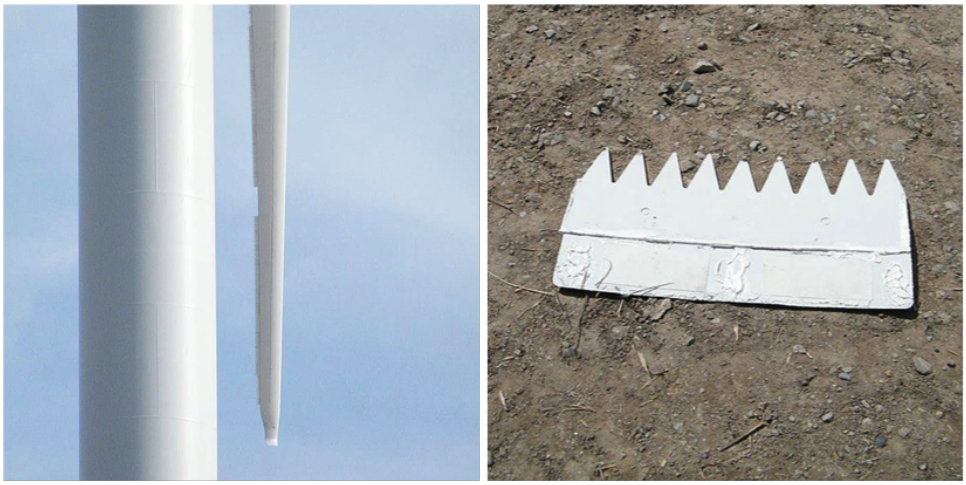

Figure 1.15: An example of an add-on device failure, image courtesy of xxx

Table 1.5: Research history of drag and noise reduction add-ons for the flatback airfoil

Low-noise devices for flatback airfoils	National Physics Lab. Nash et al. (experimental)	Rounded trailing edge Cavity Perforated cavity	First comprehensive study of base drag	1966 1967
	DFVLR, Gottingen Tanner (experimental)	Splitter plate Ventilated cavity M-shaped trailing edge	First serrated trailing edge add-on for flatback trailing edge	1973
	Indian Institute of Tech, Bombay Gai and Sharma (experimental)	Various serrated trailing edge	Tested various serrated trailing edge for flatback trailing edge	1981
	UC-Davis C.P.vanDam, Baker (experimental & CFD)	Splitter plate Serrated splitter plate	FB3500-1750 with splitter, serrated splitter plate add-ons - Drag and noise reduced - but still tonal noise	2008
	Virginia Tech / Sandia Lab. Barone, Berg (experimental)	Splitter plate	Splitter plate on the DU97-W-300 - Drag and noise reduced by 50% - Tonal noise reduced by 12dB (90->79) - but still tonal noise	2009 2010
	National Technical University of Athens Manolesos and Voutsinas (CFD)	Various splitter plates	Modified FB10 airfoil wind tunnel test	2016

Table 1.6: Research history of drag and noise reduction add-ons for current commercial wind turbine blades (sharp trailing edge)

Low-noise devices for sharp trailing edge airfoils	GE Energy Oerlemans et al. (experimental)	Serrated tapes on the blade	Field test on GE 2.3MW prototype turbine	2009
	Siemense Oerlemans and Fuglsang (experimental)	Vortex generators + DinoTails	Field test	2012
	LM Wind power Mathew at al. (experimental)	Serrated tapes on the blade	Serrated tapes on the blade mid-board	2016

1.5 Reseach Motivation and Objectives

1.5.1 Motivation

Thus, the motivations of current study are same as followings.

Motivations,

(a) Although the flatback airfoil delays flow separation, it also increases the aerodynamic drag and aero-acoustic noise. And the main reason is the trailing edge vortex shedding.

(b) The trailing edge vortex shedding can be diminished by another trailing edge modification, such as a cavity, split plate, or serrated trailing edge.

(c) Most of the trailing edge modifications are 'add-on' type devices until nowadays.

(d) Thus, additional task will be required in manufacturing process

(e) And, add-on type devices are not free from the risk of failure, such as a part fall off from the blade.

(f) Because of the risk of the part failure, additional maintenance, such as more careful blade inspections and repairs will be required.

(g) Therefore, development of a non-add-on type drag and noise reduction device (or design of blade) is worthy to be investigated.

1.5.2 Objectives

Regarding the above motivations, the main objectives of current study are same as followings.

The primary objectives are;

(a) To develop a airfoil-self (non-add-on type) drag/noise reduction design for flatback airfoil.

(b) Comprehensive investigations of a new trailing edge modification, 'Span-wise wavy trailing edge' for a new drag/noise reduction design.

The secondary objectives are;

(a) Finding out best performance design/sizing of the span-wise wavy trailing edge by design parametric studies

(b) Revealing the aerodynamics and aero-acoustics of modern large turbine blade inboard flow.

(c) Finding out the aerodynamic/aero-acoustic effect of flatback trailing edge on the modern large turbine blade inboard.

(d) Revealing the aerodynamic/aero-acoustic effect of the span-wise wavy trailing edge modification on the blunt trailing edge blade inboard.

(e) Brief exploration of the structural effect of the span-wise wavy trailing edge modification on the blade inboard.

Chapter 2: Drag and Noise Reduction Add-ons for Flatback Airfoil

2.1 Effect of Drag on Wind Turbine Blade

Effect of the drag on the wind turbine blade performance is either positive or negative depending on the types of wind turbines. There are two types of wind turbines; the drag-driven turbines and the lift-propelled turbines.

2.1.1 Drag-Driven Wind Turbines

The drag-driven wind turbines use the drag differentials to drive the turbine system. The mechanism of the drag-driven turbines is shown in Figure 2.1. As shown in the figure, propulsive forces are generated by the drag of the turbine blade, as like sail propelled ships. For the wind turbine system, the differential between the drag forces makes the turbine rotates. It is easy and simple mechanism, however, known as less efficient compared to the lift-propelled turbine [23]. Because the rotor rotates in the same direction with the winds, the relative flow velocity (between the wind and rotor rotation) acting on the propulsive blade is getting slower as the rotation speed is getting faster. Thus, the turbine rotation speed can not exceed the wind velocity. Typical cup anemometers and savonius turbines are the representative

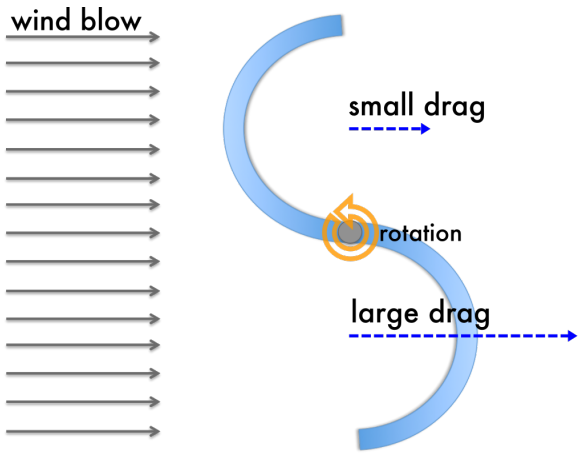

Figure 2.1: Propulsion mechanism of the drag-driven wind turbine

drag-driven turbines as shown in Figure 2.2.

2.1.2 Lift-Propelled Wind Turbines

By contraries, the lift-propelled wind turbines use the lift of turbine blade to rotate their turbine rotors. In Figure 2.3, incoming wind flow is perpendicular to the turbine rotating direction. In this mechanism, the airfoil lift drives the rotor, thus the airfoil drag gives negative effect on the turbine rotation. Most of the modern wind turbines are designed with this propulsion mechanism. Since the drag force acts against the turbine rotation, any drag reduction helps to increase its aerodynamic performance. Traditional farm windmills, the Darrieus wind turbines, and the modern Horizontal Axis Wind Turbines(HAWTs) are the representative lift-propelled wind turbines, and the examples of these turbines are shown in Figure 2.4.

Based on the previous studies, the lift-propel mechanism is more efficient than

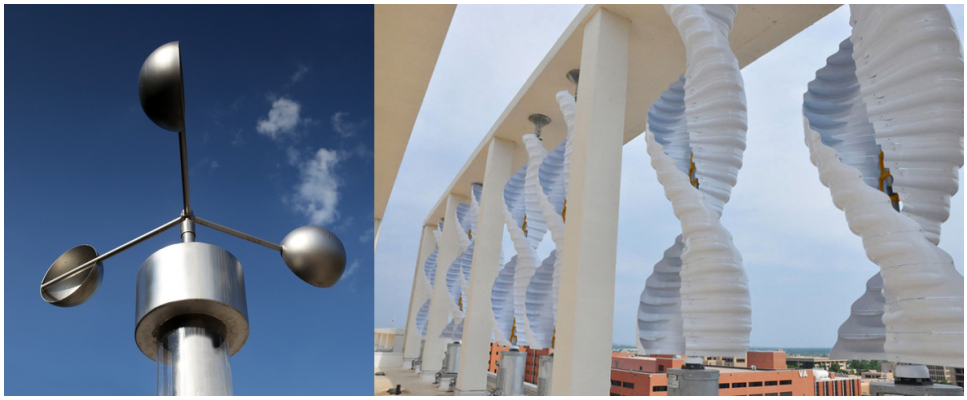

Figure 2.2: Examples of the drag-driven wind turbines; a cup anemometer and a savonius wind turbine

the drag-driven mechanism. This is well noted in Schubel and Crossely's review paper, which published in 2012 [23]. In Table 2.1, Schubel and Crossely's results are presented which comparing the efficiency of the modern and historical rotor designs. Based on the review, the maximum efficiency of the drag-driven turbines does not exceed more than 16%, while the typical efficiency of the lift propelled turbines are in a range between 27% and 50%. This is one of the reasons why the most modern wind turbines have the lift-propelled rotor driven system. And it also shows us why the modern wind turbines prefer the lower drag rotor blade designs.

2.2 Add-on type drag reduction devices

For the reason, the large drag increase of the flatback airfoil may result in the turbine power loss for the HAWTs. To overcome this aerodynamic problems, there have been many different types of drag reduction add-ons that have been tested for the blunt trailing edge. Aerodynamic characteristics and the basic working physics

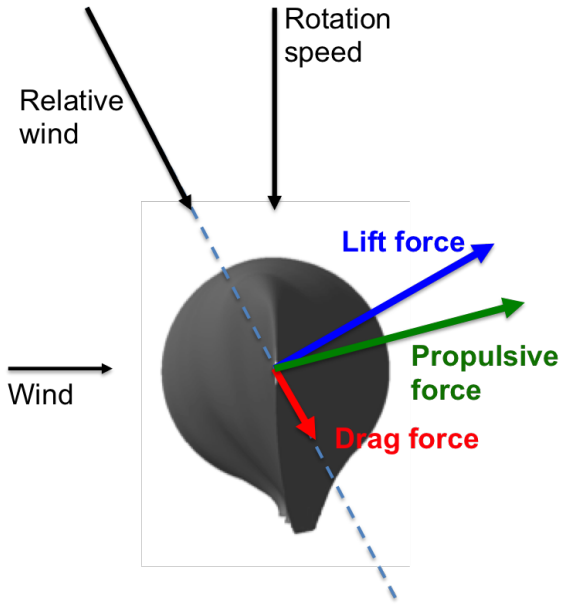

Figure 2.3: Propulsion mechanism of the lift-propelled wind turbine

Figure 2.4: Examples of the lift-driven wind turbines; a farm windmill, a darrieus wind turbine, and a modern horizontal axis wind turbine (HAWT)

Table 2.1: Efficiency of modern and historical rotor designs; referenced from P.J. Schubel and R.J. Crossely's review [23]

Design	Orientation	Propulsion	Maximum Efficiency
Savonius rotor	VAWT	Drag	16%
Cup	VAWT	Drag	8%
Dutch windmill	HAWT	Lift	27%
American farm wind mill	HAWT	Lift	31%
Darrieus rotor	VAWT	Lift	40%
Modern wind turbine	HAWT	Lift	43%(1 blade) 47%(2 blades) 50%(3 blades)

of those drag reduction add-ons are briefly introduced in the current chapter.

2.2.1 Splitter Plate

Probably, splitter plates are the most frequently tested drag reduction add-ons among the other drag reduce devices for the blunt trailing edge airfoils. And here is the working physics. As discussed in Chapter 1, for the blunt trailing edge airfoils, the strong standing vortical flow at the base region is the main reason of the large drag increase. In this situation, adding a splitter plate on the blunt trailing edge displaces the vortical flow away from the trailing edge. By this method, one can reduce the drag of blunt trailing edge effectively, and many encouraging results have been reported until the current.

J.F. Nash is one of the first researchers had tested the splitter plate add-ons. In his study, the size optimized splitter plate decreases the base drag of the blunt trailing edge about the maximum 51% at Mach number 0.4, and about 48% at Mach number 0.8 [13]. Similarly, P.W. Bearman [26] also proved splitter plates

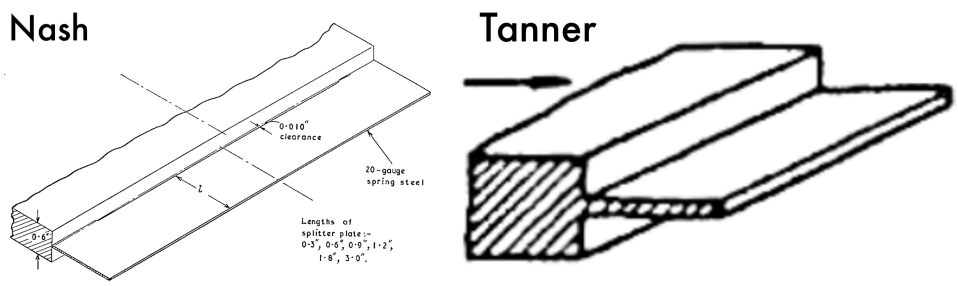

Figure 2.5: Examples of the splitter plate add-ons (source: Nash [13], Tanner [20])

reduce the base drag by the maximum 50%. However, the similar studies performed by Roshko [10] and M. Tanner [20] state their splitter plate reduced the base drag by only the maximum 24-26%.

More recently, J.P. Baker and C.P. van Dam [27] tested a splitter plate added FB3500-1750 airfoil for the wind turbine application. And their results also proved around the maximum 50% of the drag reduction. Similarly, M.F. Barone and D. Berg [22] tested a splitter plate attached DU97-flatback airfoil also for wind turbine applications. They also proved approximately the maximum 50% of the drag reduction by adding the splitter plate.

2.2.2 Base Cavity

Adding a cavity on the blunt trailing edge is another possible solution. Classic working theory explained that the cavity device on airfoil trailing edge traps the eddies inside of the cavity, and the standing (or trapped) eddies cause pressure increase at the trailing edge. Finally it results in reducing the drag. However, Nash had found that trapping the stable eddies are not necessary for the base drag

Figure 2.6: Splitter plate attached blunt trailing edge airfoil, FB3500-1750 (source: C.P. van Dam [27])

reduction, and this is supported by the similar discussions presented in the Hazen's report [28]. In his report, Nash concludes the stability improvement of the trailing edge vortex results in the base drag reduction, whether it traps the standing eddy inside of the cavity or not. More recently introduced working physics is that a cavity displaces the low pressure vortical flow away from the blunt trailing edge. It is same (or at least similar) working physics as the splitter plate [29]. Nash's test [12] had proven that a cavity add-on reduces the drag by the maximum 21% at Mach number 0.4, and the maximum 23% at March number 0.8.

However, the ventilated cavities such as slotted and perforated cavities might be better for the drag reduction. Both the slotted and perforated ventilation bleed the air flow through the vents. However, the slotted cavity operates more likely as

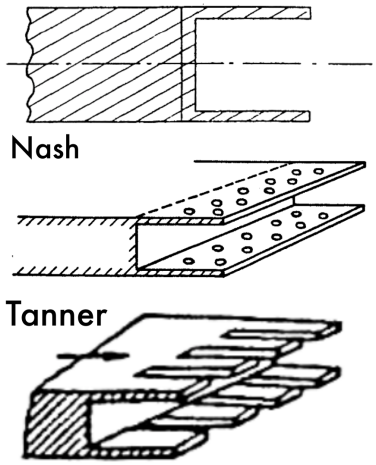

Figure 2.7: Examples of the plain cavity and ventilated cavity add-ons (source: Nash [13], Tanner [20])

vortex generators do. Stream-wise slots of the cavity increase mixing in the shear layers so that increases stability. For the overall drag decrease, slotted cavity works better than the perforated cavity. Based on the later test results of Nash et al in 1965 [13], the base drag reduction by the slotted cavities is approximately the maximum 52% at Mach number 0.4.

2.2.3 Serrated Trailing Edge

There are two types of serrated trailing edge modification for the blunt trailing edge drag reduction. The first type of serrated trailing edge modification is to modify trailing edge itself without any add-ons. M. Tanner is one of the representative researcher who tested serrated trailing edge [20]. He tested rectangular and M-shape serrated trailing edges, and they reduce the drag by the maximum 35% and 64% respectively. The serrated trailing edge operates in the same way as the slotted

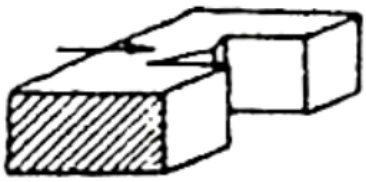

Figure 2.8: An examples of the serrated trailing edge (source: Tanner [20])

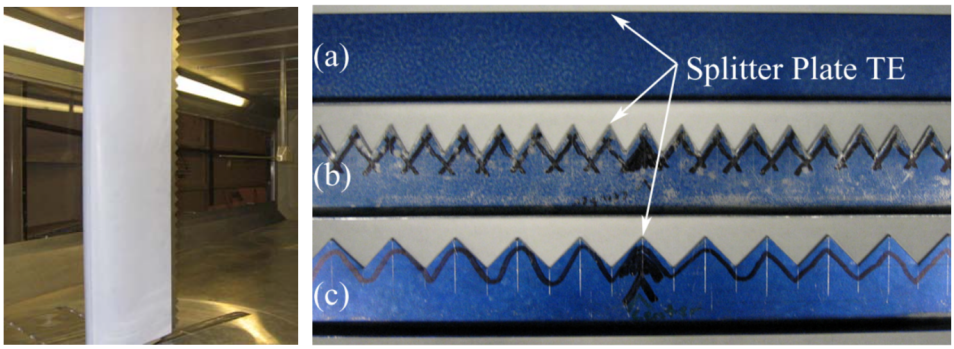

Figure 2.9: Examples of serrated splitter plate add-ons (source: C.P. van Dam [27])

cavity does. There are many different shapes of trailing edge serration have been tested since 1960s. Brief aerodynamic and acoustic performance of various trailing edge serrations are well described in P.J. Deshpande and S.D. Sharma's paper [30].

The second type of serrated trailing edge modification is serrated splitter plate add-ons. These are more frequently tested in the recent for the wind turbine application. Baker et al. [27] also tested the serrated splitter plate add-on and the non-serrated splitter plate as well for the FB3500-1750 flatback airfoil. However, in their results, the drag reduction was not so many different with the non-serrated splitter plate.

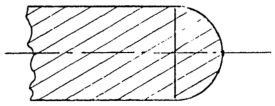

Figure 2.10: An example of the rounded trailing edge (source: Nash [13])

2.2.4 Rounded Trailing Edge

Sargent's study [31] is one of the earliest researches focusing on the rounded trailing edge. In his study, he showed a significant drag reduction using the rounded trailing edge for a small degree of trailing edge bluntness(3% of the chord) in subsonic flow condition. Inspired by Sargent [31]'s study, Nash had tested the rounded trailing edge, too. However, he concludes that the effectiveness of the rounded trailing edge as a drag reduction method is dubious [12]. In Nash's test, the rounded trailing edge reduced the drag only over a small range of Mach number around 0.4. But for higher Mach number, it didn't reduced the base drag much enough. According to his conclusions, the rounded trailing edge operates in the same way as a short splitter plate does at the low Mach number region, but for the higher Mach number region, the flow follows curvature of the round trailing edge, and is accelerated rather than deceleration by the blunt trailing edge. This flow acceleration at the airfoil base makes the lower pressure region at behind the trailing edge, and it increases the drag rather than the decrease. Comparing with the Sargent's study, Nash recommends that using the rounded trailing edge isn't a promising idea (or controversial) for a degree of trailing edge bluntness, 4% or greater.

Chapter 3: Span-wise Wavy Trailing Edge

3.1 Motivation

There must be no doubt that the flatback trailing edge is a great design option for the structural enhancement of the wind turbine blade inboard. However, as we discussed in the previous chapters, the large drag of the blunt trailing edge may affect against the overall power performance of the modern wind turbines. Recalling the previous chapter, only the add-on type drag mitigation devices such as the splitter plate, cavity, and serrated plate have been considered for the drag less flatback blade design, until today. According to the previous airfoil tests cited in Chapter 2, the drag reduction add-ons reduce the overall drag of flatback airfoils up to 50-60%, however the lift also reduces in the meantime. This cancels out the aerodynamic benefit of the drag reduction, thus should be avoided. Other considerable disadvantages of the add-ons are; a) to require additional manufacturing process, b) and also additional maintenance process c) and the add-on devices means additional blade mass, d) and risk of failure, as we discussed in chapter 1.

Regarding the disadvantages, one can imagine a proper geometric transformation of the blunt trailing edge itself (instead of attaching another part on the blade), which is a much simpler and instinctive solution to solve the drag problem. By this

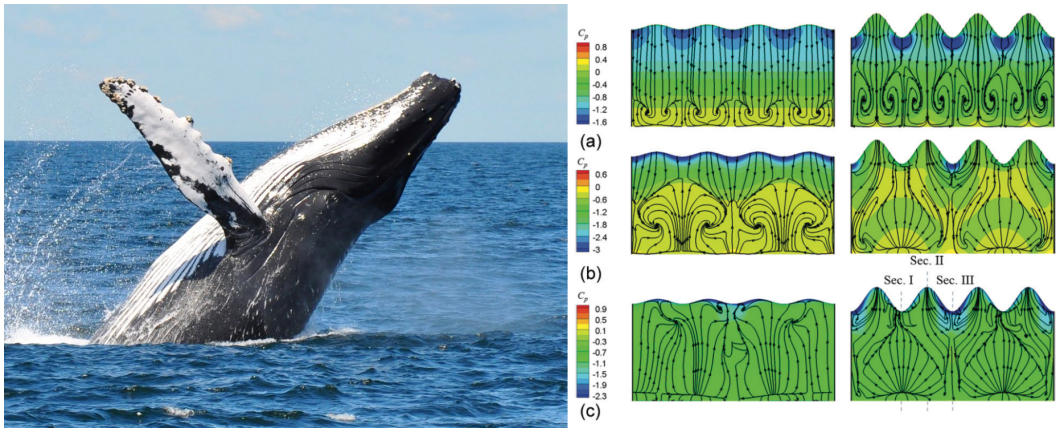

Figure 3.1: Tubercles of humpback whales (photographed by Lisa Winchester, National Geographic) and their bio-inspired airfoil designs (courtesy of C.Cai [33])

way, no additional manufacturing or maintenance processes will be required. And obviously there will be no risk of failure such as the parts fall-off. In the other hand, it may improve the aerodynamic performance of the airfoil (or wind turbine blade). Based on the previous drag reduction add-ons for blunt trailing edges, to reduce the drag in the blunt trailing edge airfoils, the strong vortical flow at the trailing edge must be pushed toward the downstream flow. And one can expect much larger drag reduction when the flow at the trailing edge base is well mixed (or swirled) by the add-on devices such as the vortex generator, ventilation slots, and trailing edge serrations.

However, designing a drag reduced blunt trailing edge without a drag reduction add-on requires a creative imagination. Fortunately, a solution can be found in the nature. Some pioneering researchers found an inspiring airfoil design in humpback whales. These are the tubercles on their fins (in Figure 3.1), and they work exactly

same as the vortex generators. Same as the vortex generators, the tubercles prevent massive flow separation on their fins and give the whales more maneuverability [32]. The idea of the span-wise wavy trailing edge in the current study is inspired by those tubercles. The concept has inspired some previous aircraft wing design projects already. Most of the previous studies considered to put the tubercles at the airfoil leading edge to delay the flow separation, same as the vortex generators work. Performance of the leading edge tubercles are proven in the previous literatures [32] [33].

In the wind turbine aerodynamics, commonly the rotor inboard area isn't very effective to generate power. This is because of the aerodynamic loss caused by the flow separation at the root/inboard region. The current study focuses on the aerodynamic and acoustic performance improvement at the blade inboard by reducing the drag and tonal noise. The inboard power loss can be overcome by the blunt trailing edge design. However, the large drag increase is still a significant problem, since it reduces the overall turbine power generation. To figure out the solution of this conundrum, we applied the tubercle like wavy pattern to our blunt trailing edge airfoil. More specifically, we put a span-wise wavy-like variation in the trailing edge thickness, and expected that the wavy trailing edge will help to guide more stream-wise flow into the airfoil base region. More stream-wise inflow will give more mixing (or swirl) to the standing flow residing at the airfoil base. By this process, we expect that the new trailing edge modification; 1) weakens the vorticity at the trailing edge region, 2) moves the standing flow away from the trailing edge, and finally results in the large amount of drag reduction while only the tiny lift loss.

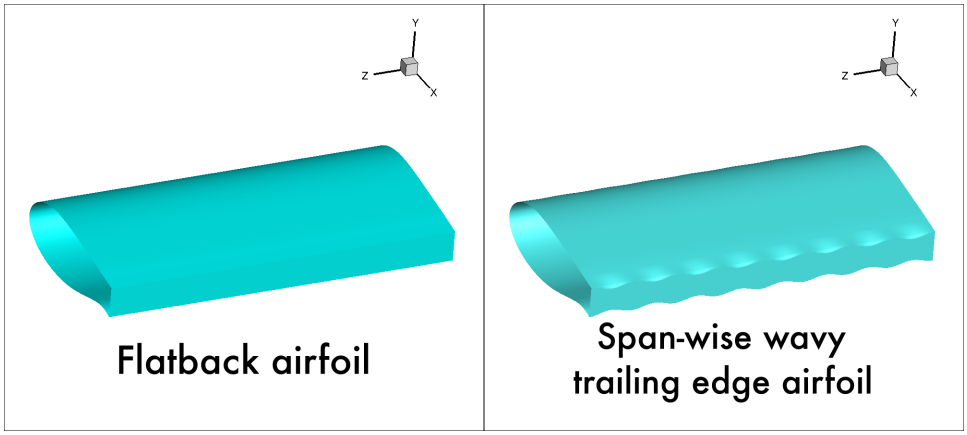

Figure 3.2: Span-wise wavy trailing edge modification for flatback airfoil proposed in the current study

3.2 Span-wise Wavy Trailing Edge Design

3.2.1 Formula of Span-wise Wavy Trailing Edge Design

An example of the proposed span-wise wavy trailing edge design is presented in Figure 3.2. The geometry of the span-wise wavy trailing edge is generated by varying the trailing edge thickness along the span-wise direction with sinusoidal wave distributions with various wave factors. A modified cosine formula, presented in Equation 3.1 and 3.2, is used to determine the local trailing edge thickness in the span-wise direction. In the formula, ω is the wave number, and z, l represent a span-wise location and a length of the wave, while y_{max}, y_{min} represent the maximum and the minimum heights from the airfoil chord line, respectively. The trailing edge thickness variations of the various wavy trailing edge designs are presented in Figure 3.3.

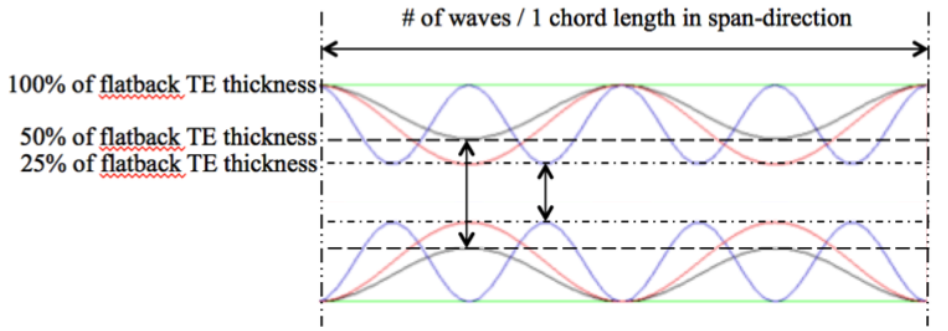

Figure 3.3: Trailing edge thickness variation generated by modified cosine formula

There might be two opposite trailing edge modifications with the wavy design; 1) embossed wavy trailing edge 2) engraved wavy trailing edge. However, if the trailing edge is already thick enough to delay the flow separation, embossed waves might be inefficient to reduce the base drag. For the reason, engraved type wavy trailing edge (as shown in Figure 3.2 through 3.4) is primarily considered in the current study.

In the figures, the span-wise wavy trailing edge airfoils have been created with a baseline airfoil, the FB3500-1750. The airfoil has dimensions of the trailing edge thickness, 17.5% of c, and the airfoil thickness, 35% of c. The coordinates of wave trailing edge geometries are generated by a simple Matlab code.

$$\Delta y = y_{max} - y_{min}, \tag{3.1}$$

$$t_{te}(z) = \frac{\Delta y}{2}[cos(2\pi\omega z/l) + 1] + y_{min} \tag{3.2}$$

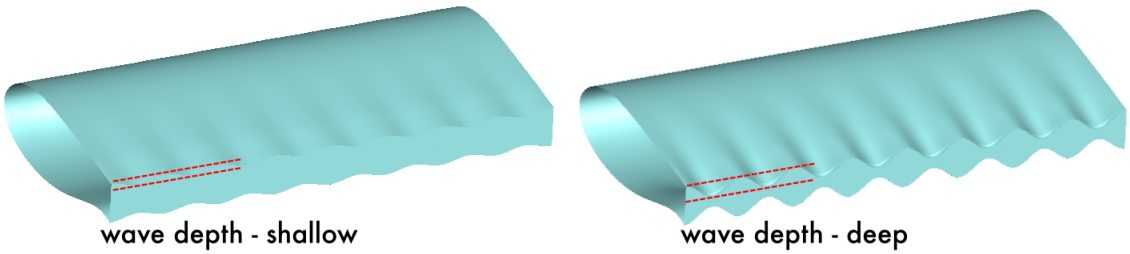

Figure 3.4: Different wavy trailing edge modification by varying its wave depth

3.2.2 Key Design Parameters for Span-wise Wave Trailing Edges

To design a span-wise wavy trailing edge, three parameters; (a) wave depth, (b) wave length, and (c) wave portion are mainly considered. Each of the key design parameters directly affects to the aerodynamic characteristics of the modified airfoil. To understand the role of the design parameters, a comprehensive parametric study is required.

(a) Wave depth: in the current study, 'wave depth' is defined as a distance between the crest and trough of a wave. The wavy trailing edges differed by the wave depth variations are presented in Figure 3.4. It is assumed that the deeper wave depth reduces the base drag more than the shallow wave depth, but also reduces the lift force more than the shallow wave depth.

(b) Wave length: in the current study, 'wave length' is defined as a distance between the wave crests. The wavy trailing edges differed by the wave length variations are presented in Figure 3.5. Changes of the wave length differs the curvature of wave trough, which may influence to the velocity vectors at the

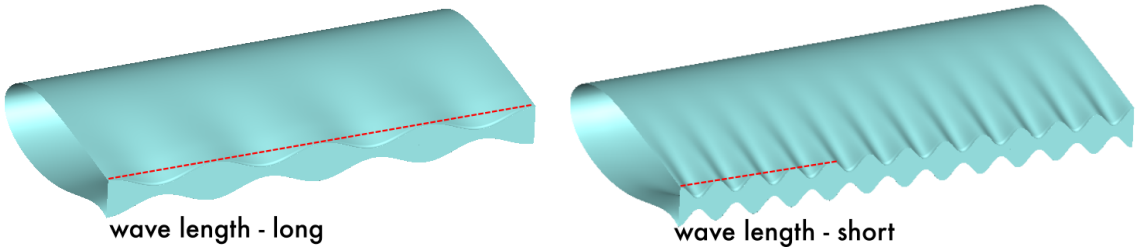

Figure 3.5: Different wavy trailing edge modification by varying its wave length

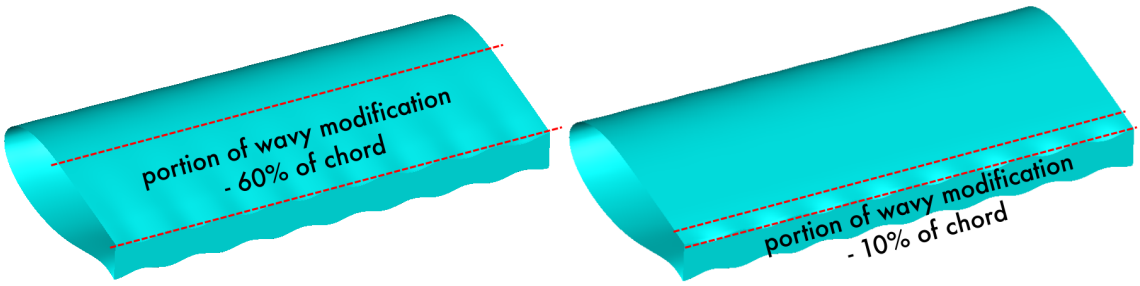

Figure 3.6: Different wavy trailing edge modification by varying the portion of modification

trailing edge.

(c) Wave portion: in the current study, 'wave portion' is defined as a distance from the trailing edge to the unmodified region in a chord-wise direction. The wavy trailing edges differed by the wave portion variations are presented in Figure 3.6. As the wave depth and length are same in two different span-wise wavy modifications, varying the portion of modification differs a chord-wise curvature of the wave trough. It may affect to the adverse pressure gradient at the modified region.

3.2.3 Naming Notation of Span-wise Wavy Trailing Edges

Obviously, there might be numerous variations of the span-wise wavy trailing edge design depending on the combinations of three key wave parameters, as shown in Figure 3.7. Each trailing edge modifications are named with the following rules of naming notation.

In Figure 3.8, the rules of naming notation for the span-wise wavy trailing edge airfoil is presented with a relevant example. The first part of the notation represents the wave length. The wave length is presented with the number of waves per a chord length in the span. In the example presented in Figure 3.8, the modified trailing edge has 4 waves per a chord length along the airfoil span. Thus, the airfoil is named with '4W'.

The second part of the name represents the wave depth. The wave depth is presented with the ratio of the maximum and minimum trailing edge thickness in the relevant airfoil. In the figure, the minimum trailing edge thickness of the airfoil is 0.25, while the maximum trailing edge thickness is 1.0. Thus, the ratio of the maximum and minimum trailing edge thickness is 25 in percentile, thus the name is now tagged with '25%t'.

The last part of the name represents the portion of the wavy trailing edge modified region in the airfoil. In the current study, only three cases of the different portions of the wavy trailing edges are investigated, and they are; the maximum portion of the wavy trailing edge modification, and two less portion of wavy trailing edge modifications, such as 'only 10% of a chord', and 'half way cut'. Only the less

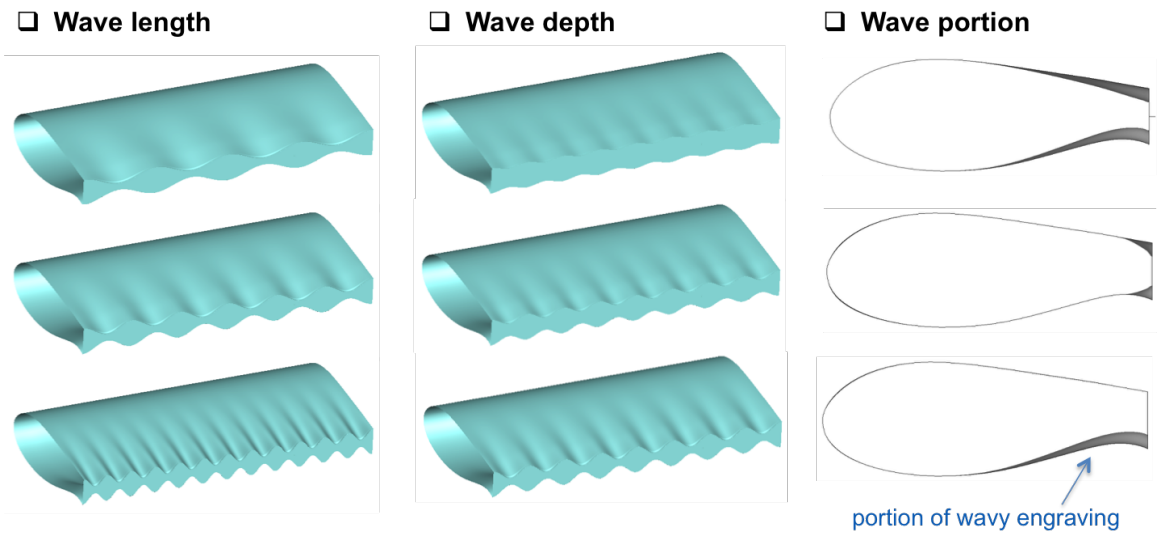

Figure 3.7: Several variations of the span-wise wavy trailing edge design sorted by the key wave parameters

portion wavy trailing edge airfoils are tagged with the notations, such as '10%c' and 'half', respectively.

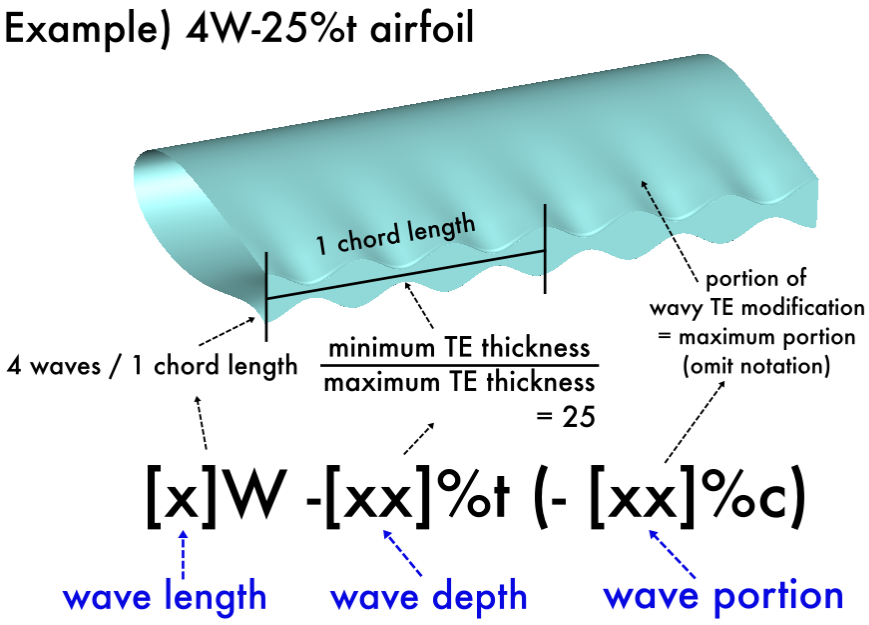

Figure 3.8: An example of naming notation of a span-wise wavy trailing edge airfoil

Chapter 4: Numerical Methods

The current study is performed using computational approaches. The mainly focused flow regimes are; low Mach number (Mach number: 0.1 - 0.4), high Reynolds number (Re number: 500,000 - 5,000,000), and highly unsteady. In addition, the research focuses on simulating flow separation and vortical flow near the trailing edge. For the reasons, governing equations for the flow simulations are solved with the special modeling techniques (explained latter in the chapter).

In the airfoil simulations, the most efficient way to model both the boundary layer and the turbulent eddies might be a hybrid RANS-LES method. Since the current study focuses on both the boundary layer and the large turbulent eddies, a hybrid RANS-LES solver is required to achieve high fidelity and high computational efficiency. For this reason, DDES (Delayed Detached Eddy Simulation) method is selected in the current study. Spalart-Allmaras one equation turbulent model is used. For the successfully resolving the flow separation and turbulent eddies, a laminar-turbulent transition model is used with Adverse Pressure Gradient (APG) correction.

4.1 Governing Equations

4.1.1 The Navier-Stokes Equations

The governing equations used in the current works are the three-dimensional, unsteady, compressible Navier-Sotkes equations. In Cartesian coordinates, those can be written as presented in Equation 4.1. In the system of equations, $\mathbf{Q}$ is the vector of conserved variables, and $\mathbf{F}, \mathbf{G}, \mathbf{H}$ are the vectors of flux variables. The subscriptions, i and v represent the inviscid and viscous terms respectably, and $\mathbf{S}$ is the source term of the body-force.

$$\frac{\partial \mathbf{Q}}{\partial t} + \frac{\partial \mathbf{F}_i}{\partial x} + \frac{\partial \mathbf{G}_i}{\partial y} + \frac{\partial \mathbf{H}_i}{\partial z} = \frac{\partial \mathbf{F}_v}{\partial x} + \frac{\partial \mathbf{G}_v}{\partial y} + \frac{\partial \mathbf{H}_v}{\partial z} + \mathbf{S} \tag{4.1}$$

When one sets with primitive variables such as the density of fluid as ρ, the Cartesian velocity components of the fluid as u, v, w, and the total energy per unit volume as E, the vector of conservative variables can be written as shown in Equation 4.2.

$$\mathbf{Q} = \begin{vmatrix} \rho \\ \rho u \\ \rho v \\ \rho w \\ E \end{vmatrix} \tag{4.2}$$

In the equation, the total energy per unit volume, E is given as shown in Equation 4.3.

$$E = \rho\left[e + \frac{1}{2}(u^2 + v^2 + w^2)\right] \tag{4.3}$$

The inviscid flux vectors, F_i, G_i, H_i can be written as shown in Equation 4.4 - 4.6. In the flux vector, p is the pressure which can be determined by the equation of state for a perfect gas law as shown in Equation 4.7, where γ is the ratio of the specific heat at constant pressure (C_p) to the specific heat at a constant volume (C_v).

$$\mathbf{F}_i = \begin{vmatrix} \rho u \\ \rho u^2 + p \\ \rho uv \\ \rho uw \\ u(E+p) \end{vmatrix} \tag{4.4}$$

$$\mathbf{G}_i = \begin{vmatrix} \rho v \\ \rho vu \\ \rho v^2 + p \\ \rho vw \\ v(E+p) \end{vmatrix} \tag{4.5}$$

$$\mathbf{H}_i = \begin{vmatrix} \rho w \\ \rho w u \\ \rho w v \\ \rho w^2 + p \\ w(E+p) \end{vmatrix} \tag{4.6}$$

$$p = (\gamma - 1)\left[E - \frac{1}{2}\rho(u^2 + v^2 + w^2)\right] \tag{4.7}$$

The viscous flux vectors, F_v, G_v, H_v can be written as shown in Equation 4.8 - 4.10.

$$\mathbf{F}_v = \begin{vmatrix} 0 \\ \tau_{xx} \\ \tau_{yx} \\ \tau_{zx} \\ u\tau_{xx} + v\tau_{xy} + w\tau_{xz} - q_x \end{vmatrix} \tag{4.8}$$

$$\mathbf{G}_v = \begin{vmatrix} 0 \\ \tau_{xy} \\ \tau_{yy} \\ \tau_{zy} \\ u\tau_{yx} + v\tau_{yy} + w\tau_{yz} - q_y \end{vmatrix} \tag{4.9}$$

$$\mathbf{H}_v = \begin{vmatrix} 0 \\ \tau_{xz} \\ \tau_{yz} \\ \tau_{zz} \\ u\tau_{zx} + v\tau_{zy} + w\tau_{zz} - q_z \end{vmatrix} \tag{4.10}$$

In the vector components, $q_x, q_y, and q_z$ represent the heat conduction, and defined as shown in Equation 4.11 as a function of temperature according to the Fourier's law.

$$q_i = -k\frac{\partial \mathbf{T}}{\partial x_i} \tag{4.11}$$

In the equation, k is the thermal conductivity and T is the temperature. The temperature can be written as shown in Equation 4.12, by the perfect gas law where R is the gas constant.

$$T = \frac{p}{\rho R} \tag{4.12}$$

In the viscous flux vector, τ is the mean shear stress which can be defined by Stokes' theorem as shown in Equation 4.13.

$$\tau_{ij} = \mu \left[\left(\frac{\partial u_{ij}}{\partial x_{ij}} + \frac{\partial u_{ji}}{\partial x_{ij}} \right) - \frac{2}{3}\frac{\partial u_k}{\partial x_k}\delta_{ij} \right] \tag{4.13}$$

In the equation, μ is the laminar viscosity, which can be evaluated by the Sutherland's law as shown in Equation 4.14.

$$\mu = C_1 \frac{T^{\frac{3}{2}}}{T + C_2} \tag{4.14}$$

At the standard temperature and pressure (STP), C_1 is 1.4 x 10^{-6} $kg/(ms\sqrt{K})$ and C_2 is 110.4 K.

4.1.2 Non-dimensionalization of the Navier-Stokes Equations

To apply above governing equations to a computational solver, non-dimensionalization of the governing equations is required. Non-dimensionalization 1) gives dynamic and energetic similarity for geometrically similar flow conditions 2) reduces number of free parameters and 3) minimize potential numerical inaccuracies. In the current, study, an airfoil chord length, L, a speed of sound at free stream, a_∞ and density at free-stream, ρ_∞ have been used as reference parameters. In Equation 4.15, denoted variables with '*' are the non-dimensional variables used in the current solver.

$$\begin{aligned} t^* = \frac{ta_\infty}{L}, (x^*, y^*, z^*) = \frac{(x, y, z)}{L}, (u^*, v^*, w^*) = \frac{(u, v, w)}{a_\infty}, \\ \rho^* = \frac{\rho}{\rho_\infty}, T^* = \frac{T}{T_\infty}, p^* = \frac{p}{\rho(a_\infty)^2}, E^* = \frac{E}{\rho(a_\infty)^2}, \mu^* = \frac{\mu}{\mu_\infty} \end{aligned} \tag{4.15}$$

The non-dimensional flow parameters are defined as shown in Equation 4.16 - 4.18.

$$ReynoldsNumber : Re_\infty = \frac{\rho_\infty V_\infty L}{\mu_\infty} \tag{4.16}$$

$$MachNumber : M_\infty = \frac{V_\infty}{a_\infty} \tag{4.17}$$

$$PrandtlNumber : Pr_\infty = \frac{\mu Cp}{k} \tag{4.18}$$

For definition of the Mach number and Reynolds number, V_∞ is the magnitude of free-stream velocity, and defined as shown in Equation 4.19. In the current study, the known value of the Prandtl number of air at STP, $Pr_\infty = 0.72$ is used.

$$V_\infty = \sqrt{u_\infty^2 + v_\infty^2 + w_\infty^2} \tag{4.19}$$

The forms of the Navier-Stokes equation presented in Equation 4.1, and both inviscid and viscous flux terms are not changed with the normalization. However, non-dimensional stress tensor and heat conduction terms are now transformed as functions of Reynolds number and Prandtl number as shown in Equation 4.20 - 21.

$$\tau_{ij} = \mu \left(\frac{M_\infty}{Re_\infty} \right) \left[\left(\frac{\partial u_i}{\partial x_j} + \frac{\partial u_i}{\partial x_j} \right) - \frac{2}{3} \frac{\partial u_k}{\partial x_k} \delta_{ij} \right] \tag{4.20}$$

$$q_i = -\frac{\mu M_\infty}{Re_\infty Pr_\infty(\gamma - 1)} \frac{\partial \mathbf{T}}{\partial x_i} \tag{4.21}$$

4.2 Turbulent Modeling

4.2.1 DNS/LES/DES/RANS

For the turbulent flow regime, the solution of the Navier-Stokes equations require additional numerical treatments to be closed. In the current, the most frequently using numerical treatments must be; DNS, LES, DES, RANS. The N-S equations can be solved by directly. A Direct Numerical Simulation (DNS) solves the N-S equation directly without any additional turbulent model. However, DNS requires large number of grid points to get an accurate solution. Furthermore, sufficient number of grid points for the accurate solution increase super-linearly with the Reynold number. That means DNS requires very large numbers of grid point to get reliable solutions for the high Reynolds number flow. It causes a limitation for use of DNS, when it apply to the various Reynolds number spectrum.

Large Eddy Simulation (LES) can be applied with more flexibility. Large Eddy Simulation approach only resolves the large length scale eddies and filters out the smaller scale motions. The filtered eddies are modeled using a sub-grid scale model. Because of the filtering process, requirement in the number of grid points can be more flexible to apply to the higher Reynolds number flow. For this reason, LES is more frequently used for the higher Reynolds number flow simulation. However,

since LES is inherently three-dimensional and unsteady, it still requires the large number of grid points.

In this case, use of Reynolds Averaged Navier-Stokes (RANS) equations is a good alternative of LES. As the name of the equations implies, RANS uses a time-averaging concept. In RANS equations, the variables of the original N-S equations are decomposed by two parts; a time-averaged and fluctuation. Use of the RANS equations can save the potential computational expense of the LES or DNS for the high Reynolds number flows. However, it shows less fidelity in some flow cases, such as a flow with high curvature stream lines and abrupt or rapid local variations of flow.

In the current study, to achieve accurate prediction of the complex flow characteristics (such as flow separation, trailing edge vortex shedding and flow mixing) of turbine blade inboard, a high fidelity computational method such as the LES is required. However, sizes of wind turbine simulations are inherently very large, thus numerical approach of full LES is not very efficient.

A hybrid RANS-DES method such as Detached Eddy Simulation (DES) is a good alternative for the LES or RANS methods. DES is proposed and developed by P.R. Spalart et al [34]. DES resolves a flow around solid body surfaces with 1) RANS mode for the thin boundary layers and 2) LES mode for the massive separation flow. Since required number of grid points for RANS is much less than LES, this mode switching saves the computational cost of LES very much.

4.2.2 Delayed Detached Eddy Simulation

DES is initially developed based on a one-equation turbulent model, Spalart-Allmaras (SA) [36]. In the DES, switching mode between RANS - LES begins with a modification of the length scale in the SA turbulent model, d (details of the SA model will be discussed in the next subsection). The original length scale, d is replaced with a new length scale, $\tilde{d}$ as shown in Equation 4.22.

$$\tilde{d} \equiv min(d, C_{DES}\Delta) \tag{4.22}$$

In Equation 4.22, d is the wall distance, C_{DES} is an adjustable constant in order of 1, and Δ is chosen measure of grid spacing, defined as the largest spacing such as $\Delta \equiv max(\Delta x, \Delta y, \Delta z)$ where the $\Delta x, \Delta y, \Delta z$ are grid spaces in each coordinates.

With the RANS-LES combination, DES compromises very well between computational accuracy and cost for resolving near body flow simulations, especially in thin boundary layer - massive separation flow. However, the original form of DES can exhibit an incorrect behavior in thick boundary - shallow separation flow when using with undesired grid spacing [35]. This is called 'Modeled-Stress Depletion (MSD)'.

In Figure 4.1, three different types of grid space in the boundary layer. On the top figure of Figure 4.1, grid spacing in parallel direction to the wall (Δx) is larger than the boundary layer thickness, δ. In this case, RANS mode precisely predicts thin boundary layer. In an opposite case (in Figure 4.1 bottom right), if the wall-

parallel grid spacing is much smaller than the boundary layer thickness ($\Delta x << \delta$), DES resolves with LES mode over the bulk of the boundary layer. If the grid is fine enough to support resolved velocity fluctuations in the boundary layer, DES will produce a good solution. According to Spalart, the plausible value of the grid spacing is $\Delta \approx \delta/20$ ($\Delta \approx \delta/10$ for acceptable results). MSD can be happened in between this two cases. In Figure 4.1, grid spacing in the bottom left of the figure is less than the boundary layer thickness, but not fine enough to support the resolution of LES. With this grid spacing, the DES length scale will be chosen as $\tilde{d} = C_{DES}\Delta$ and activate LES mode, since Δx is still less than δ. This may lead to a reduction in the eddy viscosity below the RANS level, and it may cause undesired Grid Induced Separation (GIS). In this case, DES will predict premature separation flow which is physically incorrect rather than shallow separation which should be expected [35].

Delayed Detached Eddy Simulation is a modified version of DES which has been developed by P.R. Spalart et al [35] to prevent potential MSD problem. In this version, the original form of DES length scale is modified as shown in Equation 4.23 - 4.25, where ν_t is the kinematic eddy viscosity, ν is the molecular viscosity, $U_{i,j}$ is the velocity gradient, and κ is the Karman constant.

$$\tilde{d} \equiv d - f_d max(0, d - C_{DES}\Delta) \tag{4.23}$$

$$f_d \equiv 1 - tanh([8r_d]^3) \tag{4.24}$$

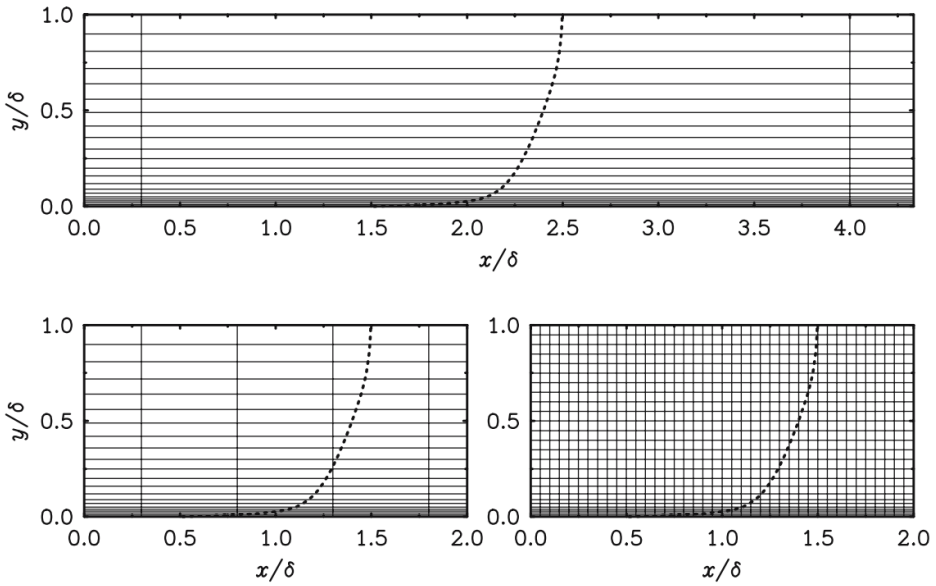

Figure 4.1: Three different cases of grid spacing in a boundary layer; (Top) natural DES, (Bottom left) ambiguous spacing, (Bottom right) LES. Dotted lines are velocity profiles. δ is boundary layer thickness. Courtesy of P.R.Spalart [35]

$$r_d \equiv \frac{\nu_t + \nu}{\sqrt{U_{i,j}U_{i,j}}\kappa^2 d^2} \tag{4.25}$$

The new length scale formula prevents the DES limiter activating LES mode inside the boundary layer while it activates LES in the regions of separation outside of the boundary layer.

4.2.3 Spalart-Allmaras One Equation Turbulent Model

A one-equation turbulent model, Spalart-Allmaras is used in the current study. RANS begins with the Reynold decomposition which variables are decomposed with a mean and fluctuating parts as shown in Equation 4.26. When ϕ is a flow variable, its mean variable is $\bar{\phi}$ and fluctuation variable is $\phi^{'}$, where the mean variable is defined as shown in Equation 4.27. In the definition of the mean variable, t_0 is current time step, and Δt is size of time step.

$$\phi = \bar{\phi} + \phi^{'} \tag{4.26}$$

$$\bar{\phi} = \frac{1}{\Delta t}\int_{t_0}^{t_0+\Delta t} \phi(t)dt \tag{4.27}$$

$$u = \bar{u} + u^{'}, v = \bar{v} + v^{'}, w = \bar{w} + w^{'}, \rho = \bar{\rho} + \rho^{'}, p = \bar{p} + p^{'}, T = \bar{T} + T^{'} \tag{4.28}$$

After replacing the dependent variables of the Navier-Stokes equations (Eq.4.1) with the decomposed form shown in Equation 4.28, and time-averaging, RANS

equations can be derived. The system of final RANS equations is identical to the original N-S equations, with an addition of the turbulent fluctuation term in the momentum and energy equations. This term is called the Reynolds-stress, and adding to the viscous stress term shown in Eq. 4.20, it can be written as shown in Equation 4.29.

$$\tau_{ij}^{R} = -\rho\overline{u_i' u_j'} \tag{4.29}$$

In the momentum equations, now six additional unknowns are required to solve, because of the Reynold-stress terms. To close the RANS equations, the Reynolds-stress terms can be approximated using a turbulent model.

The Spalart-Allmaras model relates the Reynolds-stress and mean strain as follows [36],

$$\overline{u_i' u_j'} = -2\mu_t S_{ij} \tag{4.30}$$

where the eddy viscosity in the isotropic equation above is related to the turbulent variable $\tilde{\nu}$ as follows,

$$\mu_t = \nu_t = \rho\tilde{\nu} f_{\nu 1} \tag{4.31}$$

where $f_{\nu 1}$ is a function of the turbulent variable, $\tilde{\nu}$ and molecular viscosity, ν

as follows,

$$f_{\nu 1} = \frac{\chi^3}{\chi^3 + C_{\nu 1}^3} \tag{4.32}$$

where $\chi = \frac{\tilde{\nu}}{\nu}$, and $C_{\nu 1}^3 = 7.1$. The turbulent variable, $\tilde{\nu}$ can be obtained by solving the PDE shown in below,

$$\frac{\partial \tilde{\nu}}{\partial t} + \mu_j \frac{\partial \tilde{\nu}}{\partial x_j} = \frac{1}{\sigma}\left[\frac{\partial}{\partial x_j}\left((\nu + \tilde{\nu})\frac{\partial \tilde{\nu}}{\partial x_j}\right) + C_{b2}\frac{\partial \tilde{\nu}}{\partial x_j}\frac{\partial \tilde{\nu}}{\partial x_j}\right] + C_{b1}\tilde{S}\tilde{\nu} - C_{w1}f_w\left(\frac{\tilde{\nu}}{d}\right)^2 \tag{4.33}$$

where d is the distance to the nearest wall. In the PDE, $\tilde{S}$ and f_w are as follows,

$$\tilde{S} = max\left[\Omega + \frac{\tilde{\nu}}{\kappa^2 d^2} f_{\nu 2}, 0.3\Omega\right] \tag{4.34}$$

$$f_w = g\left[\frac{1 + C_{w3}^6}{g^6 + C_{w3}^6}\right]^{1/6} \tag{4.35}$$

where Ω is vorticity magnitude, and $f_{\nu 2}$ and g are as follows,

$$f_{\nu 2} = 1 - \frac{\chi}{1 + \chi f_{\nu 1}} \tag{4.36}$$

$$g = r + C_{w2}(r^6 - r) \tag{4.37}$$

$$r = min\left[\frac{\tilde{\nu}}{\tilde{S}\kappa^2 d^2}, 10\right] \tag{4.38}$$

The constants in the above equations are given as follows,

$$C_{b1} = 0.1355, C_{b2} = 0.622, \kappa = 0.41, \sigma = \frac{2}{3}$$
$$C_{\nu 1} = 7.1, C_{w1} = \frac{C_{b1}}{\kappa^2} + \frac{1 + C_{b2}}{\sigma}, C_{w2} = 0.3, C_{w3} = 2.0 \tag{4.39}$$

4.2.4 Laminar-Turbulent Transition Model

In the current study, a modified $\gamma - \overline{Re_{\theta_t}}$ laminar-turbulent transition model [37] [38] is used to predict the precise locations of the transition on the airfoil surface boundary layer. The original laminar-turbulent transition model was developed by R.B. Langtry and F.R. Menter [39] for the SST (Shear Stress Transport) $k - \omega$ two equation turbulent model [40]. The original version of the $\gamma - \overline{Re_{\theta_t}}$ was modified by S. Medida and J.D. Baeder [37] and coupled to the SA turbulent model. It uses the local intermittency, γ to govern the laminar-turbulent transition in the boundary layer by controlling the amount of turbulent kinetic energy generated.

In the current version of $\gamma - \overline{Re_{\theta_t}}$ transition model [38], γ can be obtained by the following transport equation,

$$\frac{D(\rho\gamma)}{Dt} = P_\gamma - D\gamma + \frac{\partial}{\partial x_j}\left[\left(\mu + \frac{\mu_t}{\sigma_f}\right)\frac{\partial \gamma}{\partial x_j}\right] \tag{4.40}$$

where,

$$P_\gamma = \rho F_{onset} G_{onset} MAX\left(\frac{\Omega}{F_{length}}, \frac{1.0}{F_{length,min}}\right)$$
$$if \gamma > 1.0, P_\gamma = (1-\gamma)P_\gamma \tag{4.41}$$

$$D_\gamma = \rho \Omega \gamma (1.0 - G_{onset}) \tag{4.42}$$

$$G_{onset} = \begin{cases} 1.0, if max(F_{onset}) > 1.0 at a given point \\ 0.0, otherwise \end{cases} \tag{4.43}$$

$$F_{onset} = max(F_{onset2} - F_{onset3}, 0) \tag{4.44}$$

$$F_{onset1} = \frac{Re_\nu}{2.193 Re_{\theta_c}} \tag{4.45}$$

$$F_{onset2} = min(max(F_{onset1, F^4_{onset1}}), 4.0) \tag{4.46}$$

$$F_{onset3} = max(2 - (0.25 R_T)^3, 0) \tag{4.47}$$

$$Re_\nu = \frac{\rho d^2 S}{\mu}, Re_{\theta_c} = 0.62 \overline{Re_{\theta_t}}, R_T = \frac{\mu}{\mu_t} \tag{4.48}$$

$$F_{length} = 40.0, F_{length,min} = 2.5 \tag{4.49}$$

Re_{θ_c} represents the critical Reynolds number and governs the transition onset location. Beyond this, the intermittency increases within the boundary layer. The value of F_{length} determines the length of the transition region. $\overline{Re_{\theta_t}}$ is the Reynolds number based on the local momentum thickness, θ_t, and is given as follows,

$$\overline{Re_{\theta_t}} = \frac{\rho_\infty U_\infty \theta_t}{\mu_\infty} \tag{4.50}$$

The $\overline{Re_{\theta_t}}$ field is dependent on a new transition equation as follows,

$$\frac{D(\rho\overline{Re_{\theta_t}})}{Dt} = P_{\theta_t} + \frac{\partial}{\partial x_j}\left[\sigma_{\theta_t}(\mu+\mu_t)\frac{\partial\overline{Re_{\theta_t}}}{\partial x_j}\right] \tag{4.51}$$

where,

$$P_{\theta_t} = C_{\theta_t}\frac{\rho}{t}(Re_{\theta_t} - \overline{Re_{\theta_t}})(1.0 - F_{\theta_t}) \tag{4.52}$$

$$F_{\theta_t} = min(e^{-(\frac{d}{\delta})^4}, 1.0) \tag{4.53}$$

$$\theta_{BL} = \frac{\overline{Re_{\theta_t}}\mu}{\rho U}, \delta_{BL} = 7.5\theta_{BL}, \delta = \frac{50\Omega d}{U}\delta_{BL} \tag{4.54}$$

The $\overline{Re_{\theta_t}}$ is determined using experimental results while the $\overline{Re_{\theta_{t\infty}}}$ results from a piecewise interpolation of the freestream turbulent value given as in Table 4.1 [41].

Using the table 4.1, when solving the Eq. 4.51 and following equations, $\overline{Re_{\theta_t}}$ can be obtained.

$$Re_{\theta_t} = Re_{\theta_{t\infty}}F(\lambda_\theta) \tag{4.55}$$

$$F(\lambda_\theta) = \begin{cases} -(-12.986\lambda_\theta - 123.66\lambda_\theta^2 - 405.689\lambda_\theta^3)e^{-(\frac{Tu}{1.5})^{1.5}}, if\lambda_\theta \leq 0 \\ 1 + 0.275(1 - e^{-3.5\lambda_\theta})e^{-\frac{Tu}{0.5}}, if\lambda_\theta > 0 \end{cases} \tag{4.56}$$

$$\lambda_\theta = \frac{\rho\theta^2}{\mu}\frac{dU}{ds} \tag{4.57}$$

$$\sigma_f = 1.0, C_{\theta_t} = 0.03, \sigma_{\theta_t} = 2.0 \tag{4.58}$$

Table 4.1: Piecewise linear correlations between turbulent intensity, $Tu\%$ and freestream turbulence, $\overline{Re_{\theta_{t\infty}}}$ [41]

$Tu\%$	$\overline{Re_{\theta_{t\infty}}}$
0.01	1800.0
0.03	1135.0
0.51	894.0
1.33	392.0
2.00	252.0
5.25	165.0
6.50	100.0

4.3 Flow Solvers

In house developed flow solver, GPURANS3D and OVERTURNS are used in the current study. Both solvers are developed in the University of Maryland, featuring above numerical modeling techniques.

4.3.1 GPURANS3D

The parametric studies, shown in the following Chapter, 5 have been conducted using GPURANS3D flow solver. The solver was developed by the University of Maryland. GPURANS3D is a GPU-accelerated FVM (Finite Volume Method) flow solver, which employs a curvilinear, structured, compressible DDES solver.

GPURANS3D was coded using CUDA (Compute Unified Device Architecture) to fit in GPU-accelerated computation [37] [42] [43]. Until the recent days, the best solution to handling high cost CFD simulations was a physically parallelized computation on multiple CPU nodes. However more recently, GPU computations have been receiving attention and developed as an alternative of multi-clustered CPU machines, since one can have even more job threads with one high end GPU machine than with moderate sized multi-clustered CPU machines.

According to recent benchmark tests, by completely solving the RANS-LES using GPU computation, the computation speed can be accelerated up to more than 50 times comparing with a typical single core from CPU based machines. In this research, the Nvidia Tesla K20m GPU cards in the Deep-Thought II computer cluster (located in the University of Maryland) are used [44]. The Nvidia Tesla K20 GPU card is featured 2496 processor cores (processor core clock: 706 MHz), total 5GB board memory (memory clock: 2.6 GHz, bandwidth: 208 GB/sec) [45]. By running on a single GPU card versus running using MPI on a CPU cluster there is no domain partitioning required for the current simulations.

4.3.2 OVERTURNS

For the isolated rotor simulations, the OVERTURNS solver is used. The OVERTURNS (Overset Transonic Unsteady Rotor Navier-Stokes) is CPU-based, structured, finite-volume, compressible, Navier-Stokes solver which was developed also at the University of Maryland.

In the current study, the third-order accurate MUSCL (Monotonic Upwind Scheme for Conservation Laws) scheme with Korens limiter [46] [47] is used for spatial reconstruction of primitive variables and second-order accurate implicit BDF (Backward Differentiation Formula) is used for time integration. The governing equations are linearized and solved using the LUSGS (Lower-Upper Symmetric Gauss Seidel) approximate factorization method [48]. Dual time-stepping is employed to minimize factorization errors. Roes approximate Riemann solver [49] is used to evaluate inviscid flux terms and a second-order accurate central difference scheme is used to evaluate viscous flux terms. The one-equation Spalart-Allmaras turbulence model [36] combined with the $\gamma - \overline{Re_{\theta_t}}$-SA transition model [37] is used for computing the eddy viscosity field. Turkels low-Mach preconditioner [50] is used to improve convergence and accuracy in the low-speed flow regime.

Chapter 5: Design Parametric Study

The idea of the span-wise wavy trailing edge looks promising. However, there are many unknown characteristics needed to be revealed, to apply for the real wind turbine or rotational wing applications. First of all, appropriate trailing edge wave size is the most key unknown. As like to the vortex generators, a proper trailing edge sizing must be the key to the best aerodynamic design (in this case, large drag reduction with small lift loss). For the better understandings of the design characteristics of the span-wise wavy trailing edge, a design parametric study has been conducted. The definition of the best aerodynamic and aero-acoustic wind turbine blade design might be defined with the characteristics of ***less drag - more lift - quieter sound***. Considering these terms, the best way to design the span-wise wavy trailing edge is discussed, in the current chapter. Quantification of the aerodynamic and acoustic performance of the various wavy trailing edge design is carried out, and design qualification is discussed based on the quantified airfoil performances. According to the previous studies (Table 1.5), the add-on type drag reduction devices reduce the drag and tonal noise of the flatback airfoils up to 50% and 12 dB, approximately [21] [22]. These values must be reasonable criteria to compare the performance of the current span-wise wavy trailing edge designs.

5.1 Design Parameters

As we discussed in Chapter 3.2.2, there are three key design parameters for the appropriate sizing of the span-wise wavy trailing edge; 1) **wave depth** 2) **wave length** 3) **wave portion**. In the current chapter, various patterns and sizes of the span-wise wavy trailing edge are tested to reveal the aerodynamic and acoustic effect of the key design parameters. Based on the results, a proper wave size for the best aerodynamic and aero-acoustic performance is determined.

5.2 Case Studies

In the current parametric study, quasi 3-D airfoils are used. The quasi 3-D airfoils are wing segments generated by span-wise extrusion of 2-D airfoil. Thus, there are no changes of the chord length and wing taper in the span direction. All the airfoil geometries used in the parametric study are created by 0.5 chord length extrusion in the span direction.

5.2.1 Tested Airfoil Trailing Edge Geometries

For the baseline cases, a flatback airfoil and a sharp trailing edge airfoil are tested. Overall, 16 different patterns of the span-wise wavy trailing edge variations including 12 different patterns of the maximum portion of wavy trailing edge, and 4 different patterns of the less portion wavy trailing edge are tested.

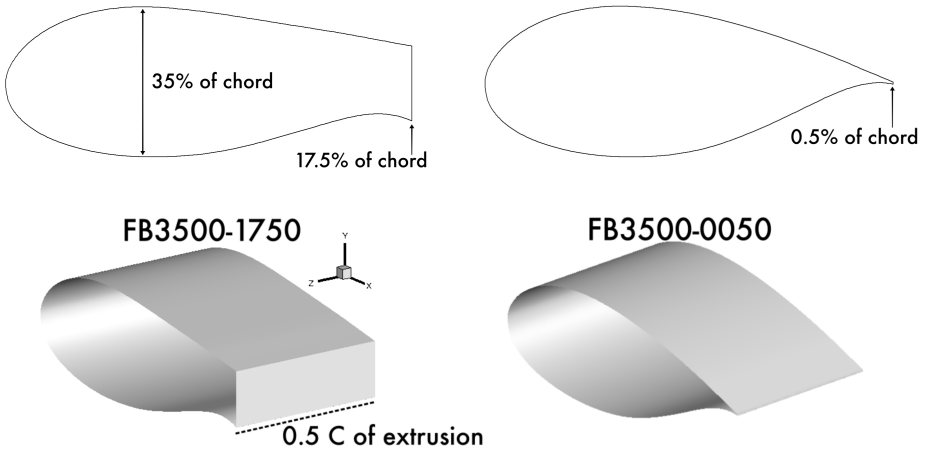

Figure 5.1: Geometries of baseline airfoil: FB3500-1750 (thick-flatback) and FB3500-0050 (thick-sharp trailing edge)

5.2.1.1 Baseline airfoils

As baseline airfoils, the FB3500-1750 and FB3500-0050 airfoils are used. Both airfoils belong to the FB3500 airfoil series. FB3500-0050 is a thick airfoil which has a conventional sharp trailing edge, but its thickness is much larger than the conventional airfoils. The thickness of the FB3500-0050 is 35%c, and the trailing edge thickness is 0.5%c. The FB3500-1750 is a flatback version of FB3500 airfoil. The airfoil thickness of the FB3500-1750 is same as the other airfoils in the FB3500 series, but its trailing edge thickness is 17.5%c. The airfoil coordinates of these two airfoils are presented in Figure 1.7. Those airfoil coordinates are kindly provided by J.P. Baker and C.P. van Dam of UC Davis. The quasi 3-D airfoil geometries (0.5c extrusions of the airfoils) of the baseline airfoils are presented in Figure 5.1.

5.2.1.2 Maximum portion wavy trailing edge airfoils

In the beginning of the current study, maximized trailing edge wavy modifications on the baseline airfoil are considered, in order to maximize the wavy trailing edge effect and to get more clear differences between the various sizes of the trailing edge waves. Later in the current parametric study, the less portion wavy modifications are investigated in order to enhance the design efficiency and acquire potential structural design benefits. The maximum portion of the wavy trailing edge airfoils modify all the adverse pressure gradient regions where the location between maximum thickness and the trailing edge. (*illustrated in* Figure 5.5)

Total twelve maximum portion wavy trailing edge designs are considered for the current parametric study. The twelve airfoil geometries are created by combinations of two major wavy design parameters; 'wave length' and 'wavy depth'. Four steps of the wave lengths are investigated, as shown in Figure 5.2. For the parameter, 'wave depth', three different wave depths are investigated, as shown in Figure 5.3. Twelve test cases of the maximum portion span-wise wavy trailing edge designs are shown in Figure 5.4. In the figures, each airfoils are named with the naming notation presented in the previous section 3.2.3.

5.2.1.3 Less portion wavy trailing edge airfoils

The idea of the less portion wavy trailing edge airfoil is a stem from the structural concerns of the maximum portion wavy trailing edge. Figure 5.5 describes typical spar locations in the modern wind turbine blades. In the most popular blade

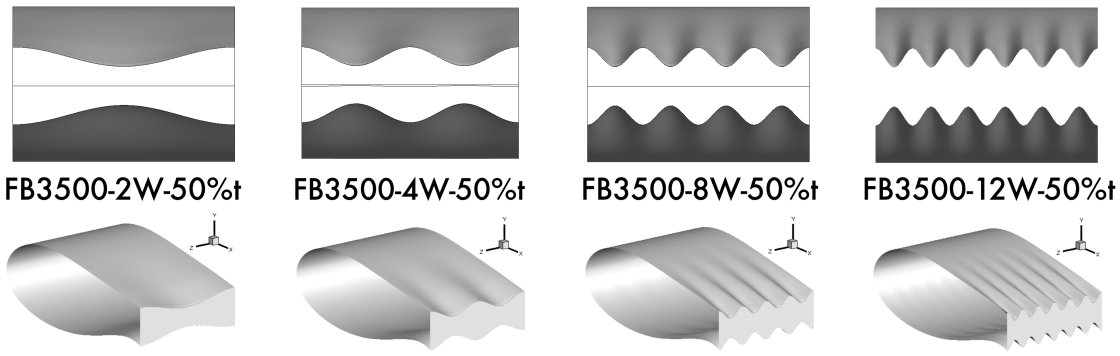

Figure 5.2: Four steps of the wave length for the current parametric study

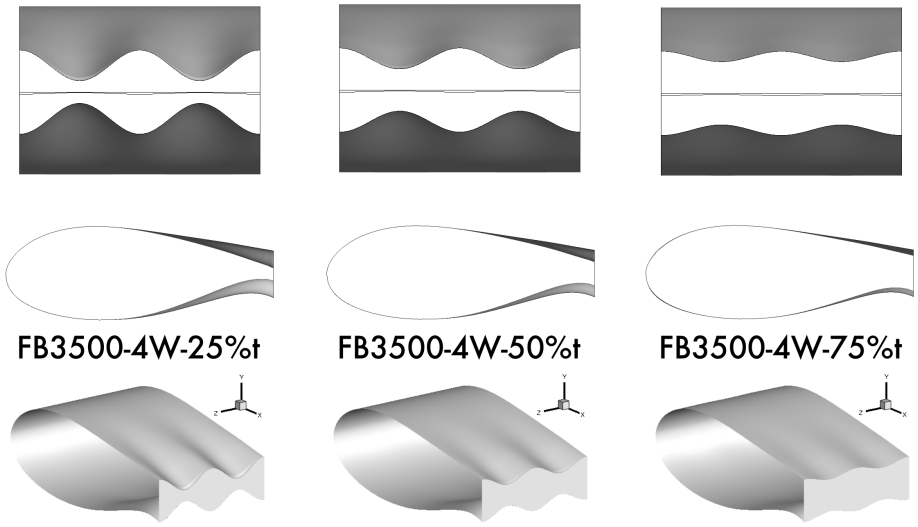

Figure 5.3: Three steps of the wave depth for the current parametric study

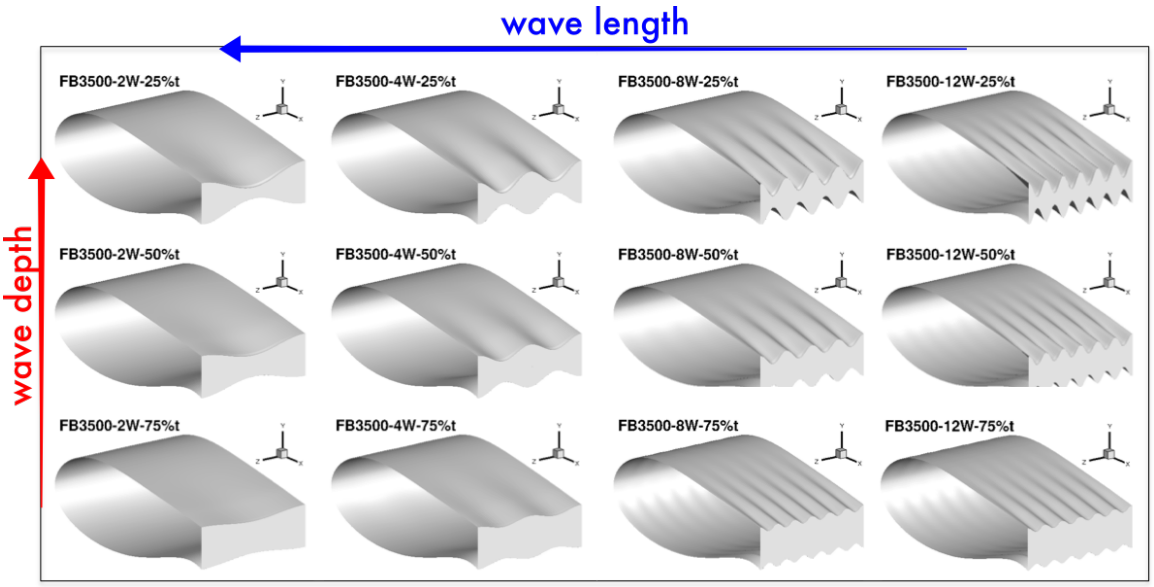

Figure 5.4: Geometries of the maximum portion wavy trailing edge airfoils

designs, the wind turbine blades are designed with two spar structures. The first and second spars usually locate near the aerodynamic center line. However, some of the modern large blades have an additional spar (third) at the relatively closer location to the trailing edge as also shown in Figure 5.5.

Regarding it, the maximum portion wavy trailing edge design may differ the third or even the second blade spar locations. In this case, it may undermine the structural robustness of the wind turbine blade and may result in the structural failure during the turbine operation.

However, if one modifies the blade from 90% of the chord to the trailing edge (in other words, last 10% of the chord) instead of modifying the whole regions of adverse pressure gradient, the blade modification will not affect to any of the blade spars as shown in Figure 5.5.

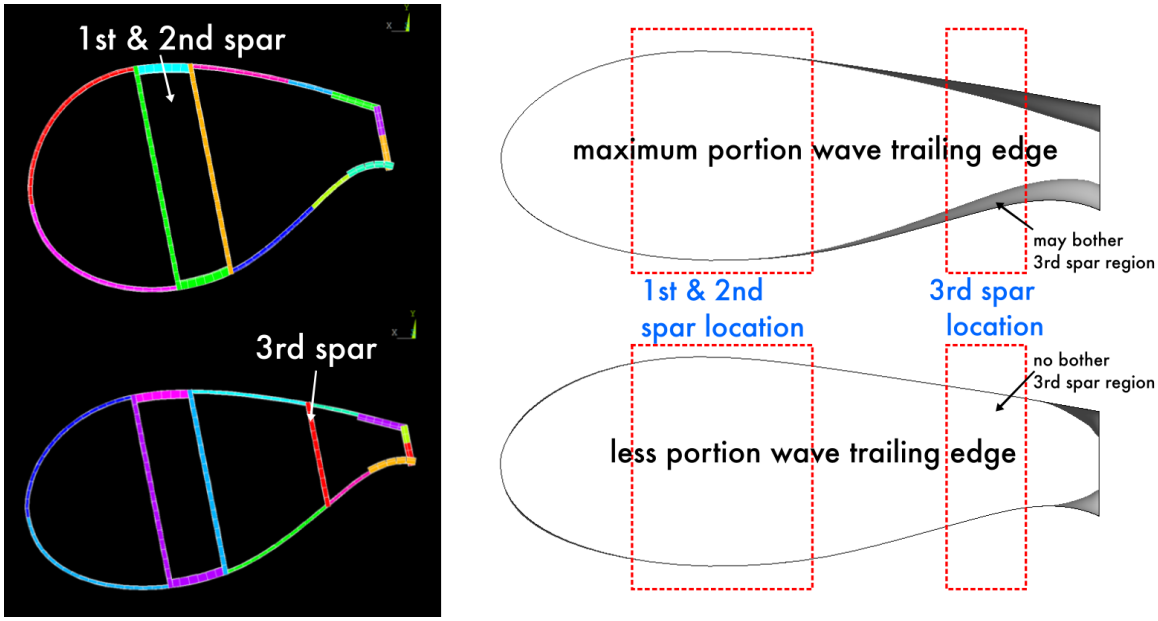

Figure 5.5: Spar locations of the modern wind turbine blade and the maximum and the less portion of wavy trailing edge modifications

Based on the idea, two different types of the less portion wavy trailing edge designs are developed as shown in Figure 5.6. The first type of the less portion wavy trailing edge design modifies only the last 10% of airfoil. Thus, it is tagged with '10%c' on the name of airfoil. The second type of the less portion wavy trailing edge design differs the airfoil, same as the maximum portion wavy trailing edge, but it only modifies the pressure side of the airfoil. Thus, it is called as 'halfway cut' wavy trailing edge, and tagged with 'half' on the name of the airfoil. For the less portion wavy trailing edge, only four variations of the geometries are considered, as presented in Figure 5.6.

Based on the idea, a total sixteen design variations of the span-wise wavy trailing edges are considered in the current parametric study. The specifications of

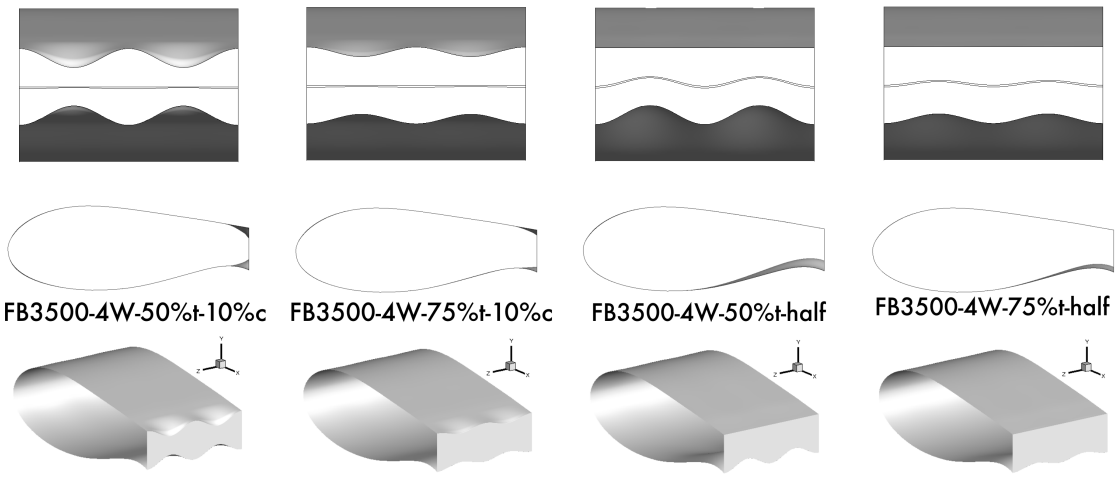

Figure 5.6: Geometries of the less portion wavy trailing edge designs

the tested airfoils are described in Table 5.1.

Table 5.1: Specifications of the wavy trailing edge airfoils used in the parametric study

Airfoil	Wave length	Wave depth	Wave portion
FB3500-1750	baseline (flatback)	N/A	N/A
FB3500-0050	baseline (sharp trailing edge)	N/A	N/A
FB3500-2W-75%t	2 waves / c (0.5c)	25% of t_{te}	from 0.25 to 1.0 x/c
FB3500-2W-50%t		50% of t_{te}	
FB3500-2W-25%t		75% of t_{te}	
FB3500-4W-75%t	4 waves / c (0.25c)	25% of t_{te}	from 0.25 to 1.0 x/c
FB3500-4W-50%t		50% of t_{te}	
FB3500-4W-25%t		75% of t_{te}	
FB3500-8W-75%t	8 waves / c (0.125c)	25% of t_{te}	from 0.25 to 1.0 x/c
FB3500-8W-50%t		50% of t_{te}	
FB3500-8W-25%t		75% of t_{te}	
FB3500-12W-75%t	12 waves / c (0.083c)	25% of t_{te}	from 0.25 to 1.0 x/c
FB3500-12W-50%t		50% of t_{te}	
FB3500-12W-25%t		75% of t_{te}	
FB3500-4W-75%t-10%c	4 waves / c (0.25c)	25% of t_{te}	from 0.9 to 1.0 x/c
FB3500-4W-50%t-10%c		50% of t_{te}	
FB3500-4W-75%t-half	4 waves / c (0.25c)	25% of t_{te}	from 0.25 to 1.0 x/c
FB3500-4W-50%t-half		50% of t_{te}	

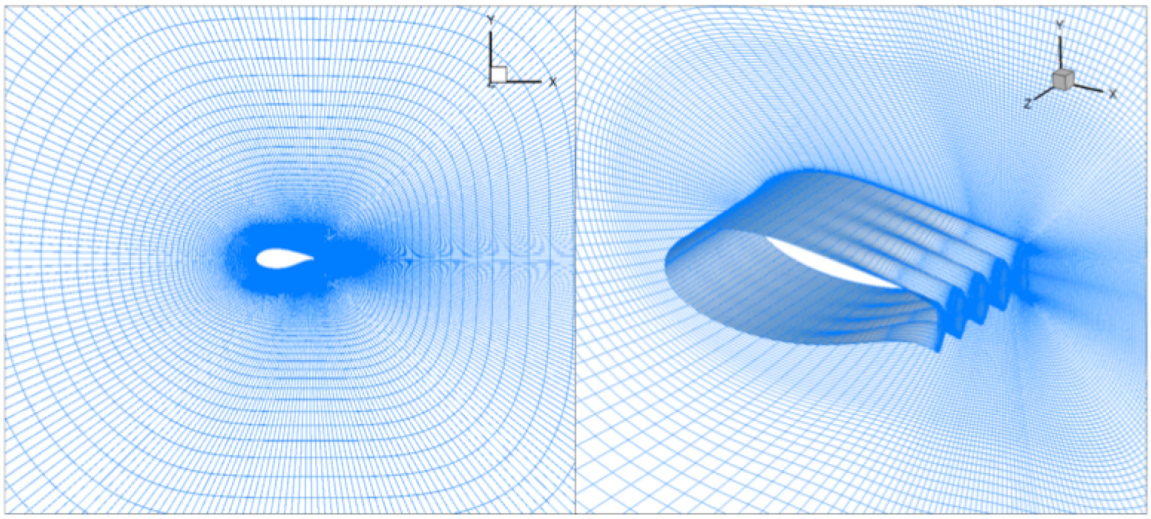

Figure 5.7: Computational mesh of the parametric study which is constructed in structured O-mesh topology, mesh points $271 \times 141 \times 61$

5.2.2 Mesh Description

Computational meshes used in the current study are created using an algebraic mesh generation method. Each individual meshes for the sixteen airfoils are constructed with a single block, structured O-mesh topology. A mesh used in the current parametric study is presented in Figure 5.7. Each of those meshes are constructed of $271 \times 141 \times 61$ mesh points in the wrap around, the normal to the surface and the span-wise direction, respectively. Thus, a total 2.33 million mesh points are used for the each airfoil segment computation. The overall extent of the mesh is around 50c in the normal to the surface direction, and 0.5c of extrusion in the span direction. At the airfoil surface, the lowest grid cell distance is about $\Delta y/c \approx 0.5 \times 10^{-6}$, and y^+ is 0.8.

5.2.3 Initial and Boundary Conditions

5.2.3.1 Initial conditions

For the current parametric study, the initial and boundary conditions for the computational domains are assigned as follows. For the initial flow condition, the freestream Mach number, $M_\infty = 0.3$ is set as a starting value and assigned at the every points in the computational domain.

The boundary conditions are assigned at the each boundaries of the computational domain as described in Figure 5.8. At the airfoil surface, the viscous wall boundary condition is assigned. In the given O-mesh, the first and the last edges in a wrap-around direction are collapsed in a line at the airfoil wake region. These edges are assigned as the periodic boundary conditions. The outer boundary of the computational domain is assigned as the far-field boundary condition. The periodic boundary conditions are assigned at both end edges in the span-wise direction.

5.2.3.2 Periodic boundary condition

A periodicity employs ghost cells to carry the density, pressure, and velocity values over from the boundary of the mesh to the corresponding physical points at the far boundary of the mesh. The current work employs the periodicity at O-grid collapsing line (at the trailing edge) and at the both right and left side of the mesh, as illustrated above in Figure 5.8. The mesh contains ghost cells at the beginning and the end of the mesh, allowing the third and fifth order spatial schemes to be

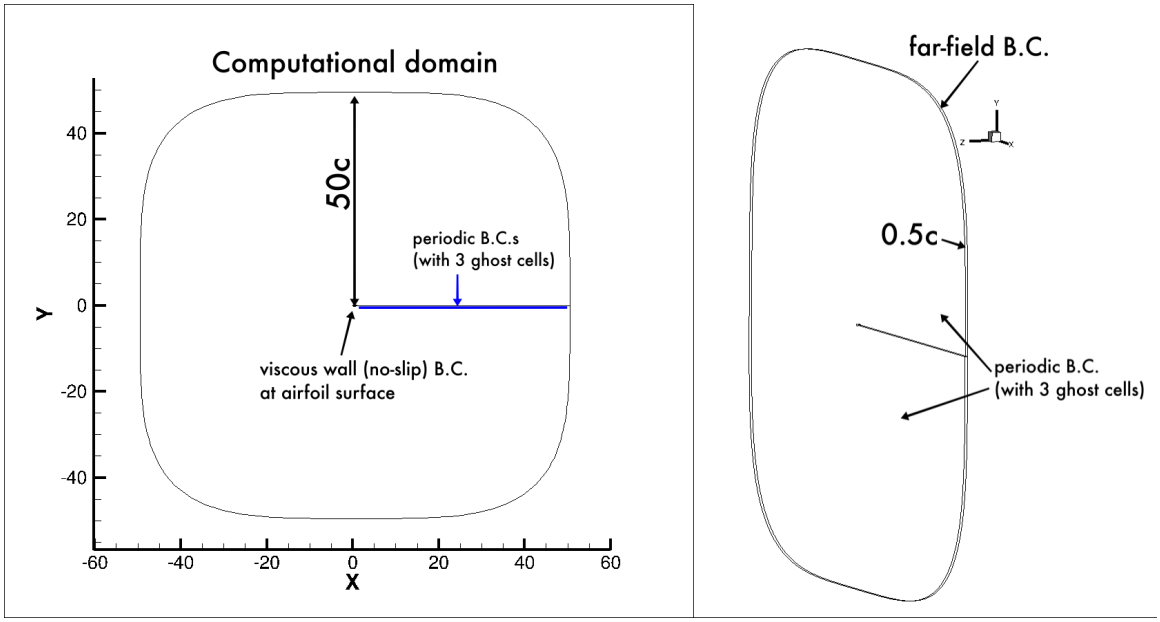

Figure 5.8: Dimensions of the computational domain and assigned boundary conditions

employed at the edges of the physical mesh by using information calculated at the corresponding physical cell to the ghost cell.

5.2.3.3 Wall boundary condition

At a solid wall, such as the airfoil surface, the density is extrapolated from the interior points of the computational domain. Viscous conditions at the wall dictate that the velocity of flow relative to the wall is zero, fulfilling the no-slip condition. With this restriction in mind, the pressure is given by the normal momentum equation. If the flow near the wall is inviscid, the velocity components of the flow are extrapolated from the computational domain to the surface. Furthermore, the no-penetration condition must be enforced, ensuring that there is no flow through the

solid boundary. This is accomplished by setting the contra-variant component of velocity in the wall normal direction equal to the surface velocity.

5.2.3.4 Far-field boundary condition

Far-field boundaries are artificial boundaries, and necessary because the computational domain has a finite size. Those boundaries are placed far enough from solid bodies within the flow such that no outgoing behavior is reflected back into the domain to interfere with the flow. Previous works have shown that placing the boundaries 20-30 chord lengths or more from any body surfaces ensures that no non-physical behavior is created [51]. Non-reflecting boundary conditions are achieved using the Riemann invariants to propagate ingoing or outgoing waves. In regions where the flow is outgoing, the Riemann invariants are extrapolated from interior cells; while in the regions of ingoing flow freestream values are extrapolated from. Due to the distance from the excited flow, numerical dissipation causes strong gradients to diminish before reaching the domain boundary. Furthermore, the mesh is stretched in the outer regions of the domain, assisting with the dissipation of strong gradients. This dissipation has the potential to negatively impact the solution unless care is taken to create a large enough computational domain to separate the majority of the flow and the outer boundaries.

5.2.4 Aerodynamic Characteristics of Span-wise Wavy Trailing Edge

Unsteady DDES is performed under the test conditions of the flight Mach number 0.3, a Reynolds number 666,000, time step 0.001 sec, and a range of angles of attack 0° to 20°. Uniform inflow condition is assumed with a stationary airfoil pitch. The test conditions are presented in Table 5.2. The main objective of the current parametric study is to figure out the design criteria of the appropriate wave sizing for the best aerodynamic, aero-acoustic and structural performance. In the first step to accomplish the objective, aerodynamic characteristics of the baseline airfoils and various wavy trailing edge airfoils are compared each other.

Table 5.2: Test conditions of the parametric study

Reynold No.	Mach No.	Time-step (sec)	Angle of attack (°)
666,000	0.3	0.001	0 - 20

5.2.4.1 Baseline airfoil cases

For the comparison, the FB3500-1750 (flatback) and the FB3500-0050 (sharp trailing edge) airfoils are tested as a baseline airfoils. The DDES results of current CFD solver (GPURANS3D) are validated with the experimental data, published by J.P. Baker and C.P. van DAM [15]. The experiments have been conducted in the University of California at Davis' aeronautical wind tunnel. The snap shot of the wind tunnel and the tested airfoil segment are presented in Figure 5.9. The airfoils are tested under assumptions of the both free and fixed boundary layer laminar-

Figure 5.9: U.C.Davis' aeronautical wind tunnel (image courtesy of U.C.Davis' web page) [52] and tested FB3500 series airfoil segment (image courtesy of Baker et al.) [15]

turbulent flow transition.

In the current CFD, the DDES with SA turbulent model is performed featuring a laminar-turbulent transition model. Figure 5.10 shows the time-averaged lift and drag predicted by the DDES comparing with the experimental results. In the flatback airfoil case (FB3500-1750), the DDES tends to predict the lift higher than the experiment near the separation curve (at the ranges of angle of attacks between 12° and 20°). This large deviation is caused by the delayed prediction of flow separation onset that commonly happens in the DDES. However, the drag is not much different in these range of the angle of attack, compared to the experimental results.

In the sharp trailing edge case (FB3500-0050), the DDES predicts the both lift and drag very close to the experimental data, even at the high angles of attack region.

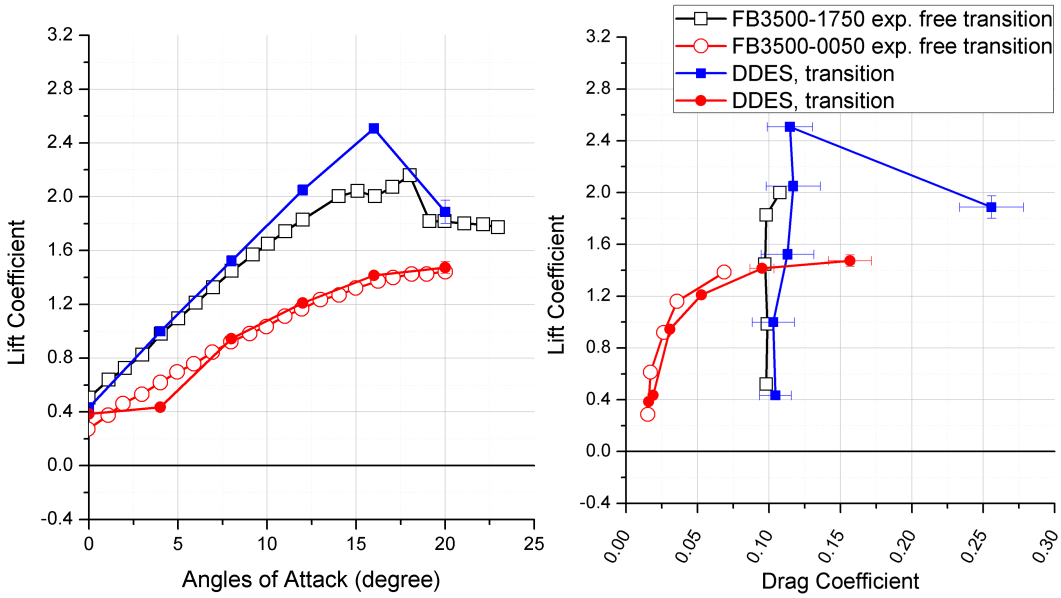

Figure 5.10: Comparison between CFD (DDES) and experimental result [15]: lift and drag of baseline airfoils; M=0.3, Re=666,000, free transition

From the figure, one can easily notice the flatback trailing edge increases the lift of airfoil a lot (in the current particular case, about 100% increase). However, the problem is that drag also increases a lot, too (also about 100-300% increase in the current case). To benefit the aerodynamic performance of wind turbine blades, one may want to maximize the lift while minimizing the drag.

The y-momentum (ρv) contours in Figure 5.11 show the difference in the trailing edge vortex shedding between the flatback and sharp trailing edge airfoil. The vortex shedding strength is much stronger in the flatback airfoil comparing to the sharp trailing edge. The strong vortical flow causes the drag increase by more than twice compared to the sharp trailing edge at the range of the angles of attack 0° to 8°.

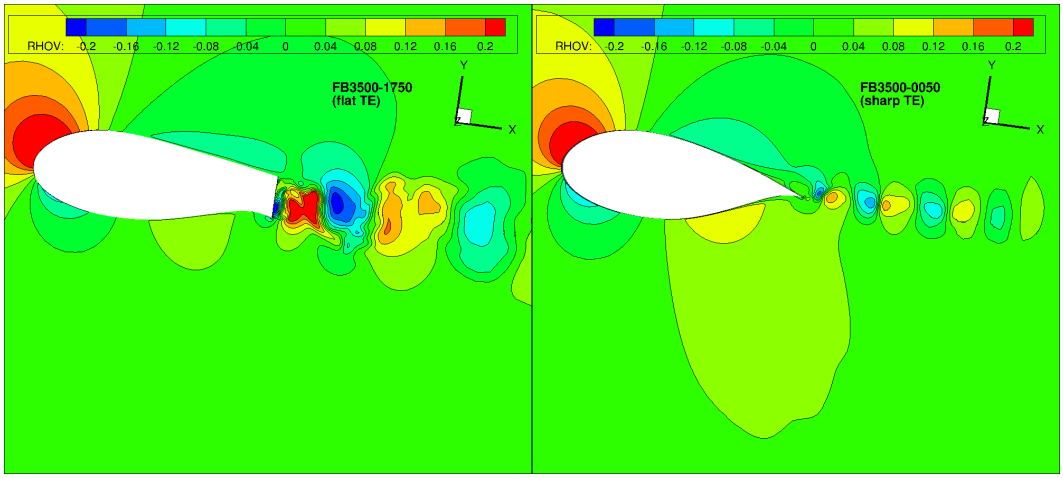

Figure 5.11: Comparison between the flatback and sharp trailing edge airfoil at AoA 8°: trailing edge vortex structure

Figure 5.12 presents the flow separation onset of the flatback and the sharp trailing edge airfoils along a range of angle of attack. As presented in Figure 5.12. at the higher angles of attack, the sharp trailing edge airfoil gets more vigorous flow separation at the most of adverse pressure gradient regions in the airfoil. This massive flow separation on the suction side of the airfoil also increases the drag as shown in Figure 5.10. The drag increase and the lift loss of the sharp trailing edge depend on the growth of the suction side flow separation. However, the drag of the flatback airfoil is mostly pressure drag caused by the trailing edge recirculation flow. Thus, it does not change much at a range of angles of attack, 0° to 16°, but immediately increases at the angle of attack 20°, where the flow separation onsets.

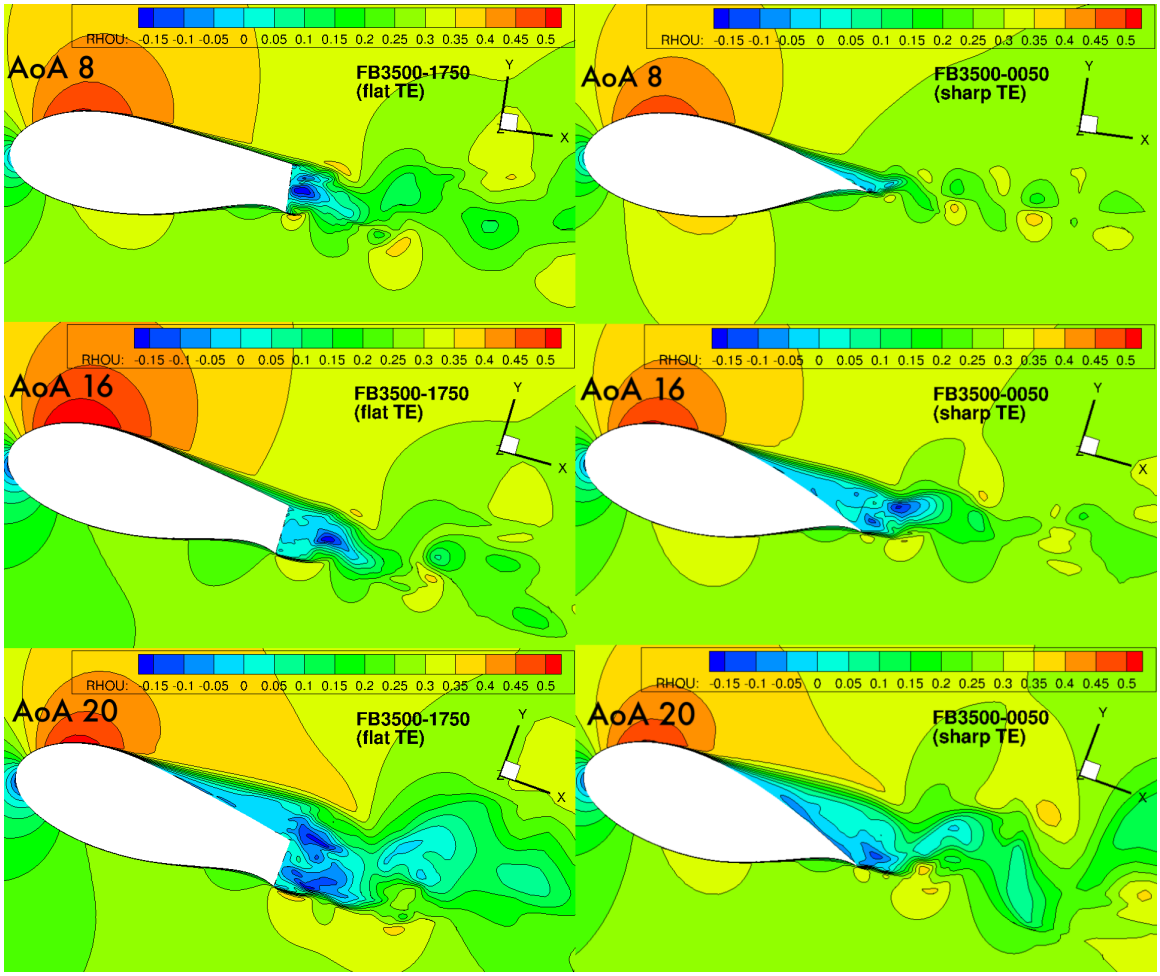

Figure 5.12: Flow separation onset of the flatback and sharp trailing edge airfoils along the angle of attack changes

5.2.4.2 Lift and Drag of span-wise wavy trailing edge airfoils

Aerodynamic performances of the various span-wise wavy trailing edge airfoils are discussed in this section. Computational setups of the current simulations are the same as the baseline cases. In Table 5.3 and 5.4, computed lift, drag and pitching moment coefficients of the tested airfoils at the angle of attack, 8° are presented.

To provide direct insights of the aerodynamic performance of the various airfoil design, the computed results are mapped in Figure 5.13. The lift and drag in the figure are time-averaged, and measured at the angle of attack, 8°. At this angle of attack, moderate flow separation occurs on the surface of FB3500-0050 (sharp trailing edge) while fully attached flow occurs with the FB3500-1750 (flatback). In the lift-drag chart, it is found that some of the wavy trailing edge designs (in the blue circle) such as the FB3500-4W-75%t produce larger lift to drag ratio compared to the baseline airfoils, while the other wavy trailing edge airfoils show the less aerodynamic benefits. The other wavy modifications such as the FB3500-12W-75%t generate the lift as much as the flatback airfoil does, but small amount of the drag reduction decreases the overall lift to drag ratio. Contrarily, the rest of wavy modifications such as the FB3500-4W-25%t also do not so much benefit since they lose too much lift force, in spite of the large drag reduction.

The result implies that there may be a certain criteria of the wave design parameters to benefit the aerodynamic performance.

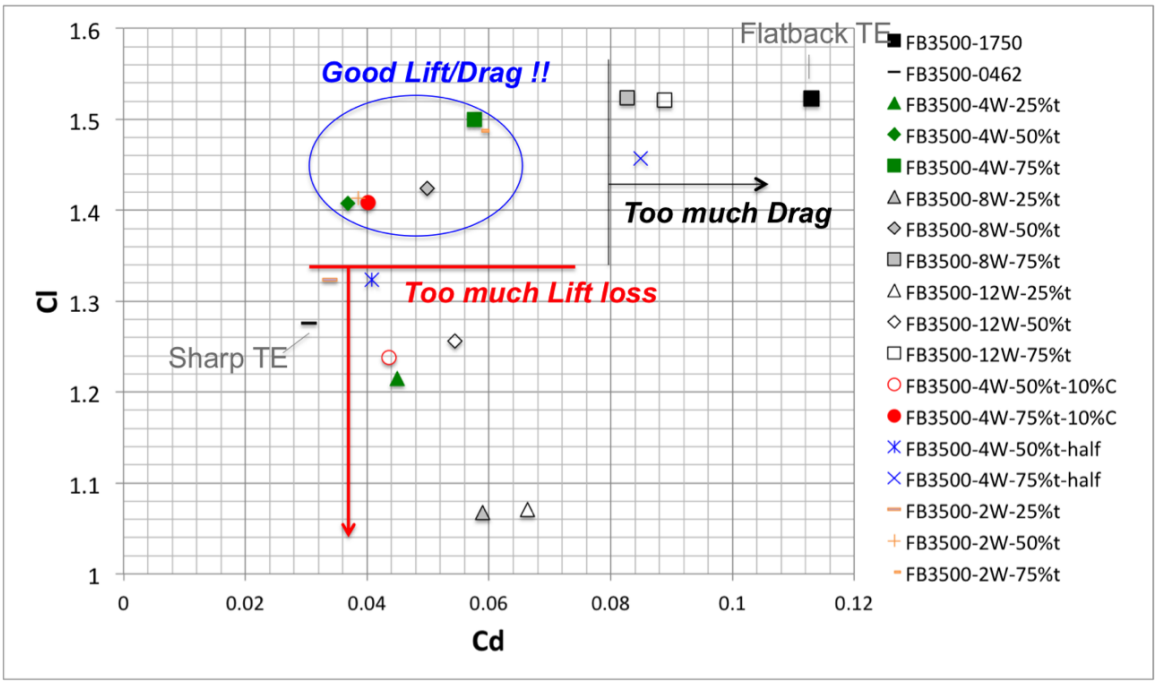

Figure 5.13: Time-averaged lift and drag of the various span-wise wavy trailing edge airfoils, at angle of attack 8°

5.2.4.3 Effect of wave depth and length on aerodynamic performance

To verify the aerodynamic contributions of the wave depth and length, the lift and drag of the twelve maximum portion of the wavy trailing edge airfoils are compared in the current section.

Recalling the previous baseline cases, at the given angle of attack 8°, the drag of the FB3500-1750 is almost 4 times larger than the FB3500-0050. And the lift of the flatback airfoil is about $Cl \approx 1.5 - 1.6$ and $Cl \approx 1.0$ in the sharp trailing edge airfoil. This means the flatback trailing edge benefits about 37.5% of the lift by preventing flow separation mostly. These aerodynamic values of the baseline airfoils must be reasonable references to judge the aerodynamic performance of the various wavy trailing edge airfoils.

The relations between the aerodynamic performance and the wave parameters are presented in Figure 5.14.

(a) In the left figure, the lift of the wavy trailing edge airfoil is inversely proportional to the wave depth (square-deep, circle-medium, triangle-shallow). In other words, simply the deeper waves lose the more lift than the shallower waves.

The 75%t wavy trailing edge (green-triangle) decreases the lift only a slight amount (approximately 7%), and there is not so much changes of the lift with the wave length variation.

Now, looking at the lift of the 50%t wavy trailing edge, the lift is decreased

approximately 12.5% compared to the flatback airfoil for the most of wave lengths (2W - 8W). It is probably a notable aerodynamic loss, but it is still the much larger lift than the sharp trailing edge. With this wave depth, the wave length does not affect significantly until it is shorten by 8 waves per chord. However, beyond this point, the lift immediately drops by another 10% (so 22.5% of the lift drop compared to the flatback airfoil).

Unlikely with the shallower depth wavy trailing edges, the lift of the deepest wave, 25%t is much eager to be affected by the wave length variation. The lift of this modification decreases as the wave length is getting shorter. In the worst case, the lift loss is about 35%.

Summarizing those results, in the perception of the lift, effect of the wave length is strongly dependent to the wave depth.

(b) The figure in center shows the effect of the wave parameters on the drag. In figure, the drag decreases linearly as the wave length increases, regardless of the wave depth variation, until the wave length becomes 0.25c. Beyond that point, the drag does not much change with the wave length. For the shorter than 0.25c of wave length (for examples, 8W and 12W), the drag increases linearly up to 150% as the wave length decrease.

Looking at the relations between the drag and the wave depth, the shallow wavy trailing edge (75%t) reduces about 50% of the drag compared to the flatback airfoil. However, the medium wave depth (50%t) works great to reduce the drag. There is about 70% of the drag reduction compared to the

flatback, and this is about the 5% more drag reduction even compared to the deepest wavy trailing edge (25%t).

(c) In the right figure, the lift to drag ratios are plotted with the wave length and depth variations. One might notice the plots in this figure are very similar to the plots of the drag (figure in center) if it is inverted. That because of the drag reductions are much larger than the lift losses for the most of the wavy trailing edge designs.

The lift to drag ratios prove the design criteria of wave parameters. Based on the results, to ensure the aerodynamic benefit at least 0.25c of wave length is required, and the 50%t might be the limit in the wave depth.

From the results, one can find that the properly designed span-wise wavy trailing edge improves the aerodynamic performance of flatback airfoil by reducing the drag more than the lift loss. For this, the lift must not be changed too much and the drag must be reduced as much it can be. For the reason, the wave depth, 75%t may not be a good design because of the relatively large drag. In the contrast, the wave depth, 25%t also may not be a proper design, because of the too much lift loss and the large drag. The wave depth, 50%t, the drag is minimum and the lift is relatively larger compared to the other wave depths.

5.2.4.4 Effect of wavy portion on aerodynamic performance

In the current section, effect of the wavy portion on the aerodynamic performances are investigated. In the previous section, the maximum portion wavy

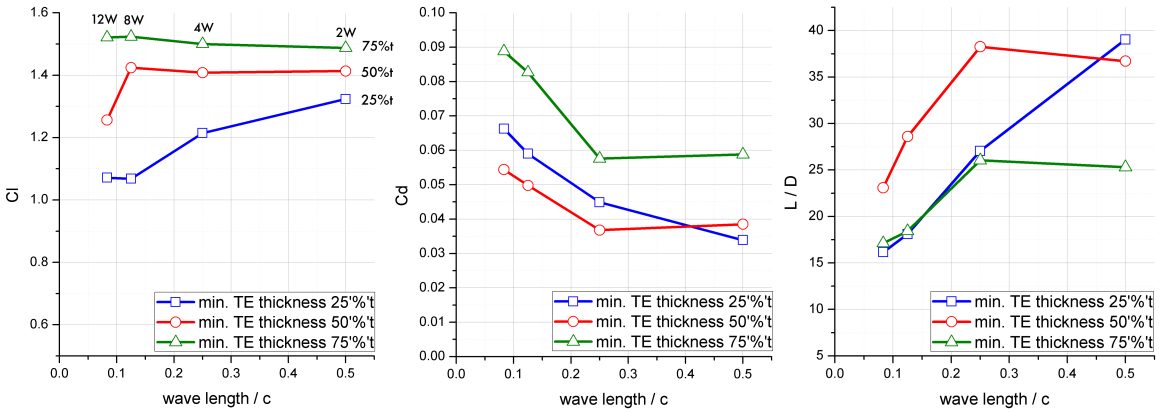

Figure 5.14: Effect of the wave parameters on the aerodynamic force: the lift, drag and lift to drag ratio

modifications are explored. Along with the study, two types (90%c and halfway cut) of the less portion wavy trailing edges are considered in the current section. The test conditions are the same as the previous cases.

Figure 5.15 compares the lift-drag polar of the simulated wavy trailing edges. For the reference, the lift-drag polar of the regular straight trailing edge airfoils the FB3500-1750 (flatback, t=17.5% of c), the FB3500-0462 (less flatback, t=4.62% of c), the FB3500-0050 (sharp trailing edge, t=0.5% of c) are plotted.

On the left column of figure, results of the two maximum portions wavy trailing edge airfoils (the 4W-75%t and the 4W-50%t) are presented. On the center column of the figure, results of the two 10%c less portion wavy trailing edge airfoils are presented. Lastly, on the right column, results of the two halfway cut less portion wavy trailing edge airfoils are presented.

(a) For the wave depth, 75%t, airfoils, comparing to the maximum portions of the wavy trailing edge, the 10%c less portion wavy trailing edge reduces the drag

more, as it retains the lift with only a slight loss. The halfway cut wavy trailing edge produces the much higher lift at the high angles of attack, because the flow is more attached on the suction side of the trailing edge. However, there is not so much drag reduction in the halfway cut - shallow wave depth case.

(b) For the wave depth 50%t cases, the maximum portions of the wavy modification and the 10%c less portion wavy trailing edge lose too much lift force, in spite of the such a large drag reduction. In this wave depth, only the halfway cut wavy trailing edge performs effectively (large drag reduction-small lift loss).

Therefore, among the trailing edge modification designs, the less portion wavy modifications, 4W-75%t-10%tc and 4W-50%t-half are the best aerodynamic performance designs. In a perception of the wind turbine blade design, the 10%c modification might be a better selection than the halfway cut modification, since it does not differ any structural design near the shear web regions. Obviously, transforming the shear webs are not the best idea, because it will make the structural characteristics of the wind turbine blade changed.

5.2.4.5 Drag and trailing edge vortex shedding

Drag reduction by well designed span-wise wavy trailing edge airfoil is about 60% of the flatback airfoil drag. According to the previous understandings of the blunt trailing edge aerodynamics, the major contributor of the large drag of the blunt trailing edge is a strong standing vortical flow formed at the trailing edge

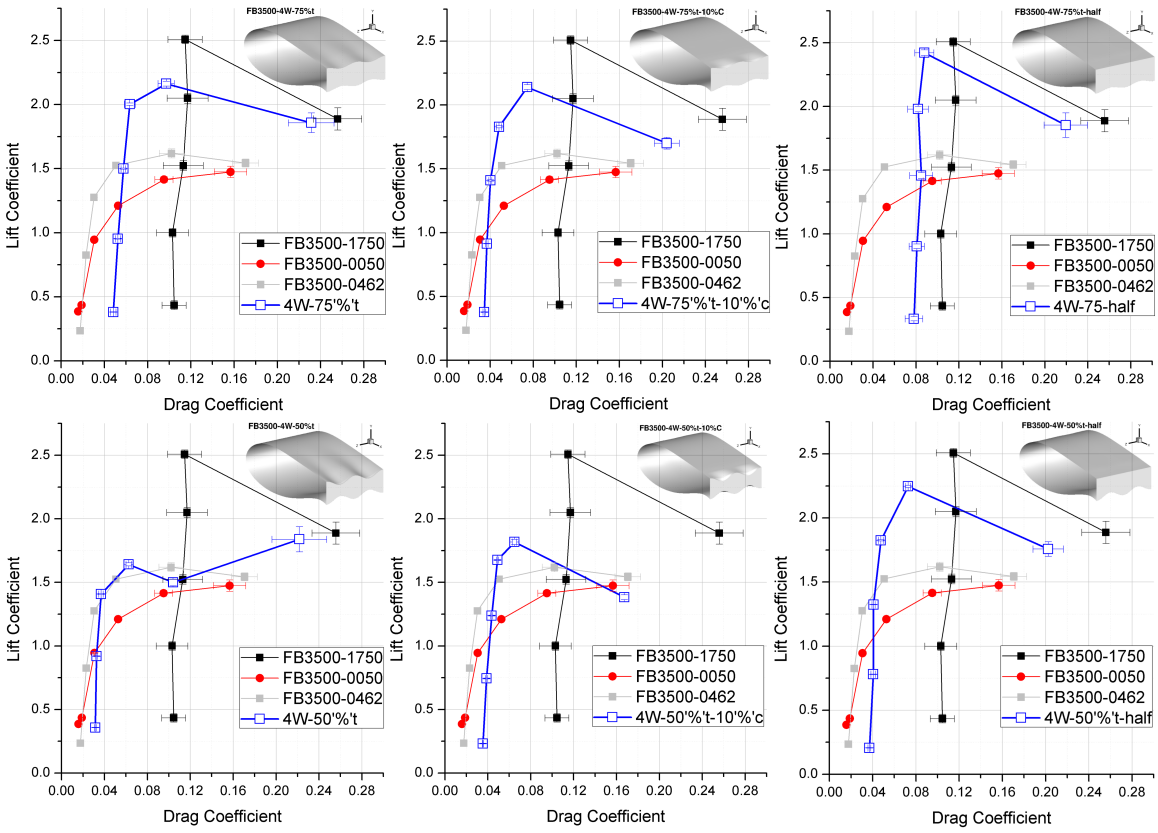

Figure 5.15: Lift-drag polars of the maximum and less portion wavy trailing edge airfoils

region [12] [13]. For the reason, the current wavy trailing edge and the most of previous drag reduction add-ons are designed to eliminate or detach the standing flow from the trailing edge region.

(a) In Figure 5.16 and 5.17, the vortex structures and the drag coefficient of the several wavy trailing edge airfoils are presented. In Figure 5.16, the drag of the 4W-75%t-10%c and the 4W-50%t-10%c airfoils are 64% ($Cd = 0.0402$) and 61% ($Cd = 0.0436$) less than the drag of the flatback airfoil ($Cd = 0.1130$). Trailing edge vortex structures of the both airfoils are less coherent in the span-wise direction, compared to the flatback airfoil, and the strong vortical flow is formed at much far downstream from the trailing edge.

(b) In the halfway cut less portion wavy trailing edge design, the drag of the 4W-50%t-half airfoil is also about 64% ($Cd = 0.0408$) less than the drag of flatback airfoil, and the formation of the trailing edge vortex structure is similar to the above two airfoils. However, comparing to the result, the trailing edge vortex structure of the 4W-75%t-half is much more coherent in the span-wise direction, and the strong vortical flow is standing at the right close to the trailing edge. This is almost identical to the trailing edge vortex of the flatback airfoil. In this case, the drag coefficient is measured as 0.0849, and this is only 25% less value than the flatback airfoil drag.

Based on the results, one can conclude that the drag reduction of the wavy trailing edge depends on the formation of trailing edge vortex shedding, such as a strength of the standing vortical flow and a distance of the vortical flow from the

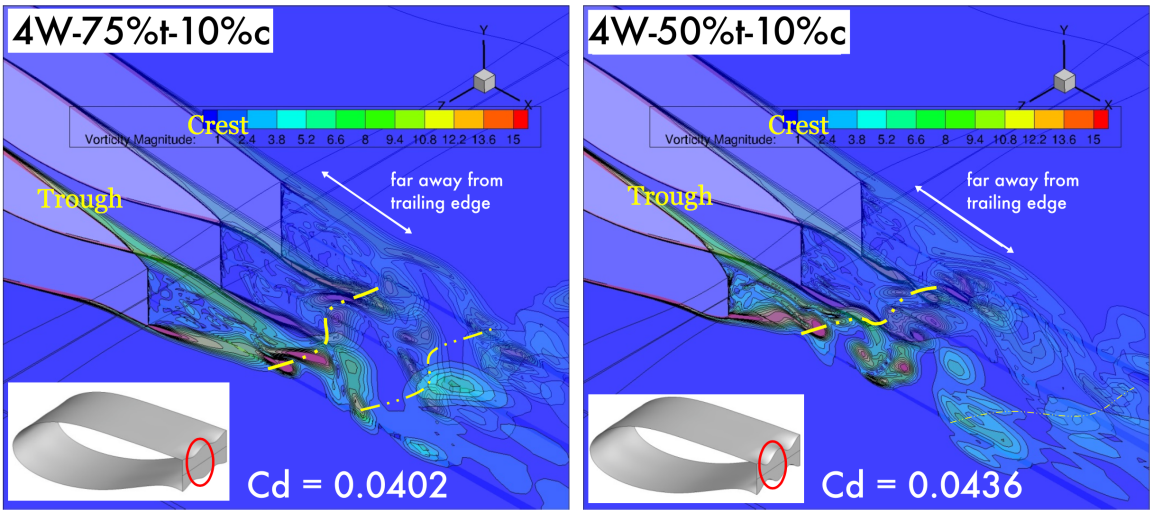

Figure 5.16: Relation between airfoil drag and trailing edge vortex shedding: case of 10%c less portion wavy trailing edge

trailing edge.

5.2.4.6 Relation between flow separation and trailing edge vortex shedding

The results in the previous sections imply; 1) flow separation and 2) trailing edge vortex shedding are two key parameters to determine the aerodynamic performance of the wavy trailing edge modified flatback airfoils. In the current section, the relation between the flow separation and trailing edge vortex shedding is discussed. Base on the results, the trailing edge vortex shedding of the wavy trailing edge can be sorted with three kinds, depending on the size and unsteadiness of flow separation. Three kinds of the trailing edge separations are described in Figure 5.18.

(a) The first type is no separation. In this type, more stream-wise velocity is

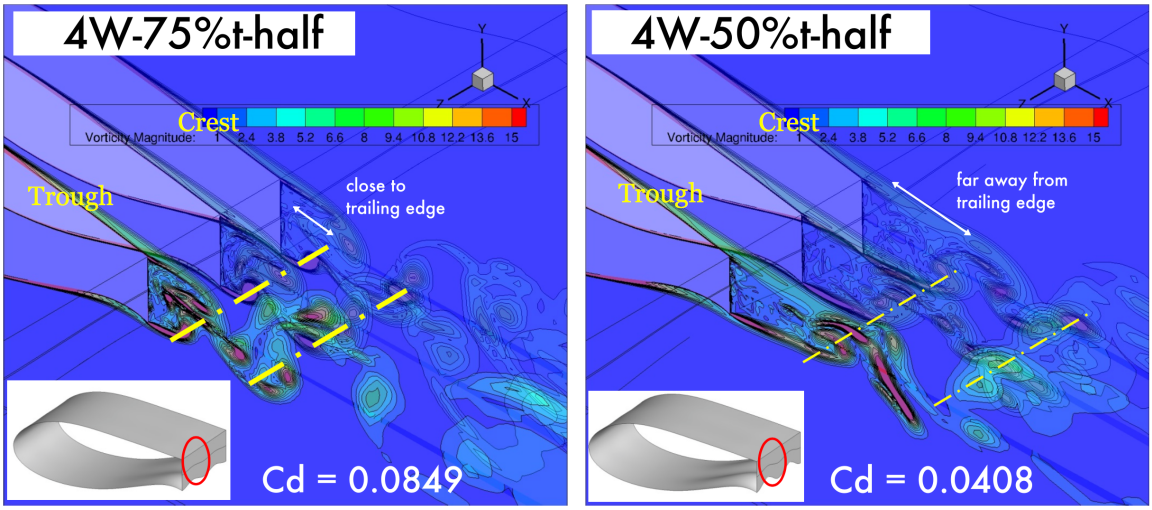

Figure 5.17: Relation between airfoil drag and trailing edge vortex shedding: case of halfway cut less portion wavy trailing edge

induced by the wavy trailing edge, but the Karman-like vortex shedding is still formed at the trailing edge, because the disturbance flow from the wavy geometry is not enough to mix the airfoil base region. There is no separation on the airfoil. Thus, only a small lift loss occurs, but also a small drag reduction occurs. Trailing edge vortex strength is much weaker than the flatback airfoil, but the Karman-like vortex structure still may cause the tonal noise.

(b) The second type is weak separation. In this type, the trailing edge vortex is no longer span-wise coherent and the vortex strength is weak. A small amount of flow separation is evenly placed at each wave paves, and the flow recirculation is observed inside of the separation bubbles. The flow recirculation at the wave paves stirs the flow behind the trailing edge, and eventually breaks up (or eliminates) the span-wise coherency of the trailing edge vortex. The small

flow separation decreases only a small amount of the lift, but the drag reduces a lot, because of the deformation of the trailing edge vortex. Finally it turns out all the best drag and noise reduction designs in the current study belong to this type of separation. Thus, one can conclude this is the most desired case.

(c) Lastly, the third type is massive separation. In this case, the flow separation is massive and irregular. Because of the massive separation, the trailing edge vortex strength is increased comparing to the weak separation cases. However, the vortex structure is no longer span-wise coherent, and the noise may be reduced a lot because of it. In the meanwhile, the massive separation decreases the aerodynamic performance a lot. Thus, it is less desired than the other two types of the flow separation.

In Figure 5.19 through 5.22, surface stream lines and related iso-vorticity contours of the trailing edge vortex shedding are presented.

Time averaged local pressure and skin friction distributions on the airfoil surfaces are plotted in Figure 5.23 and 5.24. The plots on the top of the figures are measured at the wave crest, and the plots on the bottom of the figures are measured at the wave pave. The results of the flatback, the sharp trailing edge and the wavy trailing edge airfoils are plotted in black solid line, red dashed line, and blue dashed lines, respectively. In the figure, trailing edge separation gets vigorous as the wave depth gets deeper. The 4W-50%t wavy trailing edge causes moderate separation near the trailing edge, but the flow separation is much larger with the 4W-25%t

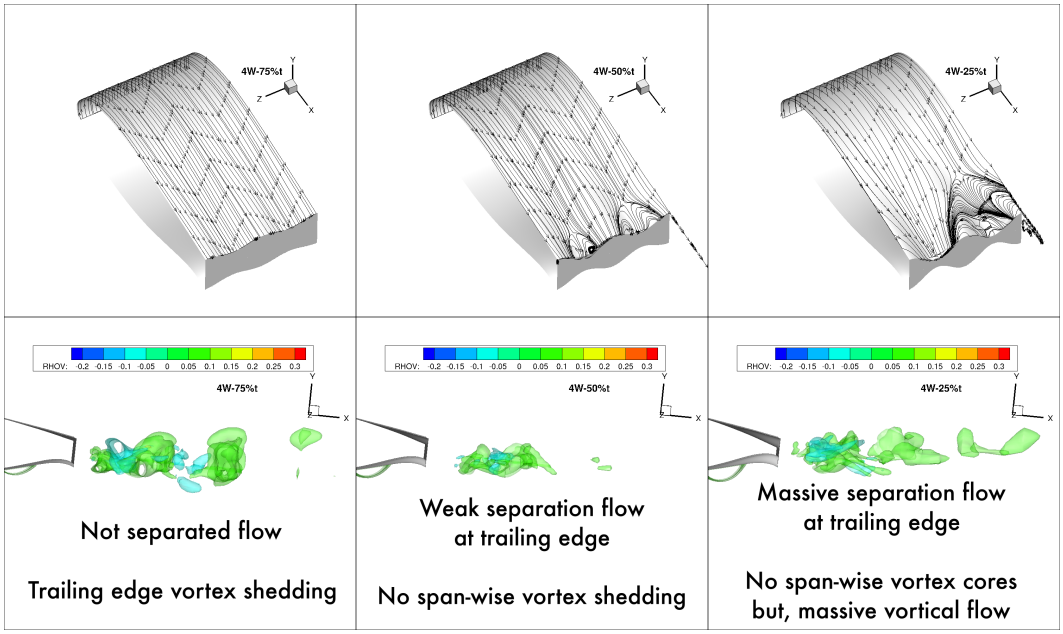

Figure 5.18: Relation between trailing edge flow separation and vortex structure

wavy trailing edge, compared to the sharp trailing edge airfoil.

These are good evidences of the results discussed in the previous two sub-sections. Interestingly, the less portioned wavy, 4W-75%t-10%c causes the flow separation at the only small portion of the airfoil, but decreases the drag same as the 4W-50%t airfoil.

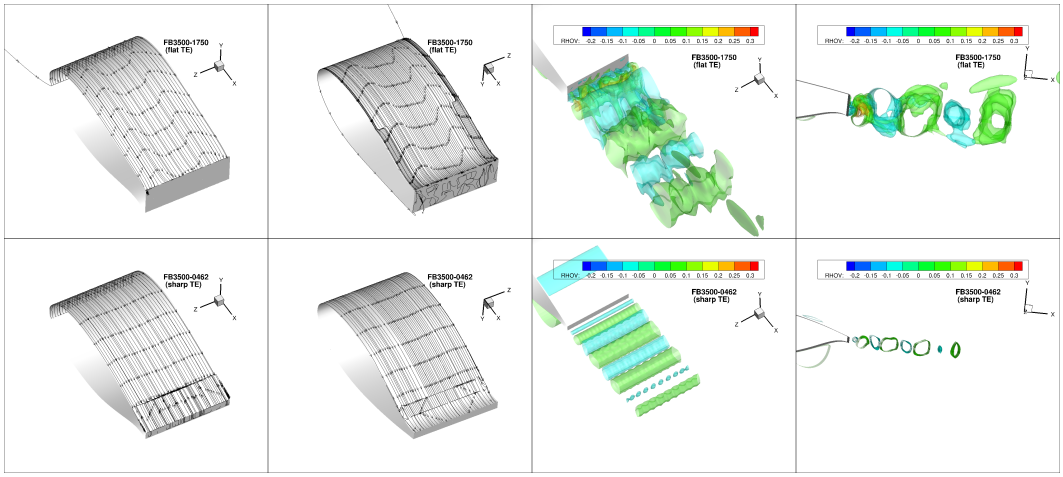

Figure 5.19: Surface stream line and trailing egde vortex structure contours of baseline cases

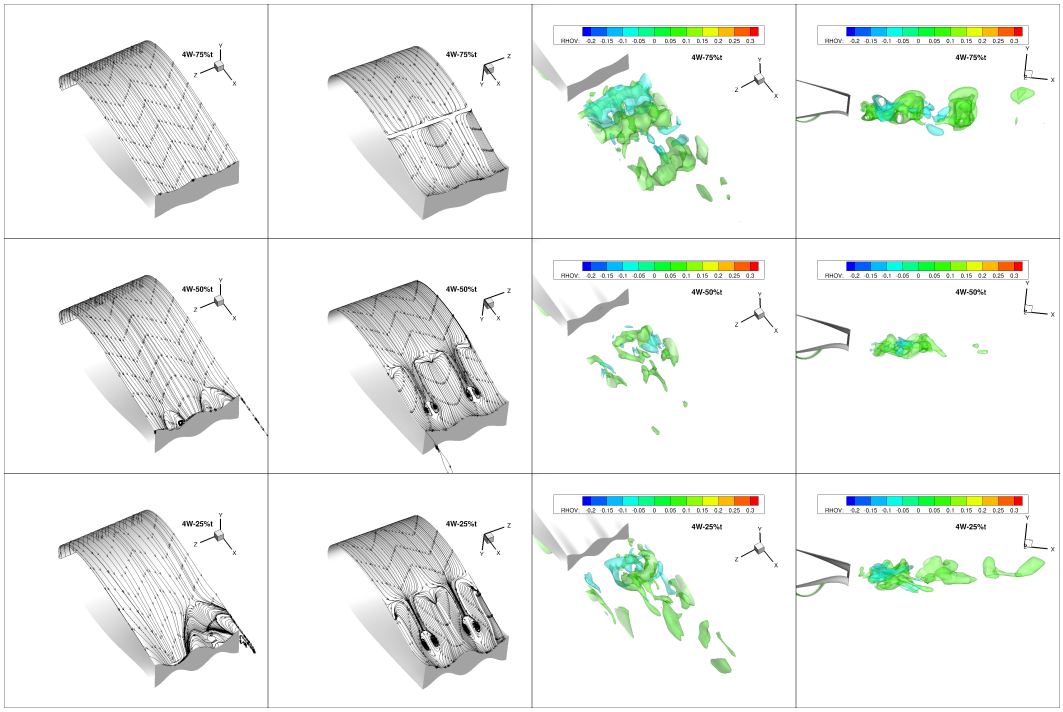

Figure 5.20: Surface stream line and trailing egde vortex structure contours of maximum portion of wavy trailing edge, 4 wave/c

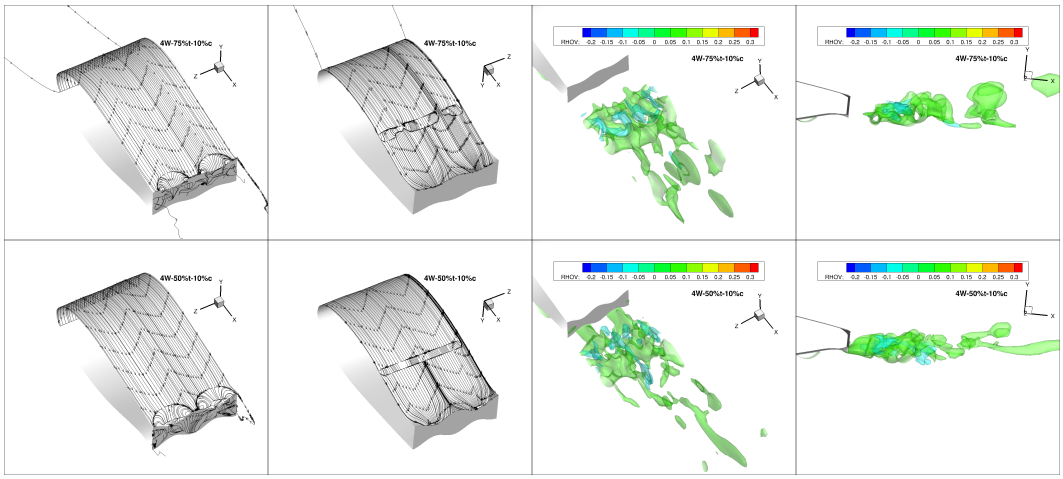

Figure 5.21: Surface stream line and trailing egde vortex structure contours of less portion of wavy trailing edge, '10%c'

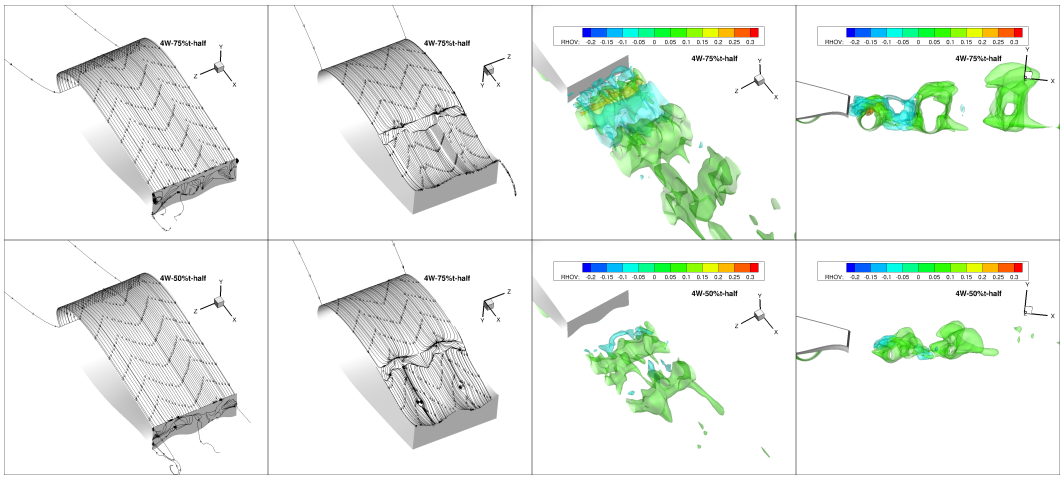

Figure 5.22: Surface stream line and trailing egde vortex structure contours of less portion of wavy trailing edge, 'half'

Table 5.3: Computed lift, drag and pitching moment coefficient of the investigated trailing edge modifications; maximum portion trailing edge wave, at angle of attack 8°

Airfoil	c_l	c_d	c_m
FB3500-0462	1.2759	0.0304	-0.1158
FB3500-1750	1.5232	0.1130	-0.1923
2W-75%t	1.4874	0.0588	-0.1740
2W-50%t	1.4132	0.0385	-0.1576
2W-25%T	1.3236	0.0339	-0.1353
4W-75%t	1.4999	0.0576	-0.1752
4W-50%t	1.6405	0.0355	-0.1537
4W-25%t	1.2146	0.0449	-0.1202
8W-75%t	1.5235	0.0827	-0.1856
8W-50%t	1.4241	0.0498	-0.1654
8W-25%t	1.0678	0.0590	-0.1054
12W-75%t	1.5210	0.0888	-0.1893
12W-50%t	1.2562	0.0544	-0.1415
12W-25%t	1.0712	0.0663	-0.1181

Table 5.4: Computed lift, drag and pitching moment coefficient of the investigated trailing edge modifications; less portion trailing edge wave, at angle of attack 8°

Airfoil	c_l	c_d	c_m
4W-75%t-10%c	1.4085	0.0402	-0.1574
4W-50%t-10%c	1.2377	0.0436	-0.1154
4W-75%t-half	1.4570	0.0849	-0.1771
4W-50%t-half	1.3234	0.0408	-0.1511

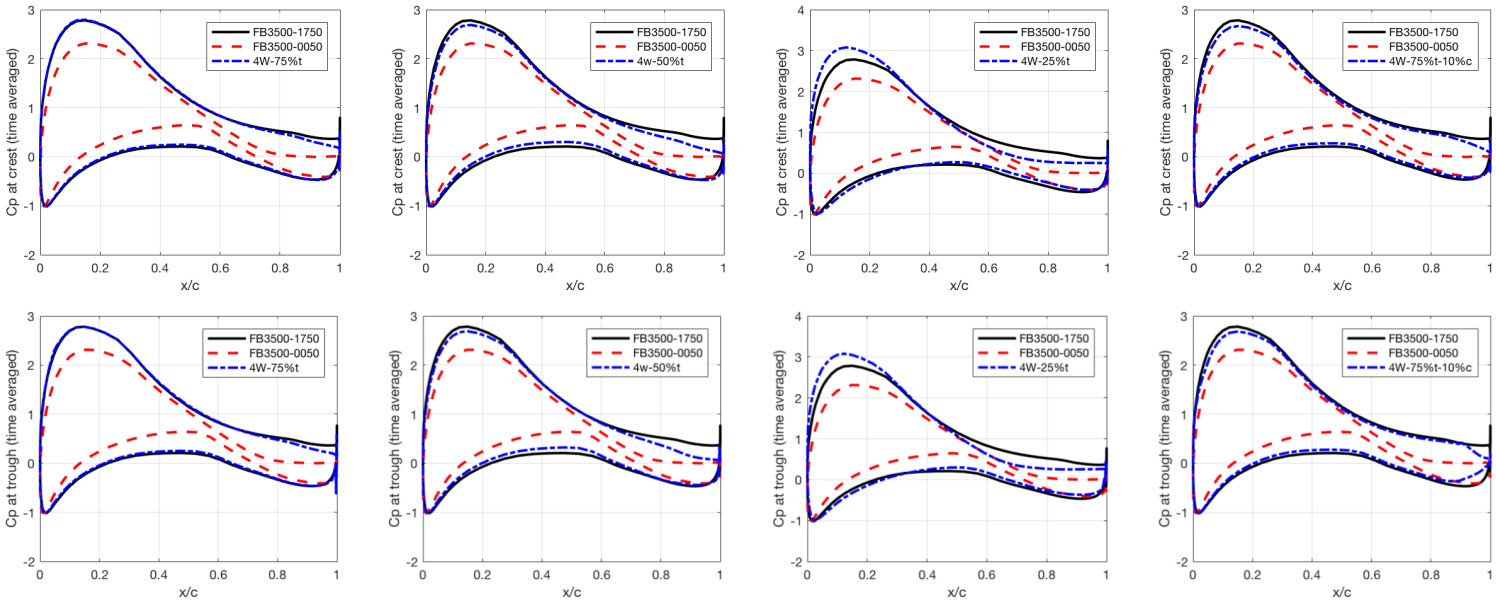

Figure 5.23: Local time-averaged static pressure distribution of various wavy trailing edge airfoils, measured at the maximum(wave crest) and the minimum(wave trough) trailing edge thickness locations. At angle of attack 8°

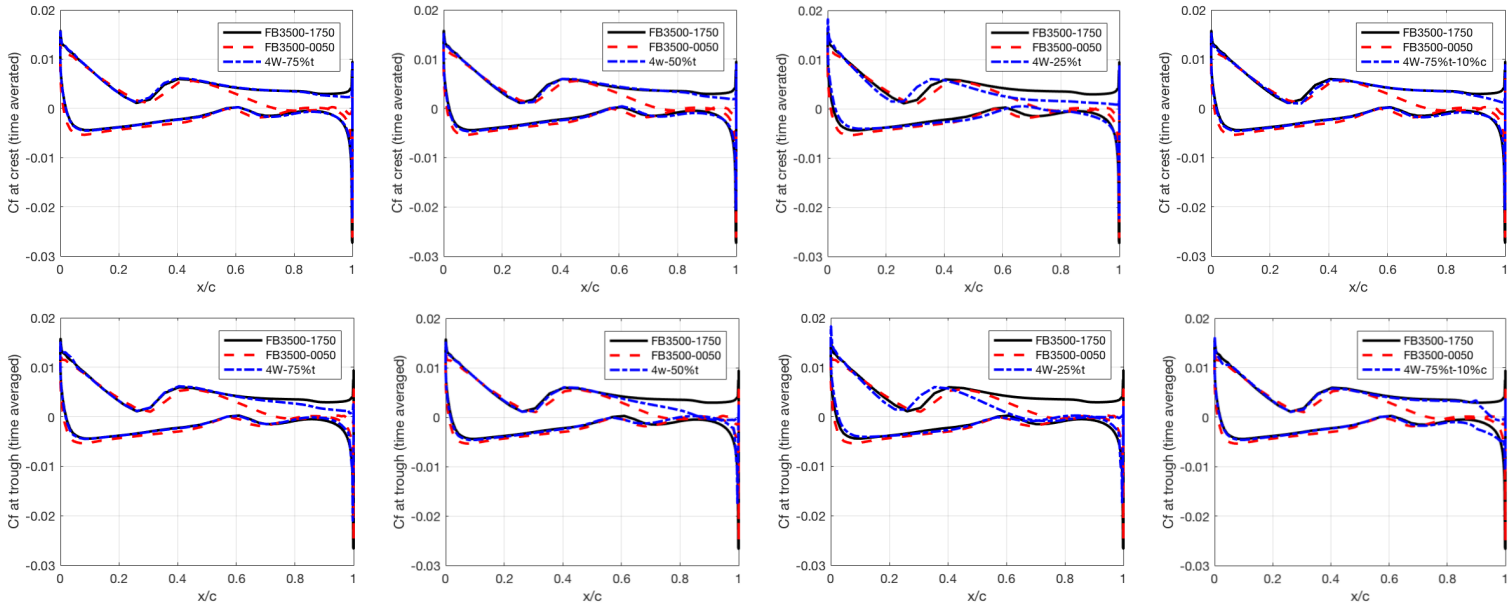

Figure 5.24: Local distribution of time-averaged skin friction of various wavy trailing edge airfoils, measured at the maximum(wave crest) and the minimum(wave trough) trailing edge thickness locations. At angle of attack 8°

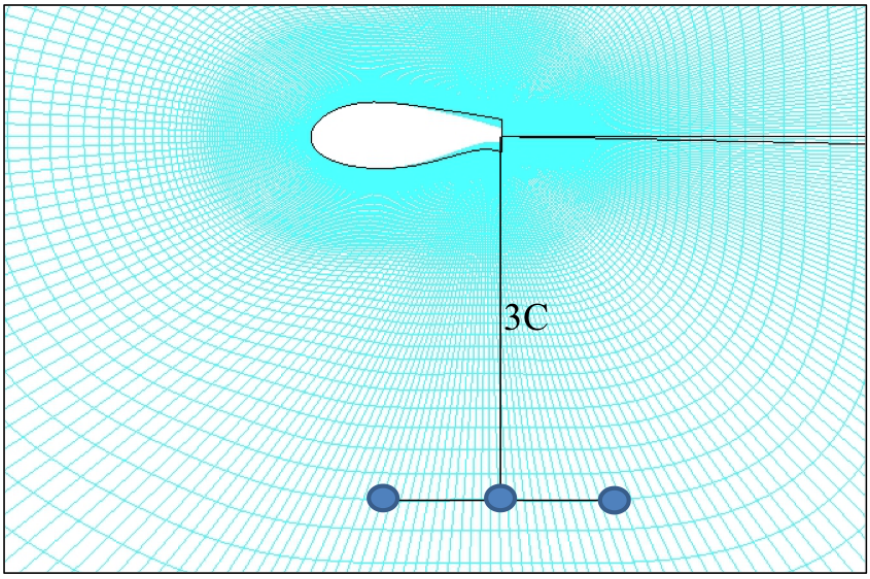

Figure 5.25: Locations of acoustic pressure measurement for the parametric study

5.2.5 Aero-acoustic Characteristics of Span-wise Wavy Trailing Edge

For the acoustic analysis, an unsteady pressure fluctuation is measured at the 3c away from the airfoil as shown in Figure 5.25. Time history of the local pressure is measured for 10 seconds of a period with a sampling rate, 0.001 sec^{-1}. Inflow conditions are the same as the previous section.

5.2.5.1 Comparison of acoustic noise between flatback and span-wise wavy trailing edge airfoil

Instantaneous acoustic pressure propagation is presented in Figure 5.26. It is obvious the wave propagation of the flatback airfoil is much stronger than the wavy trailing edge. In both cases, the strongest waves are originated from the trailing edge.

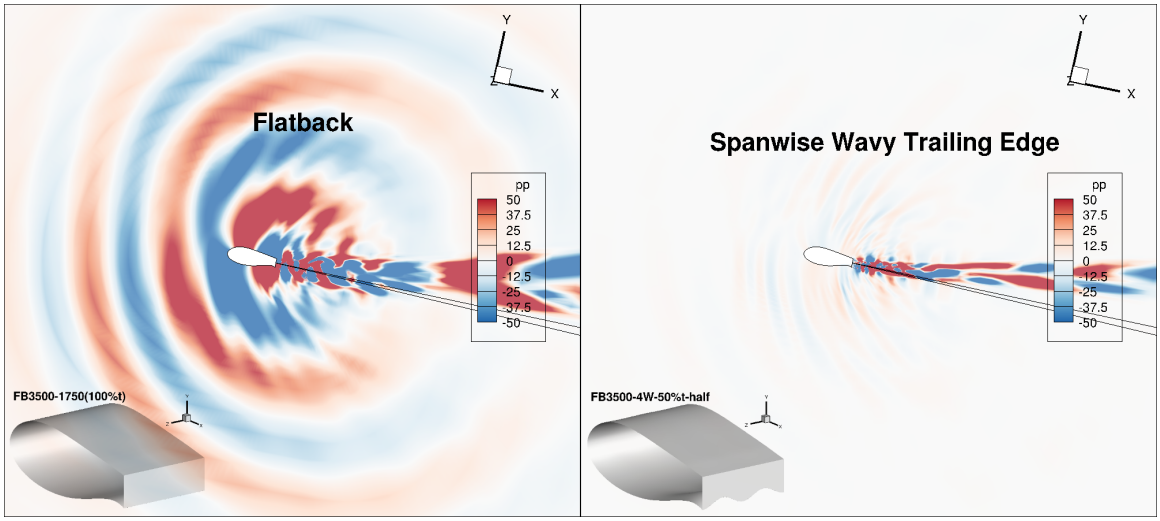

Figure 5.26: Comparison of instantaneous acoustic pressure propagation: flatback and span-wise wavy trailing edge

However, in the case of flatback airfoil, much stronger fluctuation comes out of the noise source. Therefore, the strong waves propagates to the further surround from the origin. However, the noise source of the wavy trailing edge is not strong enough to propagate toward the flow upstream, and the visible fluctuations propagates along the airfoil wake.

The magnitude differences of the pressure fluctuation between the flatback airfoil and the wavy trailing edge airfoils are presented in Figure 5.27. The magnitude of fluctuation of the wavy trailing edge airfoil is reduced approximately 12 times compared to the flatback airfoil. If converts to the decibel, it is approximately 17.4dB of the amplitude reduction.

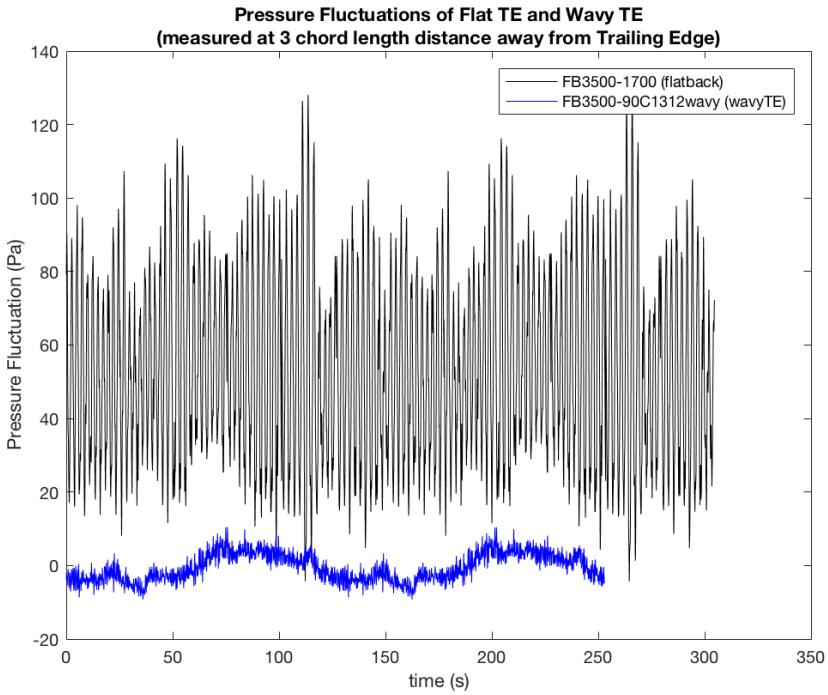

Figure 5.27: Comparison of acoustic pressure fluctuation in time history between flatback and wavy trailing edge

5.2.5.2 Acoustic noise and trailing edge vortex structure

The FFT (Fast Fourier Transform) results of the measured pressure data and related the trailing edge vortex structures are presented in Figure 5.28. The FFT results show clear tonal noise in the flatback airfoil case, but no longer with the 4W-50%t wavy trailing edge cases and many of the other wavy trailing edge airfoils. For some cases of the wavy trailing edge airfoil, such as the 4W-75%t-half, the noise spectrum is not so much different with the flatback airfoils.

Figure 5.28 compares the acoustic noise spectrum and the trailing edge vortex structures, and it shows the key features are coincidence each other. In the iso-vorticity contours, the vortex structure of the 4W-75%t-half is much bigger and span-wise coherent, comparing with the other wavy trailing edge airfoils. It is noted that the trailing edge vortex structure of the wave depth 75%t wavy is still span-wise coherent, and contrarily the vortex structure of the wave depth 50%t is no longer span-wise coherent. Very weak strength of the vortex shedding does not cause the tonal sound. The vortex of the 4W-50%t-10%c is much stream-wise compared to the 4W-75%t-10%c, but noise spectrum is not so much different.

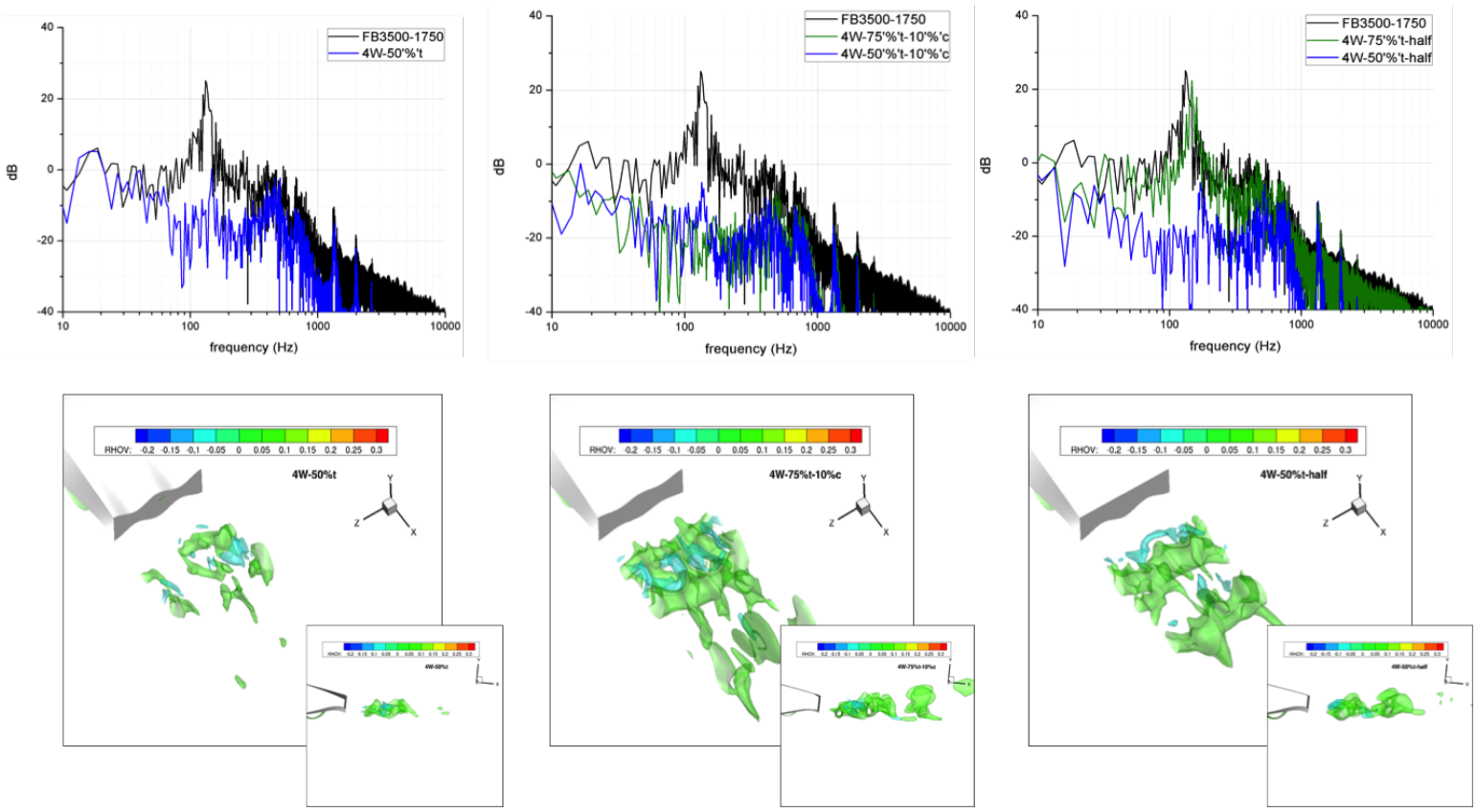

Figure 5.28: Comparison of FFT analysis result between flatback and wavy trailing edge: tonal noise peak is reduced with properly designed wavy trailing edge by breaking up strong vortical structure at trailing edge

5.2.5.3 Acoustic noise characteristics of span-wise wavy trailing edge

In the given angle of attack, 12°, flow separation occurs on the surface of the sharp trailing edge airfoil, while flow of the flatback airfoil is attached. Based on the results presented in Figure 5.29, at least 8.75% t_{te}/c of trailing edge augmentation is required to prevention the trailing edge flow separation successfully, at the given angle of attack. In the figure, as one expects, the strong standing recirculation flow is observed in the no flow separation cases. An interesting result here is that the trailing edge vortex shedding patterns are shown in the flow separation cases, too. With $t_{te}/c = 4.62\%$, the formation of the recirculation is not regular, but it causes weak vortex shedding in the wake. With $t_{te}/c = 0.5\%$, strength of the recirculation is stronger, thus the vortex shedding in the wake is also stronger.

Figure 5.30 presents the acoustic characteristics of the baseline airfoils, FB3500-1750 and FB3500-0050, measured at AoA 12 °. Focusing on the results of the FB3500-1750, magnitudes of unsteady pressure fluctuations (left figures) of the FB3500-1750 are much lager than the FB3500-0050. This strong pressure oscillations are mainly caused by the periodic trailing edge vortex shedding. In the FFT results (center and right figures), two clear noise peaks are observed. The loudest tone about 120dB (SPL) is appeared at 125Hz, and the second loudest tone about 103dB (SPL) is appeared at 400Hz. The tonal noise in 125Hz seems to be caused by oscillation of the standing vortical flow existing at trailing edge. The tone in 400Hz seems to be caused by the Karman-like vortex shedding in the wake, respectively.

In the results of the FB3500-0050, magnitudes of the fluctuations are lower

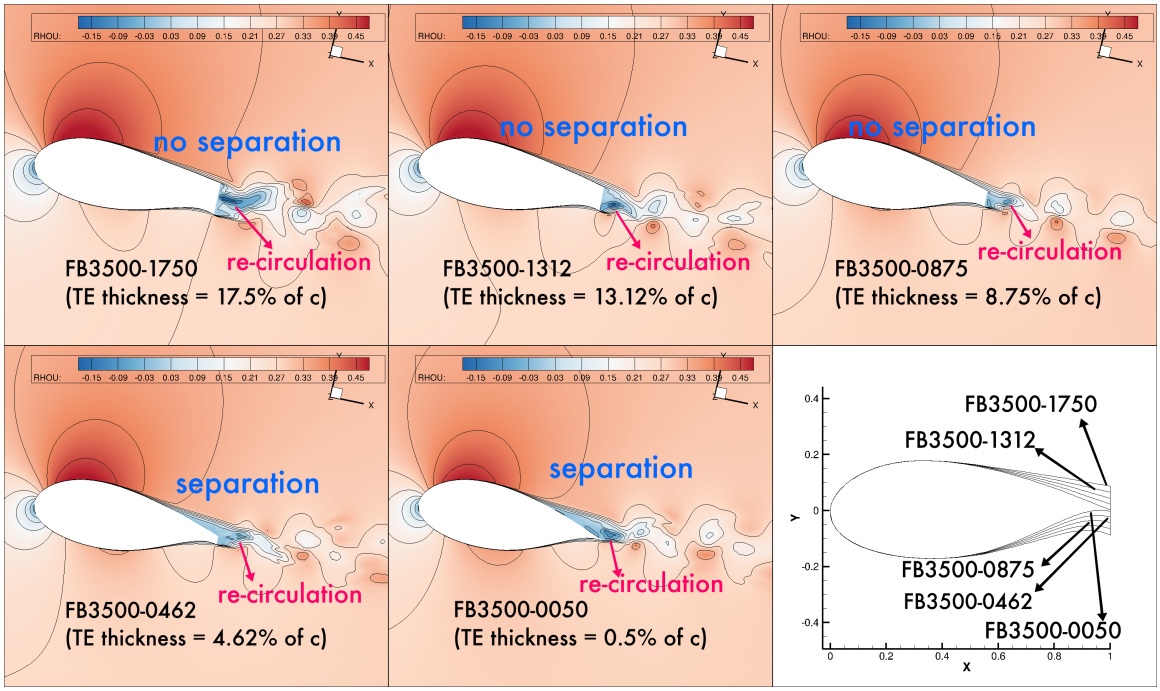

Figure 5.29: Flow separation and trailing edge recirculation of various trailing edge thickness at AoA 12°

than the flatback airfoil. As we checked in Figure 5.29, even the sharp trailing edge airfoil in separation may cause the Karman-like vortex shedding. Regarding it, we can explain the two noise peaks observed in the acoustic signal of sharp trailing edge. The loudest noise is now 107dB (SPL) at 200Hz, and the second loudest noise is 97dB (SPL) at 650Hz. Comparing to the flatback, oscillation of the standing flow is faster, but weaker, thus the vortex shedding frequency is much faster, but weaker.

Recalling the aerodynamic results of the previous subsection 5.4.4.4 and 5.2.4.6, the less portion wavy trailing edge modifications are more efficient to remove (or relocate) the standing trailing edge vortex, compared to the maximum portion wavy modifications. In Figure 5.31 through 5.34, the acoustic characteristics of the less

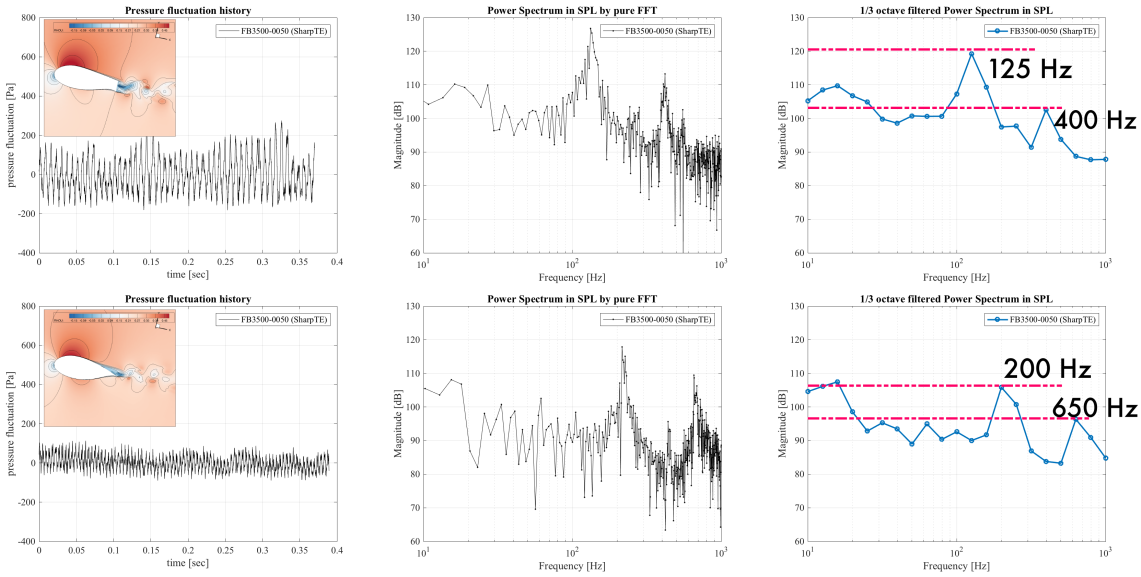

Figure 5.30: Acoustic characteristics of baseline airfoils at AoA 12°

portion wavy trailing edges are presented. In the figures, an oil flow surface streamline (top-left), ρU momentum measured at the left trough of the wave (top-second left), at the center crest (top-second right), at the right trough (top-right), pressure fluctuation time history (bottom-left), Sound Pressure Level (SPL) in frequency domain (bottom-center) and the 1/3 octave band filtered SPL in frequency domain (bottom-right) are presented respectively.

First of all, the acoustic noise of the 4W-75%t-10%c airfoil is much quieter than the flatback airfoil. And even compared to the sharp trailing edge airfoil, the wavy trailing edge airfoil is much quieter, at the given angle of attack (0-20°). There are two tonal noise peaks are still observed, but their magnitudes are much reduced and the frequency ranges are shifted to a little higher. The lower frequency tonal peak is now shifted to 160Hz, and the magnitude is reduced to 95dB, which is 25dB

less than the flatback trailing edge. Similarly, the higher frequency tonal peak is shifted to 500Hz, and the noise level is reduced to 90dB, which is 13dB less than the flatback airfoil.

The results of the second airfoil, 4W-50%t-10%c look a little different. The loudest tonal peak (95dB) is still exist at the shifted frequency (140Hz), but broad band noise is observed at the lower frequency ranges instead of the high frequency tonal peak. Comparing to the 4W-75%t-10%c airfoil, distribution of the standing flow at the trailing edge is more uneven, and the irregular formation of the standing flow helps to decay the periodicity of the span-wise vortex shedding. It is reasonable to believe that these mainly cause the low frequency broad band noise and eliminate the high frequency tonal noise.

The third airfoil, 4W-75%t-half, unfortunately, does not reduce the noise as much as the other wavy modifications do. Although the similar two tonal peaks are appeared at the same frequencies with the 4W-75%t-10%c airfoil, their magnitudes are not so different with the flatback airfoil (only 6dB/3dB reduction for the low/high frequency). Recalling the aerodynamic performance of the trailing edge modification, it is not surprise. Strong standing flow is observed close to the trailing edge, and clear vortex shedding exists.

However, deeper wave modification helps to reduce noise. Tonal noise peaks of the 4W-50%t-half are measured as around 97dB. Noise characteristic and the trailing edge flows are quite similar to the 4W-75%-10%c airfoil.

Thus, based on the acoustic results presented above, the span-wise wavy trailing edge modification reduces low frequency (about 125Hz) tonal noise by 25dB,

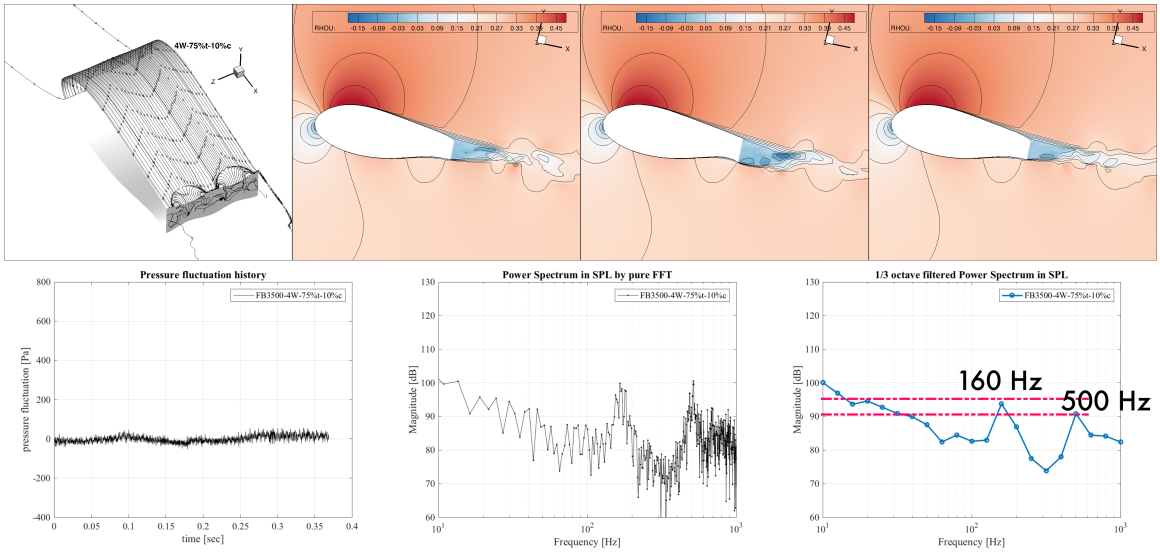

Figure 5.31: Acoustic characteristics of 4W-75%t-10%c at AoA 12°

and high frequency (400Hz) by 13 - 23dB if it properly designed.

5.3 Remarks of Parametric Study

5.3.1 Proper Sizing of Span-wise Wavy Trailing Edge

(a) Regarding the aerodynamic performance

Revisiting the results in the previous sections, appropriate wave depth is between 75%t or 50%t. And appropriate wave length is between 4W or 2W, respectively. Revisiting the lift and drag map in Figure 5.12, the wavy trailing edge modified airfoils in the blue circle are considered as a proper wavy trailing edge design. Those modification designs decrease the lift less than 7% of the original airfoil, and reduce the drag more than 50%. As we sort these airfoils with sub groups, the airfoils on top-right in the circle provide more

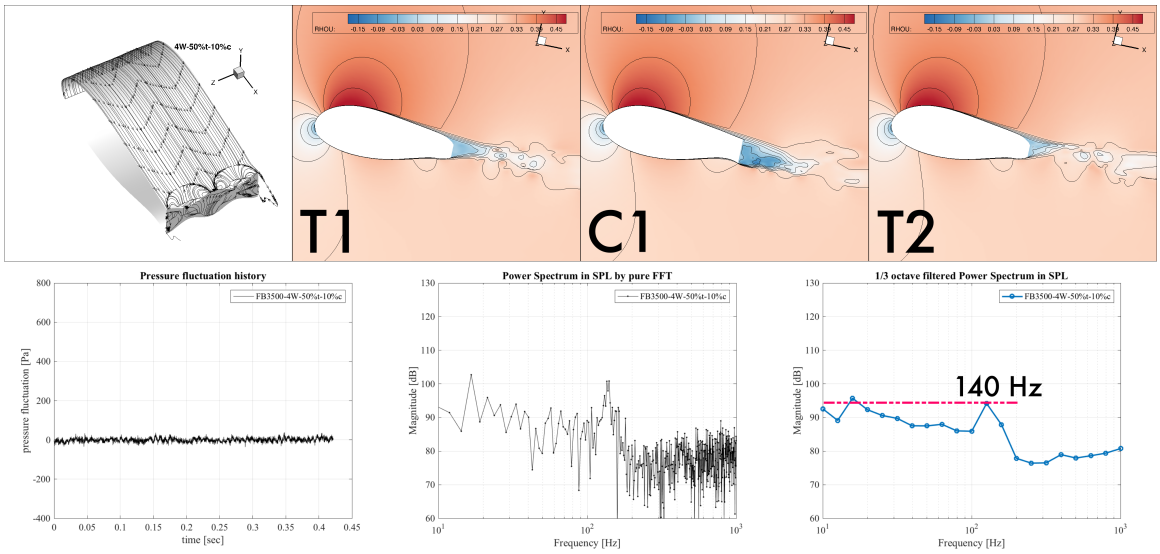

Figure 5.32: Acoustic characteristics of 4W-50%t-10%c at AoA 12°

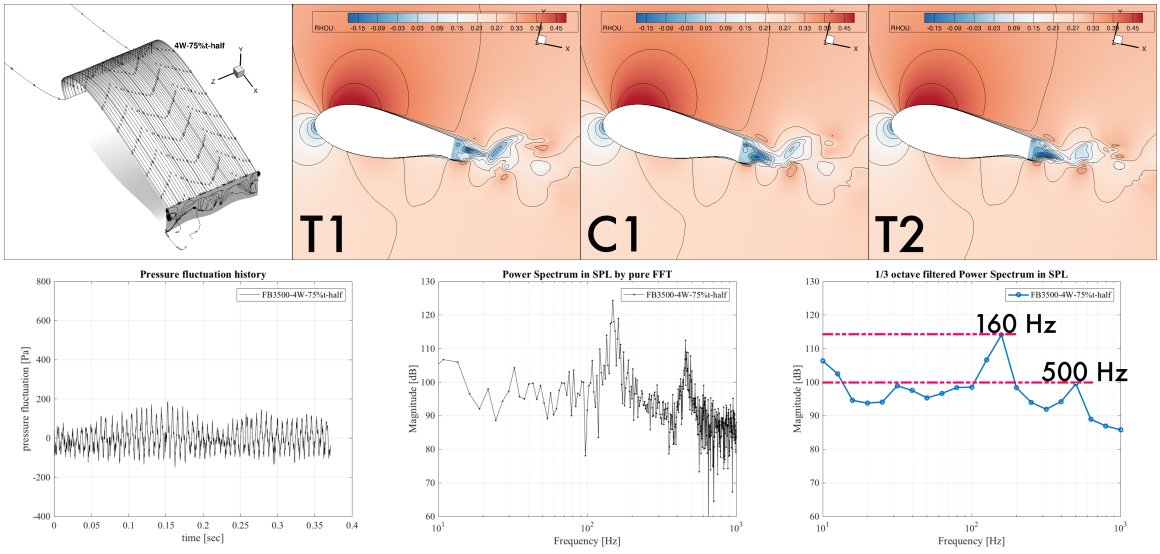

Figure 5.33: Acoustic characteristics of 4W-75%t-half at AoA 12°

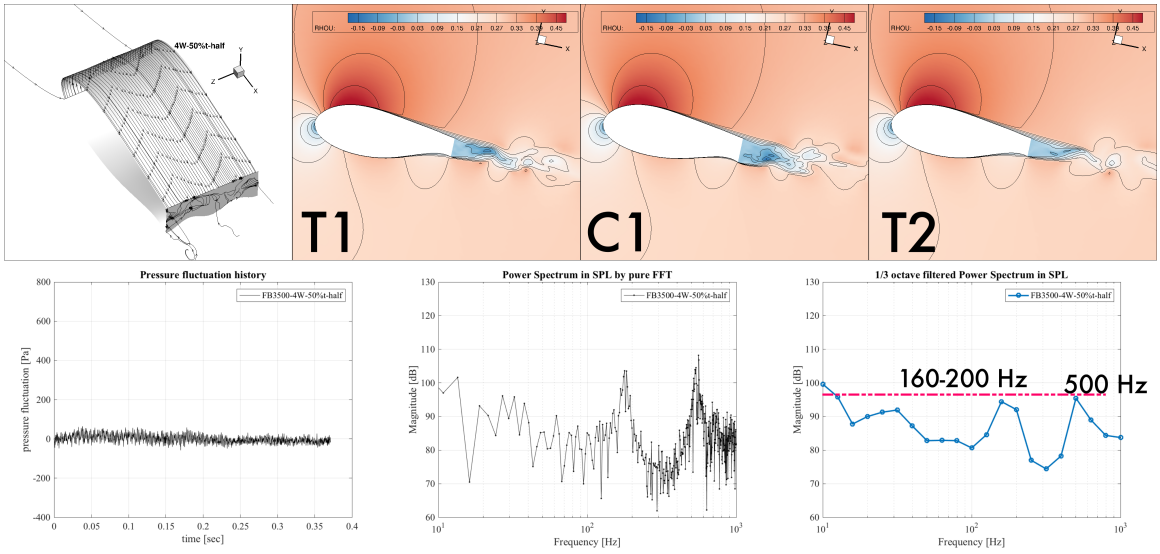

Figure 5.34: Acoustic characteristics of 4W-50%t-half at AoA 12°

aerodynamic benefit, and the group on the bottom-left provides more acoustic benefit.

In Figure 5.35, the aerodynamic performance of the tested wavy trailing edge airfoils is presented as the lift to drag ratios. Although all the wavy trailing edge airfoils shows better lift to drag ratios over the range of angles of attack, their maximum performance ranges are different, depending on the modification designs. While the maximum portion of wavy trailing edge airfoils are the best aerodynamic performance designs at the moderate angles of attack (between 4° and 12°), the less portion wavy trailing edges show the best performance with broader ranges of the angles of attack.

Considering the blade pitch and the twist in real wind turbine applications, the less portion of wavy modifications might be a better selection, due to their

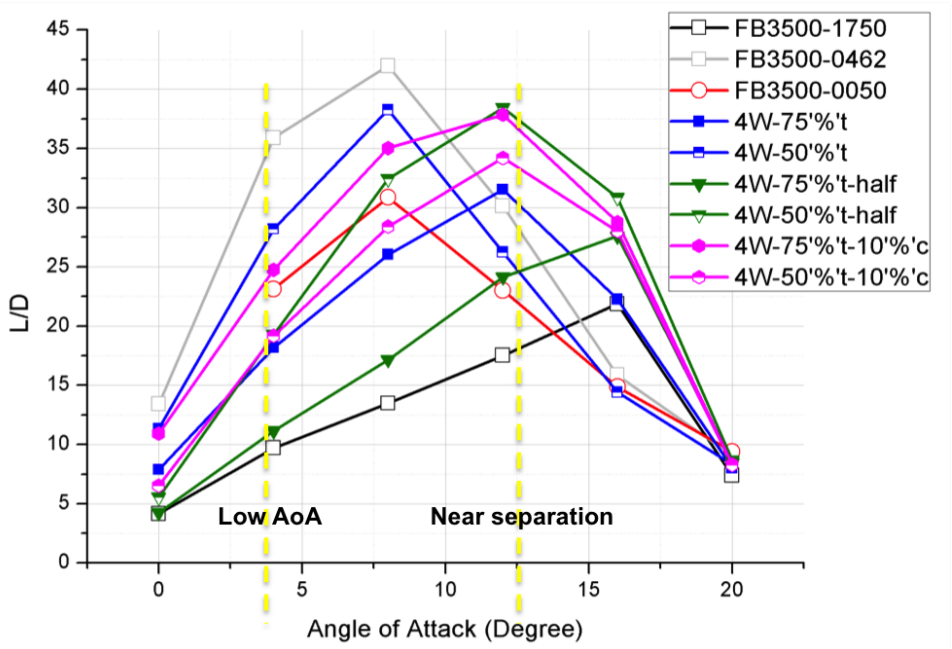

Figure 5.35: Lift to drag ratio envelopes over ranges of angle of attack 0 deg - 20 deg

generous tolerance for the flow conditions. Furthermore, the less portion of wavy modifications are more effective to generate the local moderate separation only at the trailing edge rather than other airfoil regions, as shown in Figure 5.36.

(b) Regarding the aero-acoustic performance

To discuss the best acoustic design, time history of pressure fluctuations and acoustic noise spectrum of various wavy modifications are investigated. In Figure 5.37, pressure fluctuation of properly designed wavy trailing edges have much lower magnitudes. Similarly, tonal noise level of the well designed wavy trailing edges are much lower than the flatback or ill-designed wavy trailing

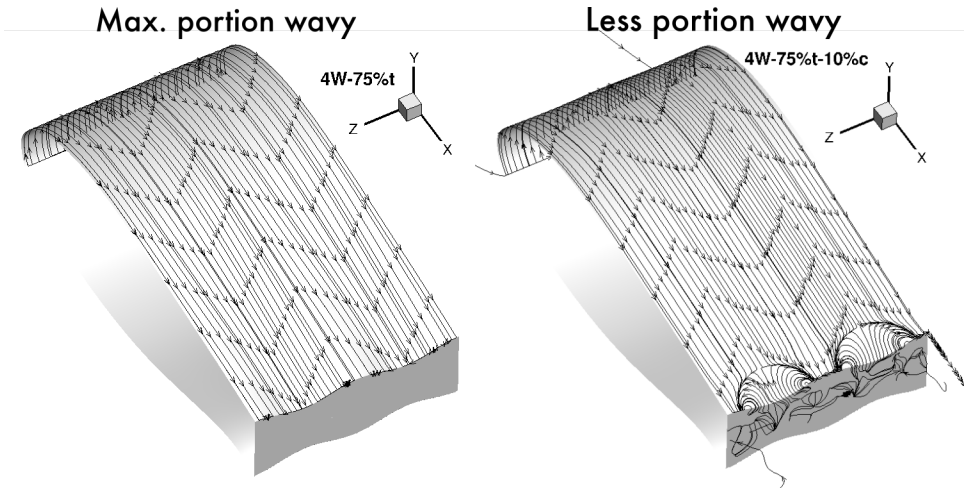

Figure 5.36: Effectiveness of the less portion wavy trailing edge design

edges, as shown in Figure 5.38. Here, reasonable tonal noise peak criteria of good acoustic designs might be around 100dB or less, since the most of best acoustic designs of noise reduction add-ons reduces around 20dB of the tonal peak. In the given case, the most of less portion wavy modifications are within the criteria except the 4W-75%t-half airfoil. However, comparing to the halfway cut modifications, the 10%c modification reduces the high frequency tonal peak much efficiently. In addition, only the 10%c modifications allows the shallow wave modification to get the best aerodynamic and acoustic performance. And the shallow wave modification is Thus, based on the analysis, the 10%c modification is more efficient design in a perception of acoustic performance.

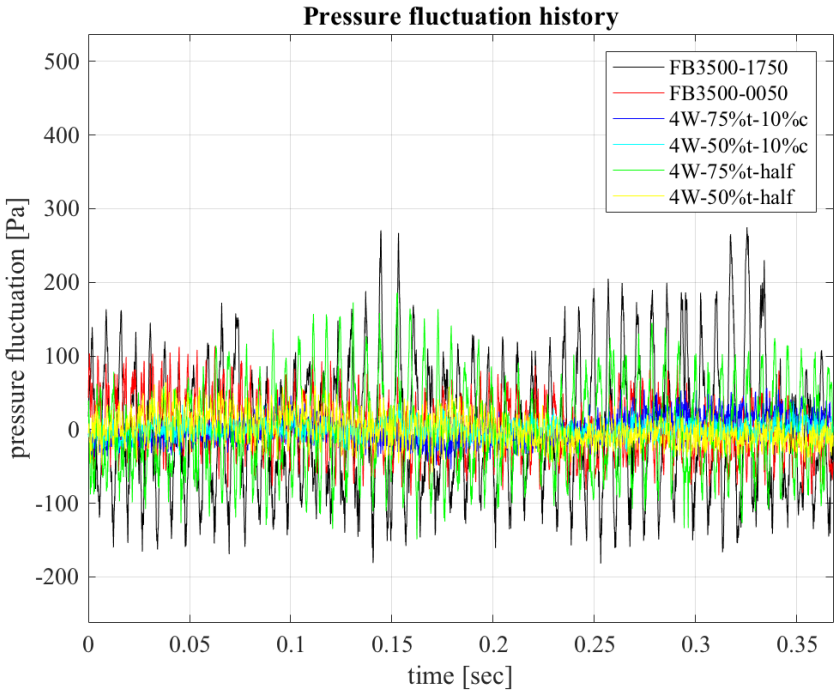

Figure 5.37: Acoustic pressure fluctuation of baseline airfoils and spanwise wavy trailing edge airfoils at AoA 12 degree

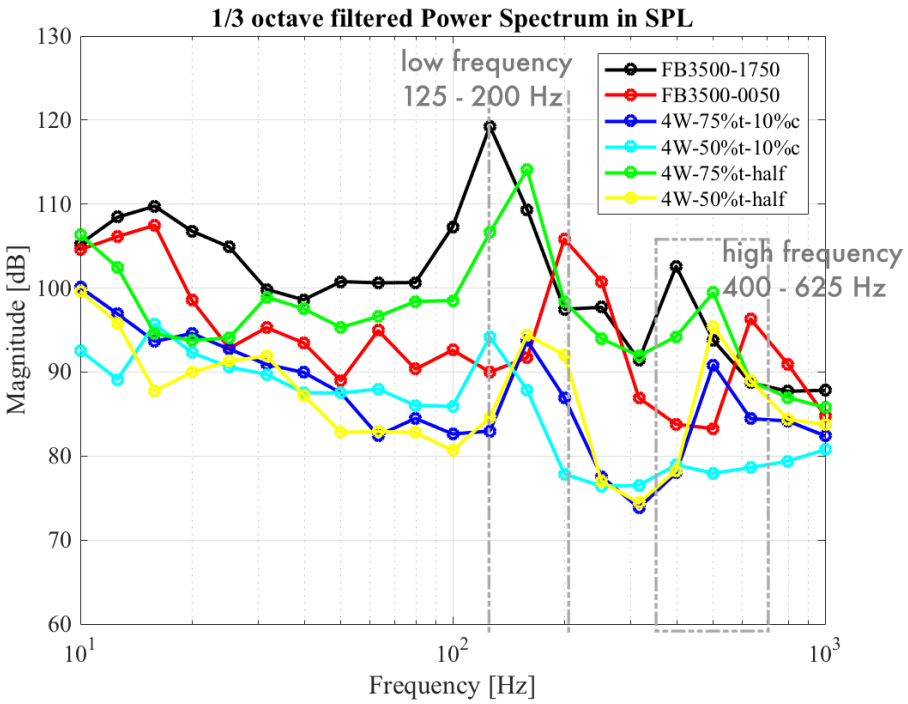

Figure 5.38: 1/3 octave band filtered Sound Pressure Level(SPL) of baseline airfoils and span-wise wavy trailing edge airfoils at AoA 12 degree

5.3.2 Comparison with the Trailing Edge Add-ons

The aerodynamic / aero-acoustic performances of the current parametric study are compared with the conventional add-on type drag reduction devices. For the references, again J.P. Baker and C.P. van Dam's experimental results [27] are used. They conducted wind tunnel tests of several drag and noise reduction add-ons (a split plate, serrated split plate, cavity and the cavity with serration) attached on the trailing edge of the FB3500-1700.

In Figure 5.28 and 5.29, the lift and drag of the splitter plates (both plain and serrated) and cavities (both plain and serrated) are presented and compared with the current wavy trailing edge results. Generally, the splitter plates produce the larger lift and drag than the wavy trailing edge, and the cavities generate the lower lift and larger drag compared to the wavy trailing edge. Considering the drag only, the drag of add-on devices is approximately 0.05 or larger and the drag of the properly designed wavy trailing edge airfoils is less than 0.04.

Figure 5.29 shows the lift to drag ratios of the trailing edge modifications. Comparing to the add-on devices, the wavy trailing edge modification produces the larger lift to drag ratio at the most angles of attack, especially much larger lift to drag ratio at the moderate angles of attack, such as 4 - 8 °. It is due to the larger drag reduction of the wavy trailing edge modification.

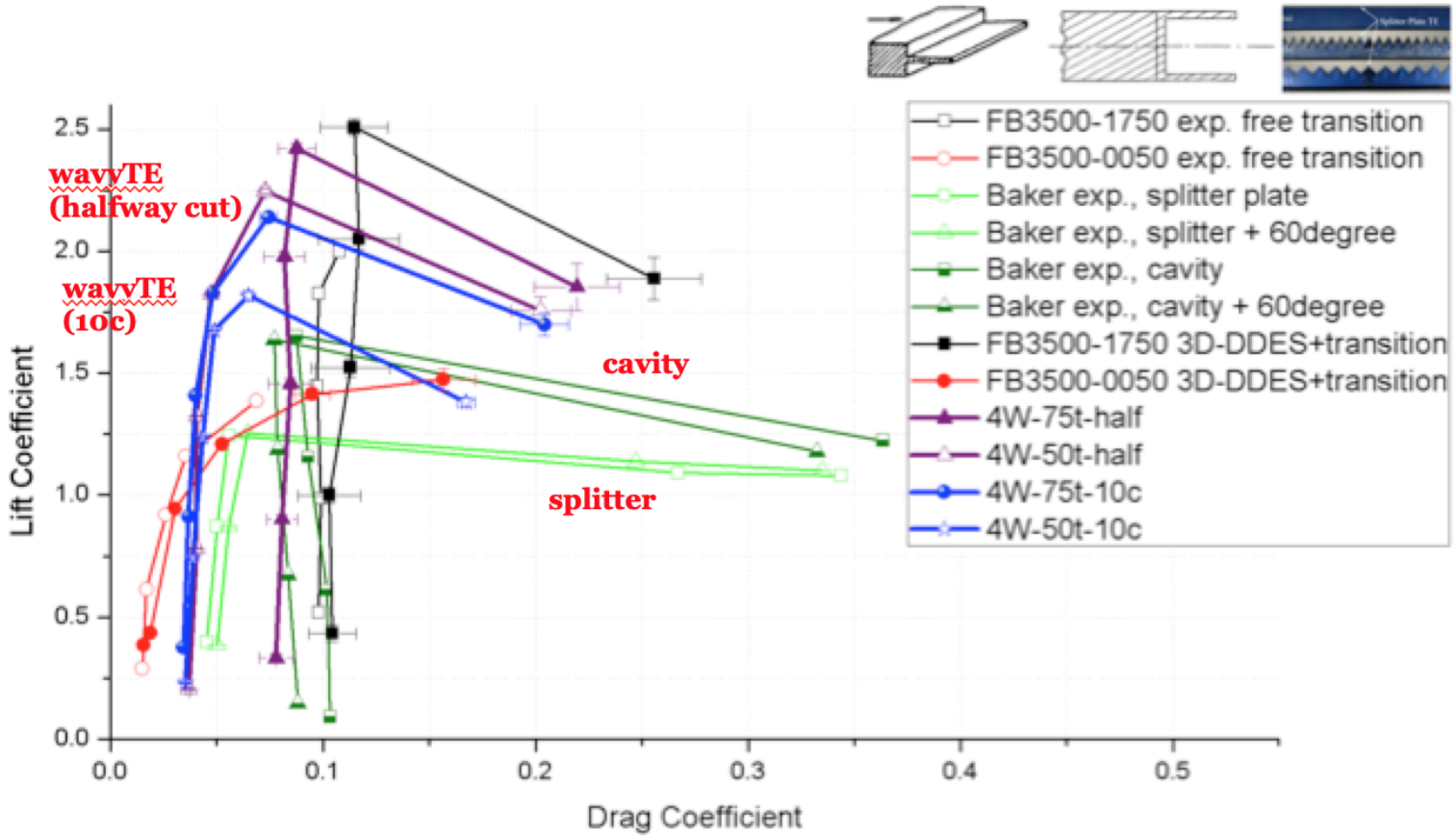

Figure 5.39: Comparison with drag/noise reduction addons: Cl versus Cd

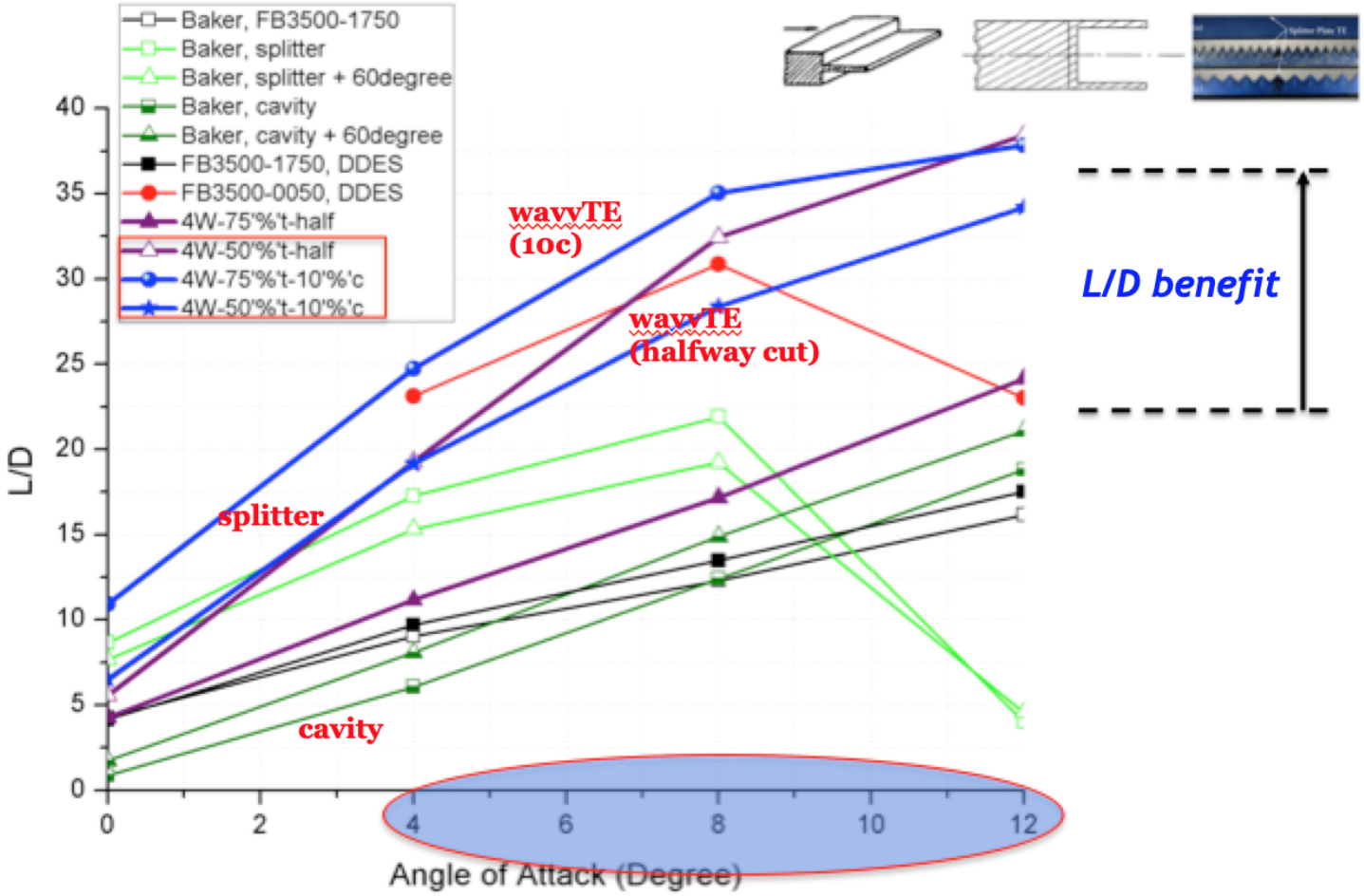

Figure 5.40: Comparison with drag/noise reduction addons: lift to drag ratio

Chapter 6: Span-wise Wavy Trailing Edge Modified Wind Turbine Blade

Aerodynamic and aero-acoustic characteristics of the span-wise wavy trailing edge airfoils have been studied and design criteria of the best performance wavy designs have been found through the Chapter 5. In the current chapter, the best performance wavy trailing edge designs are applied to a modern larger wind turbine blade. The SNL100-03FB(Flatback) wind turbine blade developed by Sandia National Laboratory is used for a base-line blade. The baseline blade and several versions of span-wise wavy modified SNL100-03FB blades are tested, under assumptions of the isolated rotor simulation. Aerodynamic and aero-acoustic performance of the baseline and modified blades are analyzed. The OVERTURNS solver is used for the current isolated rotor simulations.

6.1 The SNL100-03FB wind turbine blade

The SNL100-03FB blade was designed with a 100 meter length, aiming for a future 13.2MW wind turbine, developed by the Sandia National Laboratory. As results, they published a series of the 100 meter length blade designs. It is briefly introduced in the previous chapter 1.1.4. The SNL100-03FB blade is the latest

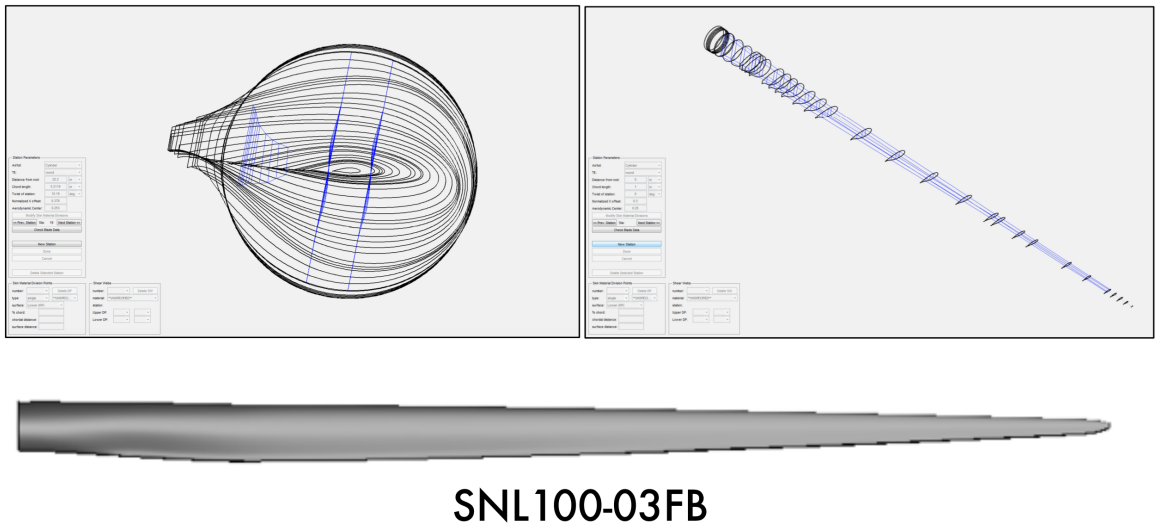

Figure 6.1: SNL100-03FB blade

design in the series. It was designed as a lighter and slender blade compared to the other blades in the series of designs. For the reason, a flatback trailing edge was applied to the inboard region of the blade. A sketch of the SNL100-03FB blade is shown in Figure 6.1, and more details of the blade design are well described in the Sandia report [2].

6.2 Case Study

In the current chapter, the CFD results of the several design modifications of SNL100-03FB blade are introduced. In the CFD, the isolated rotor conditions are assumed. The isolated rotor simulation considers only a rotor itself, and ignores other wind turbine configurations, such as a nacelle, tower and else. Thus, uniform inflow velocity profile is used, instead of Atmospheric Boundary Layer (ABL)

condition.

In the current time (Fall 2018), none of real wind turbine blade larger than 100meter exists or has been built yet. Therefore, there is no experimental data (actually it is usual for the most of wind turbine simulation) exists for the SNL100-03FB blade. Because of, the lack of experimental data, it is not easy to presume how the flow would like to be at the inboard of baseline blade. If bluntness of the trailing edge is high enough to prevent the flow separation, it may require the wavy modification to break up the stationary recirculation flow and periodic vortex shedding. Contrarily, if there is a massive flow separation at the inboard, preceding a trailing edge augmentation may help to increase the aerodynamic performance before applying the wavy modification.

Thus, as case studies,

(a) The original SNL100-03FB blade is tested as a baseline.

(b) Secondly, effect of span-wise trailing edge modification on the baseline blade is tested. The best aerodynamic and aero-acoustic performance span-wise designs, 2W-75%t-10%c and 4W-75%t-10%c are used for the trailing edge modification.

(c) Thirdly, effect of trailing edge augmentation on the baseline blade is studied.

(d) Lastly, effect of combined modification of augmented and span-wise wavy trailing edge (later in the current chapter, it is called as 'Blunt-Wavy Combined trailing edge modification') is explored.

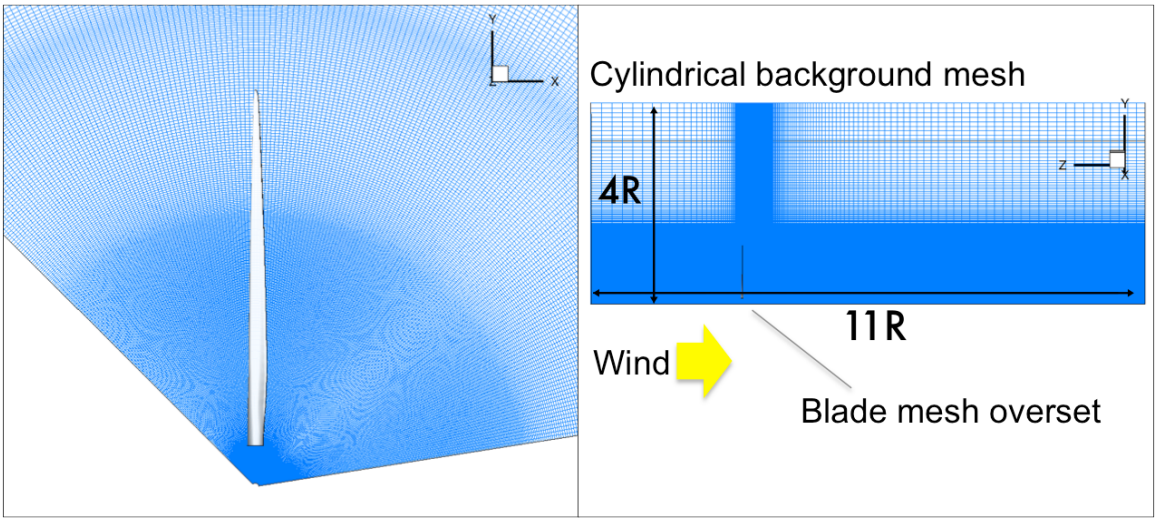

Figure 6.2: Overset meshes of the current study

6.2.1 Mesh Description

An overset mesh system is used for the current study. The mesh system consists of a single blade mesh overset to a cylindrical background mesh as presented in Figure 6.2. The blade mesh is constructed with a structured O-O grid topology, which dimensions of $269 \times 380 \times 85$ in the wrap-around, span-wise, and wall-normal directions, respectively. The cylindrical background mesh is also structured, which dimensions of $184 \times 388 \times 320$ in the azimuthal, radial, and axial direction, respectively.

For the three bladed rotor, considering efficiency of computational cost, 120° of the azimuthal extent is used for the background mesh rather than a whole 360°. The mesh also has an extent of 4 times of rotor blade radius in the radial direction, and 11 times of rotor blade radius in the axial direction. For an isolated rotor

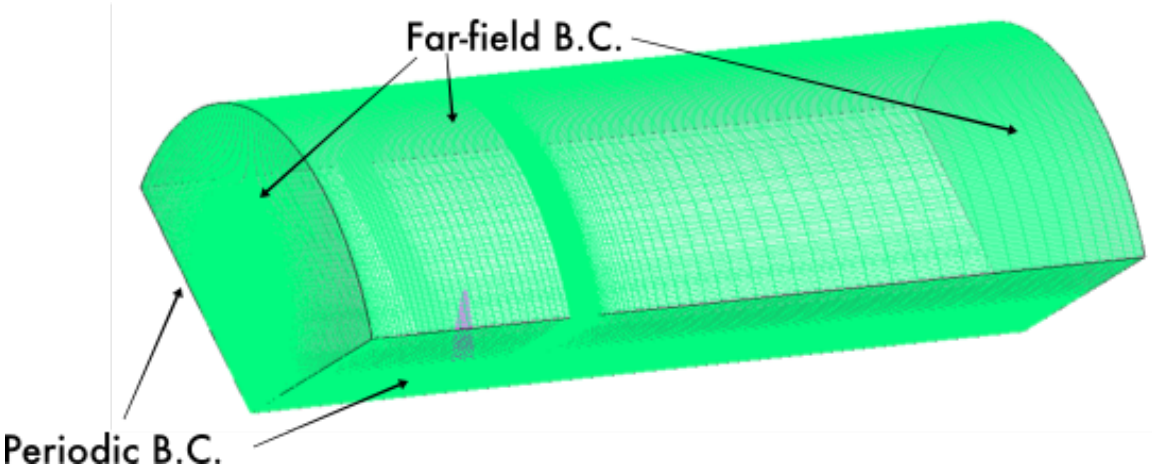

Figure 6.3: Initial and boundary conditions of near body and background meshes

simulation, these mesh extensions are good enough to meet a far-field boundary condition. The finest grid spacing in the blade inboard regions of the background mesh is 0.01 of chord length, and 0.05 of chord length near the blade tip. Size and resolution of the current mesh system has been validated in the previous work.

6.2.2 Computational Setups

6.2.2.1 Initial and boundary conditions

Uniform inflow condition is assumed at the every background cells as initial conditions. Both sides of the background mesh are set as periodic boundaries to achieve the flow connectivity in the azimuthal direction. The inner and outer boundaries of the background mesh are set as far-field condition.

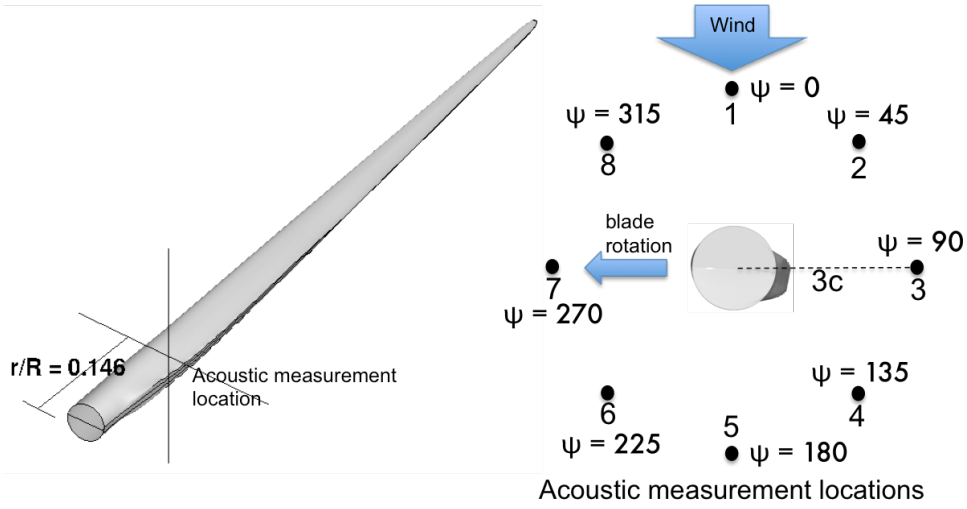

Figure 6.4: Acoustic pressure measurement locations

6.2.2.2 Acoustic Pressure Measurement

Acoustic pressure is measured at 3 times of the maximum blade chord length away from the blade surface. Total eight measurement locations are assigned at the azimuth angle of 0°, 45°, 90°, 135°, 180°, 225°, 270°, 315° with a radius of 3C, as shown in Figure 6.4. The azimuth angles are assigned toward a direction of incoming wind. Thus, in Figure 6.4, the measurement location 1 is 0° in azimuth, 3 is 90°, 5 is 180°, and 7 is 270° in azimuth. Acoustic data is measured for a period of the 2 rotor revolutions with a sampling frequency, 1kHz.

6.2.3 Baseline Blade: SNL100-03FB

6.2.3.1 Inflow conditions

The baseline blade is tested in the flow conditions of the wind speeds of 4.0 - 15.0m/s. A rated wind speed is assumed at 11.3m/s. The baseline blade is designed for a pitch controlled trim mechanism. Beyond the rated wind speed, the blade pitch varies depending on the wind speed. The flow conditions of the current case study are presented in Table 6.1. In the table, rotation speeds, pitch angles and local maximum Reynolds numbers are given from the previous Sandia research paper [53].

Table 6.1: Flow conditions of baseline case

Wind speed(m/s)	Rotor RPM	Pitch(°)	Re($\times 10^6$)
4.0	4.638	0.000	3.305
6.0	5.650	0.000	4.025
8.0	6.933	0.000	4.941
10.0	7.157	0.000	5.101
11.3	7.401	0.000	5.273
12.0	7.438	3.231	5.301
13.0	7.438	6.166	5.301
15.0	7.438	10.120	5.301

6.2.3.2 Overall power prediction of SNL100-03FB

Power coefficients of the SNL100-03FB blade measured by the current DDES are compared with the Griffith's BEM results. Power curves of the BEM and the DDES are compared in Figure 6.5. In the results, the DDES predicted the turbine power generation slightly less than the power calculation by the BEM. It is reason-

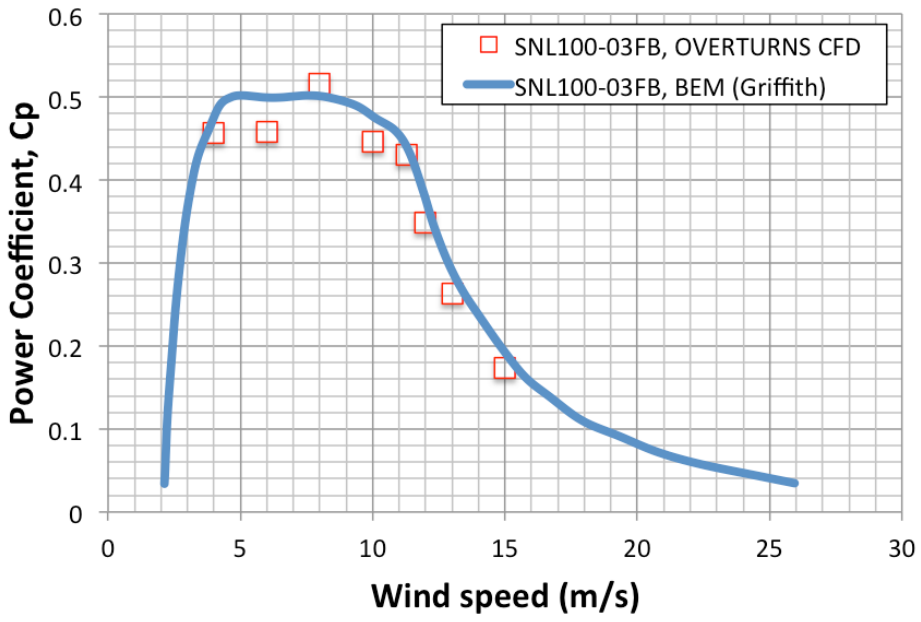

Figure 6.5: Comparison of power generation between BEM and CFD results

able to explain that the reason of this power differences between the BEM and the DDES can be found at the basic assumptions of the BEM. Regarding the difference of the solver characteristics between the BEM and the DDES, measured power by the DDES looks reasonable.

6.2.3.3 Flow-field of SNL100-03FB

Flow at the baseline turbine downstream is presented in Figure 6.6. At the root region, the strong vortical flow sheds from the blade, caused by the massive separation. The highly vortical shedding is dispersed widely through the turbine downstream, but still remains with strong vorticity. Vortical flow at the inboard regions, FB1 and FB2 are less massive than the blade root, but still significant.

Flow comes through the trailing edge is separated rather than attached flow even for the flatback regions of the baseline blade. It may be caused by a not enough bluntness of the flatback trailing edge or out of the optimal blade twist or pitch. Finally, at the very end of the flatback region (0.5r/R), the periodic vortex shedding is appeared in the wake. For a wider view, the iso-vorticity contour shows the broad and strong root wakes caused by the massive separation and clear helical wakes from the tip vortex shedding.

6.2.4 Span-wise Wavy Modified SNL100-03FB

6.2.4.1 Aerodynamic performance of span-wise wavy modification

For the first step of the wavy trailing edge modification test on the baseline blade, the less portion wavy design, 4W-50%t-10%c is chosen for a case study. The 4W-50%t-10%c is not the best aerodynamic design among the tested wavy trailing edge designs because of the too much loss of the lift force (*see* Figure 5.35). However, it is the best acoustic design among the tested designs, which is the only modification eliminating the high frequency tonal sound. Weighting little more on the acoustic noise reduction rather than the power recovery at the blade inboard, the 4W-50%t-10%c might be the best option for the baseline blade.

For the comparison, the wavy modified blade is tested with various wind speeds presented in Table 6.1. Figure 6.8 compares the power generation between the baseline blade and the 4W-50%t-10%c wavy blade for the various wind speed conditions. At the lower wind speeds (under the rated wind speed), the power generation is not

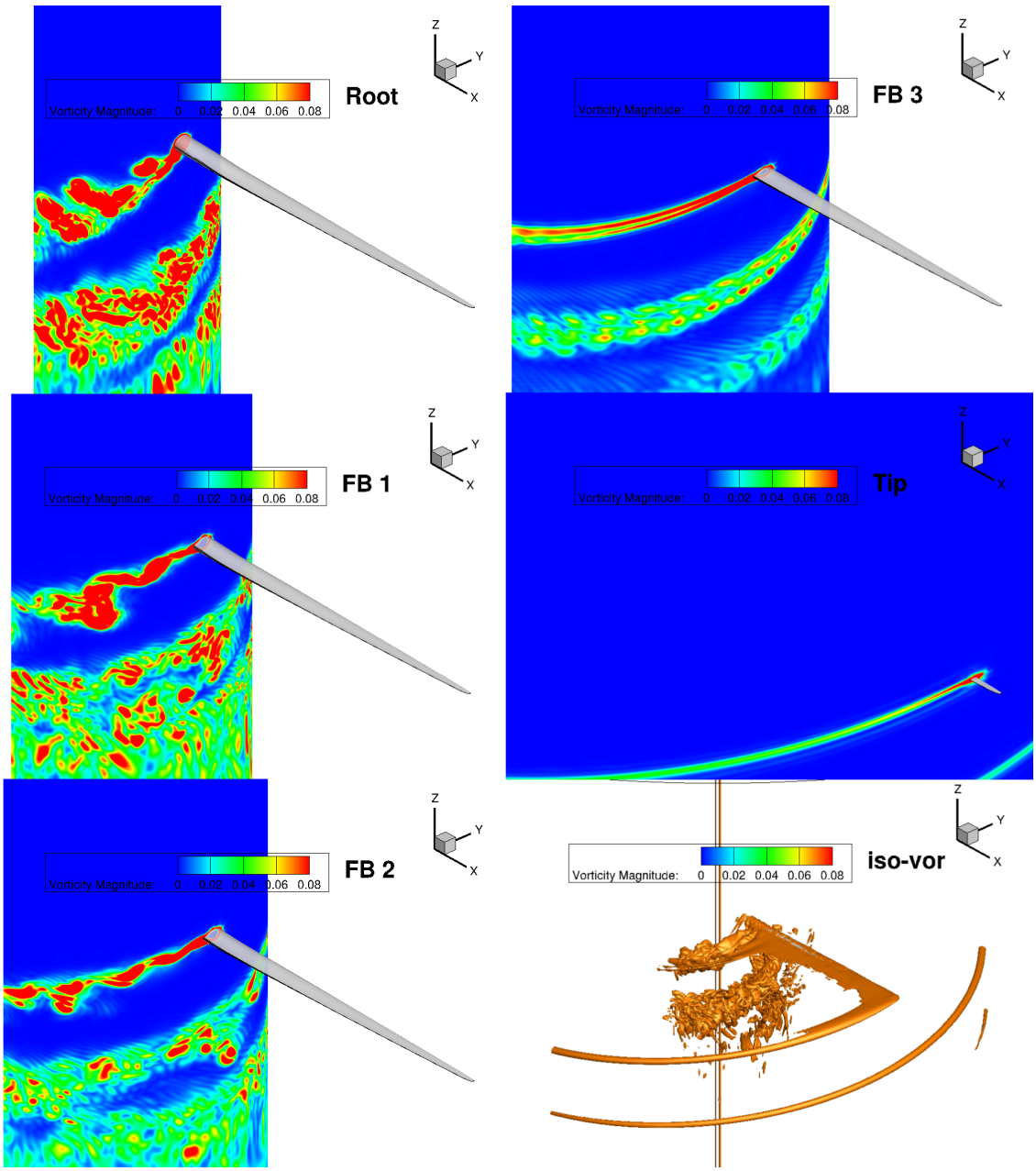

Figure 6.6: Vorticity contours of SNL100-03FB: (top-left) root, (mid-left) 0.165r/R, (bottom-left) 0.230r/R, (top-right) 0.5r/R, (mid-right) 0.95r/R, (bottom-right) iso-vorticity of turbine wake

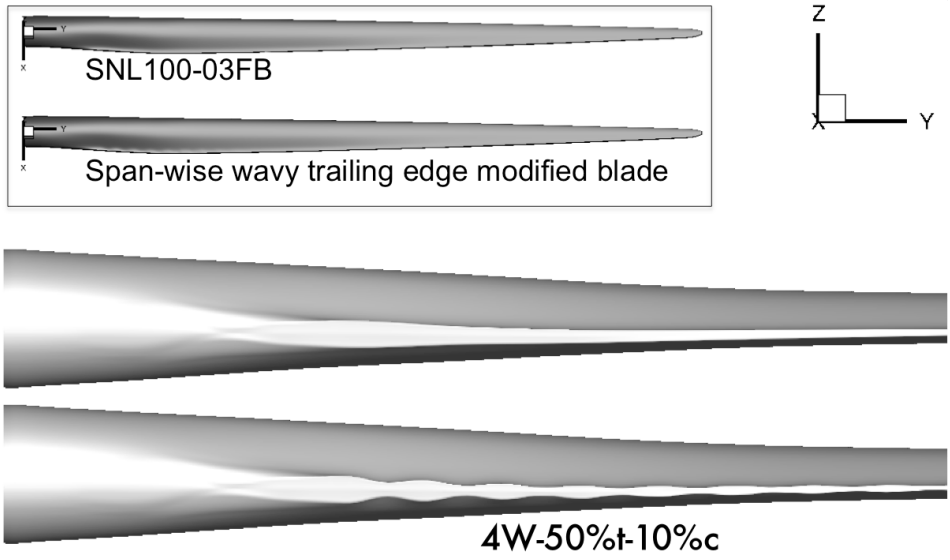

Figure 6.7: 4W-50%t-10%c wavy trailing edge modified blade geometry

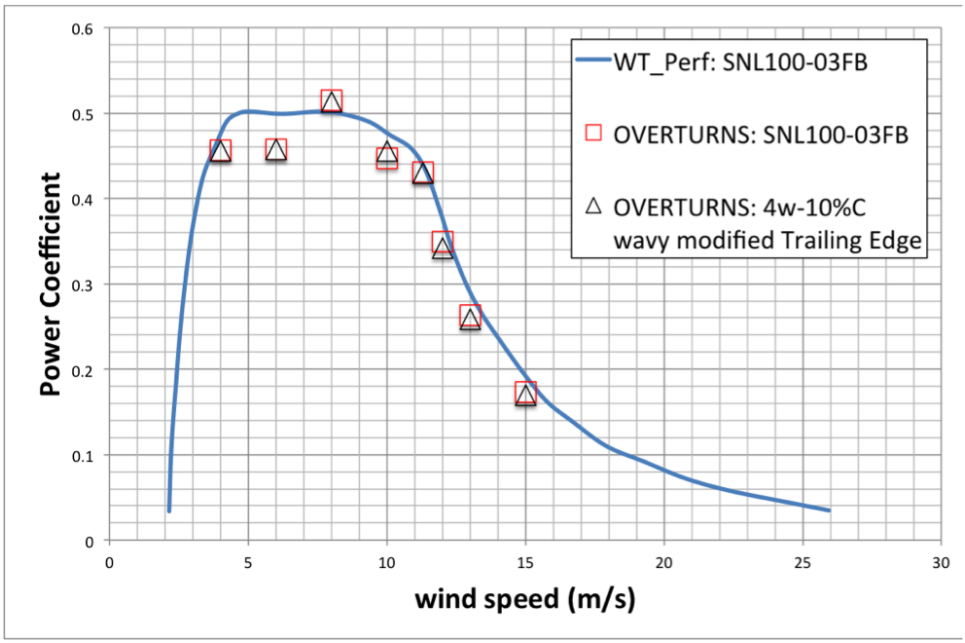

Figure 6.8: Comparison of power generation between baseline blade and 4W-50%t-10%c wavy modified blade

Table 6.2: Comparisons of integrated turbine performance at low wind speed

Modification type	Thrust(kN)	ΔT	Power(MW)	ΔP
SNL100-03FB	701.18	N/A	2.339	N/A
4W-50%t-10%c	699.26	-0.27%	2.338	-0.04%

at wind 6.0m/s

Table 6.3: Comparisons of integrated turbine performance at high wind speed

Modification type	Thrust(kN)	ΔT	Power(MW)	ΔP
SNL100-03FB	1578.3	N/A	14.28	N/A
4W-50%t-10%c	1547.1	-2.0%	13.97	-2.2%

at wind 12.0m/s

very different with those two blades. At the high wind speeds (beyond the rated wind speed), the wavy modified blade produces slightly less turbine power. Table 6.2 and 6.3 compare the integrated turbine power performance. At the lower wind speed (6.0m/s), the span-wise trailing edge modification reduces only 0.27% of the turbine thrust, and 0.04% of the turbine power generation. However, at the higher wind speed (12.0m/s) there are 2.0% of the thrust loss and 2.2% of the power loss. This is a notable power loss as it is calculated in AEP.

Figure 6.9 compares the vortex shedding of the original blade and the wavy modified blade. At the lower wind speed (6m/s), the vortex shedding between those two blades are almost identical. However, at the higher wind speed (12m/s), the strong inboard vortex shedding is observed at the much broader regions in the wavy modification case. It could be the main reason causes the power loss of the wavy modification at the high wind speed region. Figure 6.10 shows the power loss at the

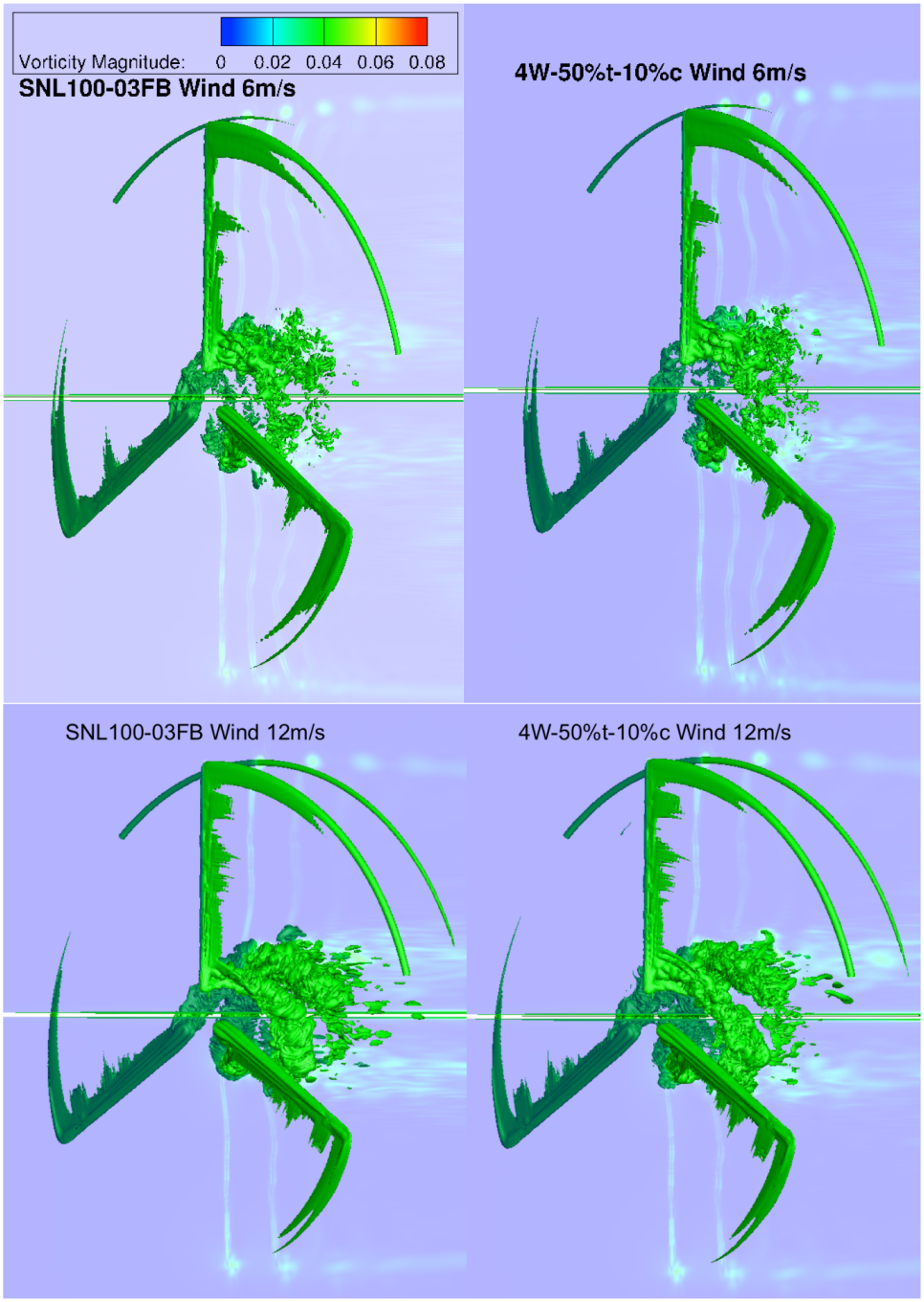

Figure 6.9: Comparison of iso-vorticity contours between SNL100-03FB and 4W-50%t-10%c wavy modified blade; at wind speed 6m/s (upper), 12m/s (lower)

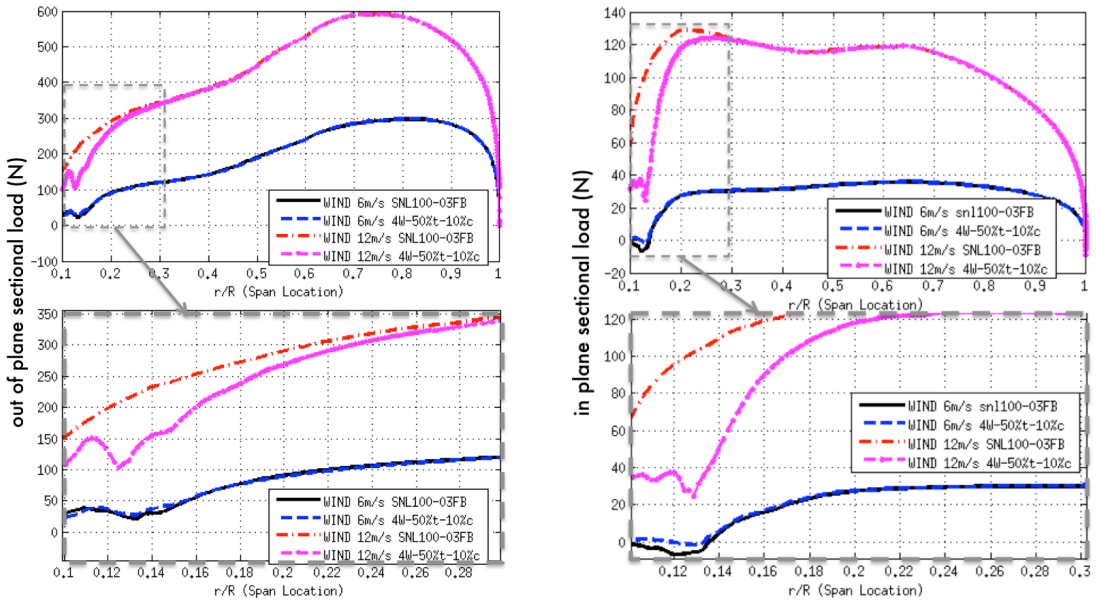

Figure 6.10: Comparison of sectional airloads between SNL100-03FB and 4W-50%t-10%c wavy modified blade; at wind speed 6m/s (upper), 12m/s (lower)

high wind speed very well. At the wind speed 12m/s, both the in and out of plane sectional loads are lower at the inboard of the wavy trailing edge modified blade.

6.2.5 Trailing Edge Augmented SNL100-03FB

6.2.5.1 Required trailing edge thickness for preventing separation flow

After investigating the wavy trailing edge modified SNL blade, we noticed our wavy modification will not work as a drag reducer, since the cross flow separated massively at the inboard of the original blade. The span-wise wavy trailing edge modification is designed for the flatback trailing edge flow which is attached flow

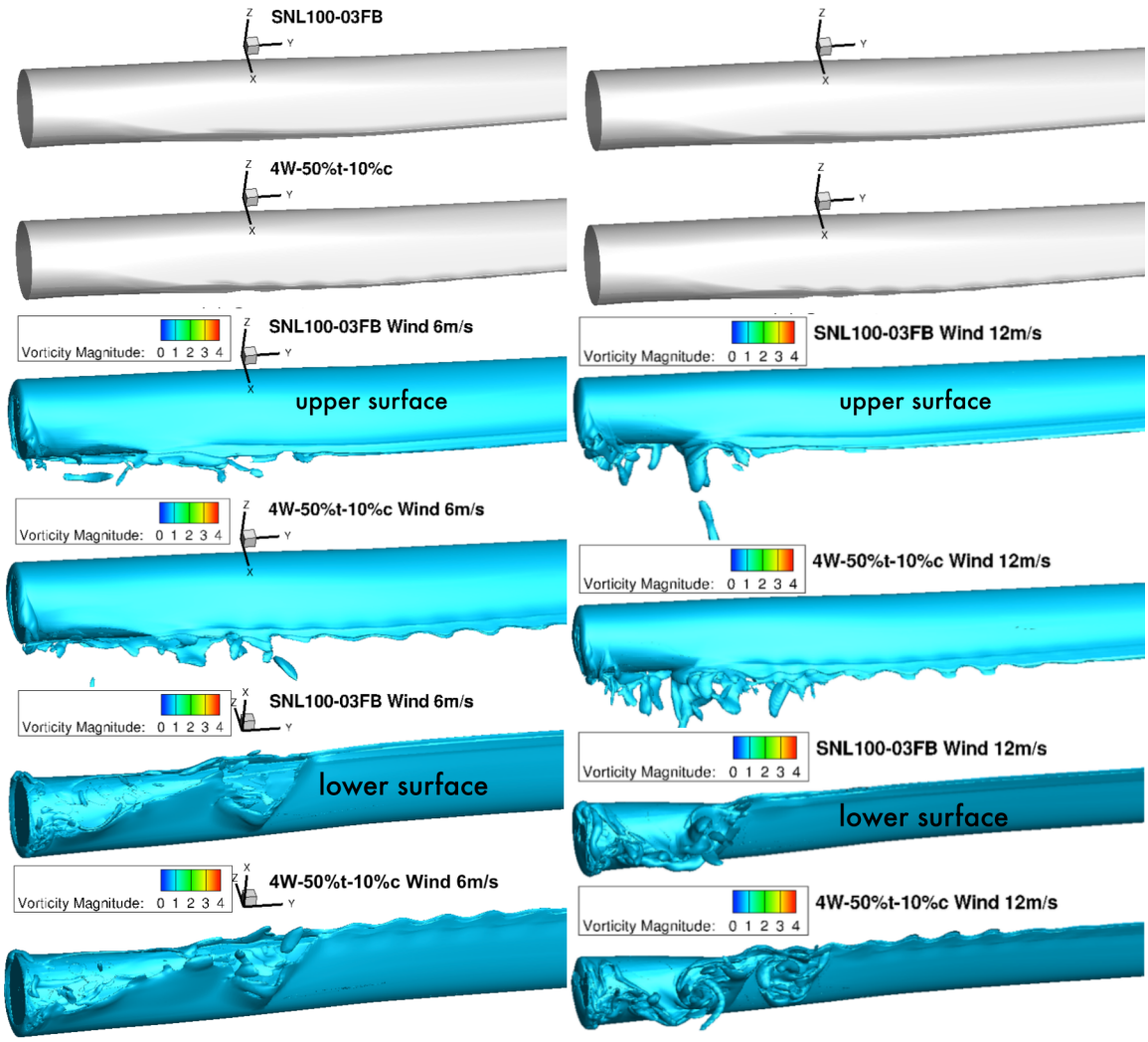

Figure 6.11: Comparison of inboard separation between SNL100-03FB and 4W-50%t-10%c wavy modified blade; at wind speed 6m/s (upper), 12m/s (lower)

rather than the massive separated flow. Probably, the simplest way to solve this matter is to increase the trailing edge thickness at the inboard locations.

Several research projects have studied the trailing edge thickness augmentation for a method of blade inboard separation prevention, such as R. Chow and C.P. van Dam [54]. From the previous efforts, it figured out that the inboard trailing edge augmentation helps to prevent separation onset, but more efforts is required to achieve a benefit to turbine power generation. In the current study, proper amount of trailing edge augmentation is estimated using the outcomes of the parametric study.

Figure 6.12 shows a flow over the original blade inboard. For this figure, the rotor rotates with 7.401 rpm, wind speed 11.3m/s and blade pitch is 0°. Although the blade pitch is 0°, the local airfoil is nose-downed toward wind upstream since local blade twists are applied such as 11.13° for location of L1, 5.18° for location of L2 and 5.00° for location of L3. From the figure, the massive separation is observed at the location of 0.163r/R and 0.256r/R. Recalling the previous parametric study, a ratio between the airfoil thickness and the trailing edge thickness of the airfoils shown in Figure 6.12, seems not enough to prevent the flow separation. Previously tested FB3500-1750 airfoil prevents the flow separation at the ranges of angle of attack 0° to 12°, and its airfoil thickness is, $t/c = 0.3500$ and trailing edge thickness is $t_{te}/c = 0.1750$. It means the airfoil thickness to the trailing edge thickness is $t/t_{te} = 0.5000$. Table 6.4 compares airfoil thickness to trailing edge thickness ratio between the FB3500-1750 and airfoils of the SNL100-03FB blade inboard. Both the 'Interp-016300' and 'FB-3423-0596' has much lower t_{te}/t compares to the FB3500-

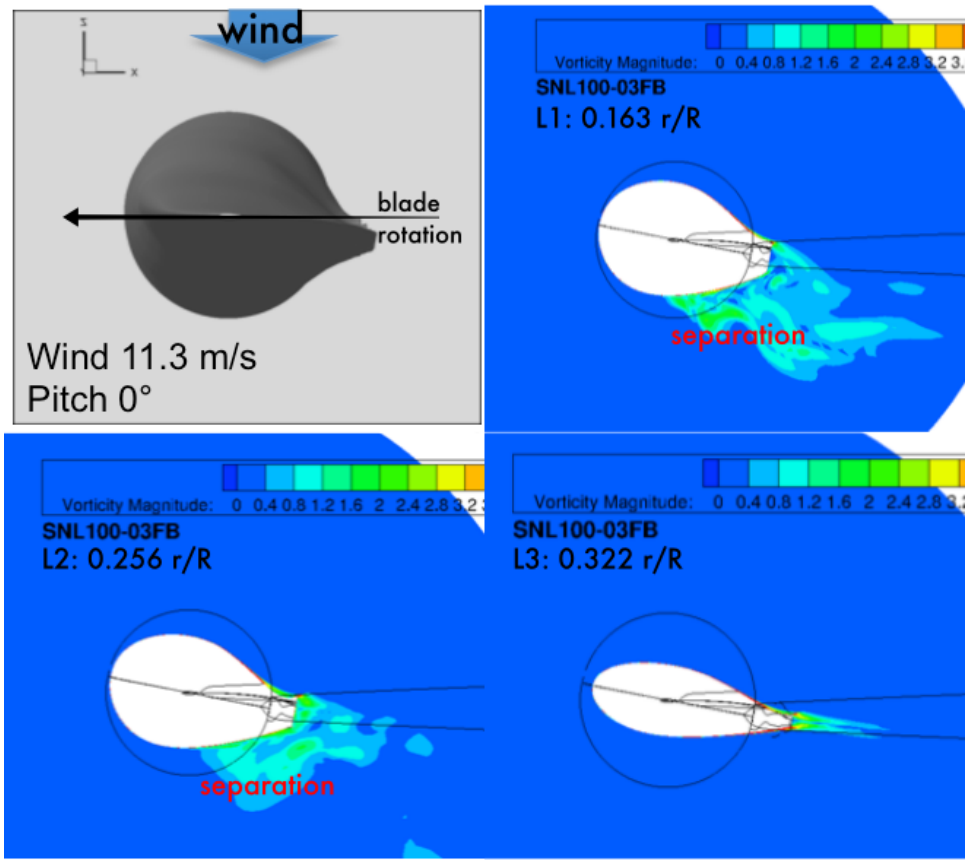

Figure 6.12: Massive separation over SNL100-03FB blade inboard at wind speed 11.3m/s

1750. Those results imply more trailing edge thickness similar to the FB3500-1750 is required to prevent the inboard separation. For this, if trailing edge thickness is augmented as 50% larger, the t_{te}/t ratios of the airfoils will be a little lower than 0.5 as presented in Table 6.5. Now, the t_{te}/t ratio is more close to the FB3500-1750.

6.2.5.2 50% trailing edge augmentation on SNL100-03FB

Trailing edge thickness of the SNL100-03FB inboard is augmented with 50%. For the first step, 50% trailing edge augmentation is applied to a region between

Table 6.4: Airfoil thickness to trailing edge thickness ratio of SNL100-03FB blade inboard at L1:0.163r/R and L2:0.256r/R

Airfoil	airfoil thickness (t/c)	TE thickness (t_{te}/c)	t_{te}/t ratio
FB3500-1750	0.3500	0.1750	0.5000
Interp-016300	0.5025	0.1036	0.2062
FB3500-3423-0596	0.3418	0.0596	0.1743

Table 6.5: Airfoil thickness to trailing edge thickness ratio of 50% augmented SNL100-03FB blade inboard at L1:0.163r/R and L2:0.256r/R

Airfoil	airfoil thickness (t/c)	TE thickness (t_{te}/c)	t_{te}/t ratio
FB3500-1750	0.3500	0.1750	0.5000
Interp-016300	0.5025	0.2073	0.4125
FB3500-3423-0596	0.3418	0.1192	0.3487

0.11r/R and 0.50r/R of the baseline blade as shown in Figure 6.13. It may be over trimmed modification (since, the modified region includes blade mid-board, too), but it would be a good start to glance the effect of the trailing edge augmentation.

The isolated rotor simulation is conducted with the flow conditions of wind speed 11.3m/s, and rotation speed 7.401rpm. Same mesh points and overset system of the baseline case is used. Figure 6.14 compares the time-averaged sectional air-loads between the baseline and trailing edge augmented blade. In the figure, the out of plane airloads are increased with the trailing edge augmentation at the blade inboard, locations between 0.0 - 0.25r/R. At this inboard location, the in plane airloads are also increased. However, beyond 0.25r/R and up to 0.5r/R, the in plane airloads are decreased. Thus, in this case, the turbine will generate the more power at the inboard location between 0.11 - 0.25r/R, but will loss the power

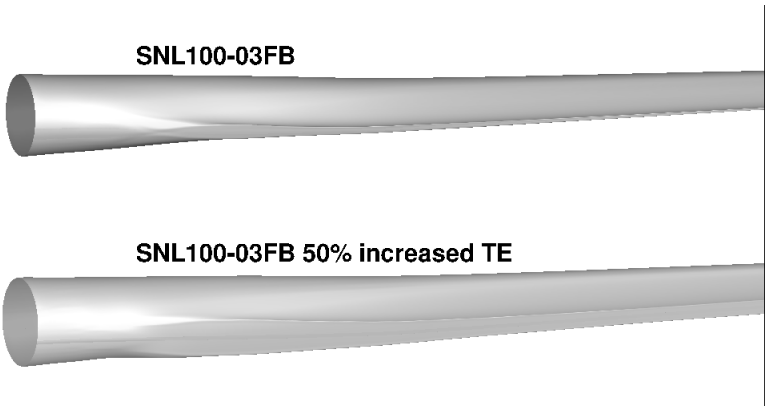

Figure 6.13: 50% trailing edge augmentation on blade span 0.11 - 0.50r/R of SNL100-03FB

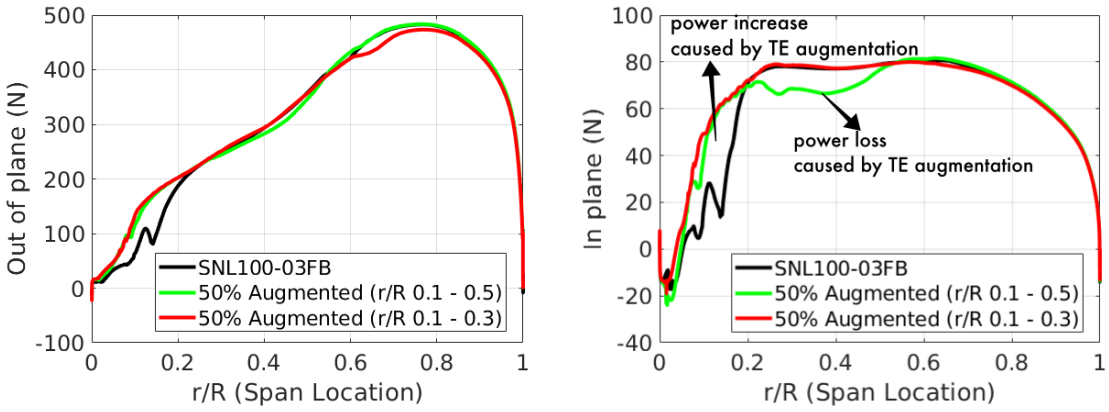

Figure 6.14: Comparisons of sectional air-load between the baseline, 50% augmented trailing edge at span 0.11-0.50r/R

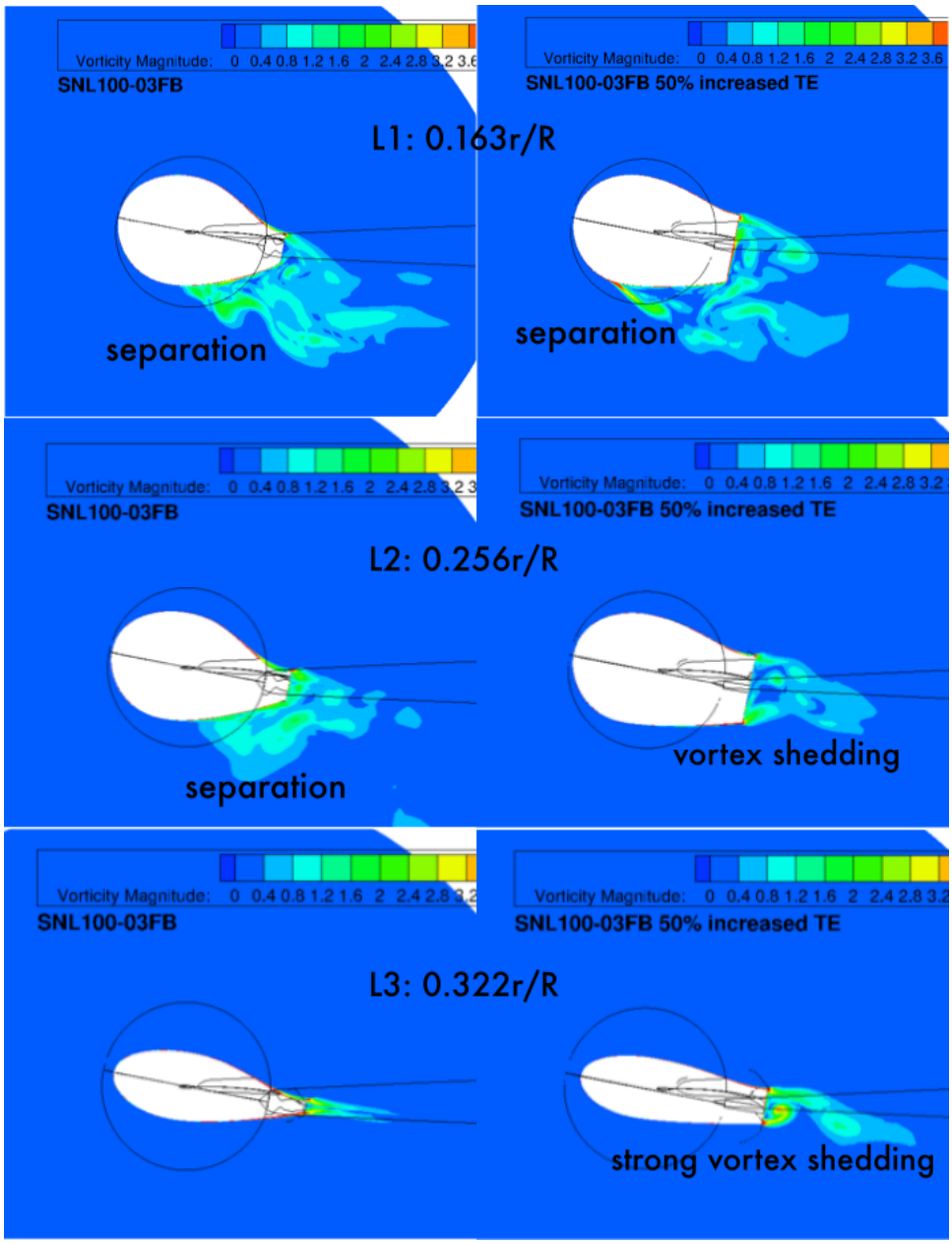

Figure 6.15: Comparisons of trailing edge vortex shedding between the baseline, 50% augmented trailing edge at span 0.11-0.50r/R

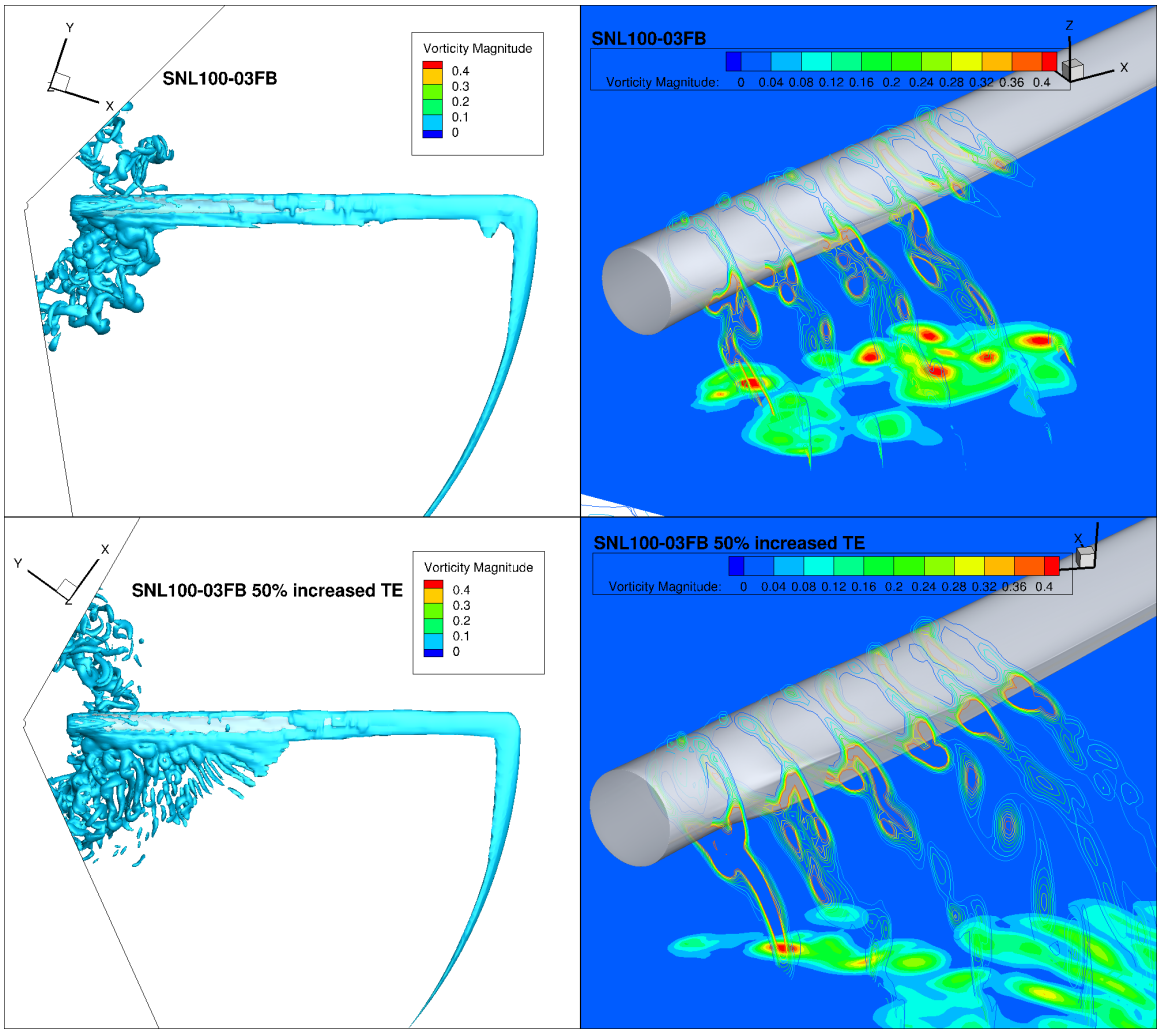

Figure 6.16: Comparisons of iso-vorticity between the baseline, 50% augmented trailing edge at span 0.11-0.50r/R

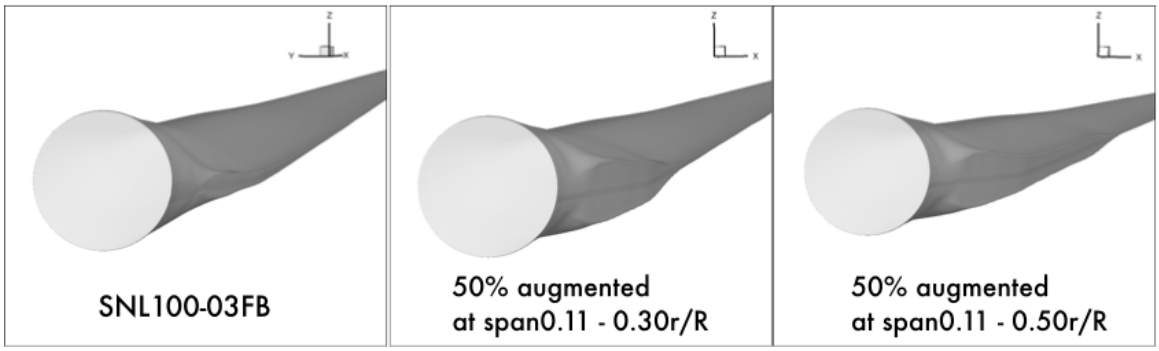

Figure 6.17: 50% trailing edge augmentation on blade span 0.11 - 0.30r/R of SNL100-03FB

generation at the mid-board location between 0.25 - 0.5r/R. The main reason of this mid-board power loss is the aerodynamic drag increase caused by the trailing edge augmentation. Recalling the sectional airloads distributions of the baseline blade, the inboard power loss caused by the flow separation occurs at the location between 0.0 - 0.3r/R.

Figure 6.15 compares the flow over the two different blades. At the very close to the root L1 (0.163r/R), the massive separation flow occurs in the both baseline and trailing edge augmented blade. At the little outward location, L2 (0.256r/R), flow separation is prevented by the trailing edge augmentation. However, at the location of L3 (0.322r/R), no separation occurs on the baseline blade, and the trailing edge augmentation enhances the trailing edge vortex shedding. Figure 16.6 shows the difference more clearly. Clear periodic trailing edge vortex sheds off from the augmented trailing edge.

Figure 6.17 shows another trailing edge augmentation design. Based on the previous result, locations of the trailing edge augmentation is changed as the location

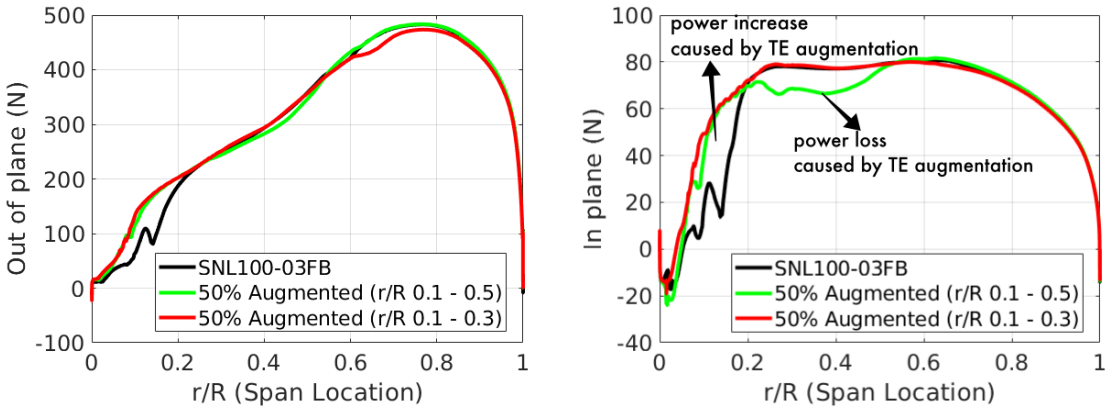

Figure 6.18: Comparisons of sectional air-load between the baseline, 50% augmented trailing edge at span 0.11-0.50r/R and at span 0.11-0.30r/R

between 0.11 - 0.30r/R. Now it recovers the mid-board power loss caused in the previous case as shown in Figure 6.18. It is encouraging in a view of the turbine power generation. As calculating integrated turbine power, this inboard power gain brings about 1.45% of the original turbine power generation. However, in a view of the acoustic performance, the strong trailing edge vortex shedding would be a problem, since it causes a tonal sound noise. More detailed discussions of the turbine power generation and the acoustic noise of the trailing edge augmentation is presented in the next section.

6.2.6 Blunt-Wavy Combined (BWC) Trailing Edge Modified SNL100-03FB

In the previous section, effect of the trailing edge augmentation is studied. Based on the previous isolated rotor test, the blunt trailing edge prevents the inboard

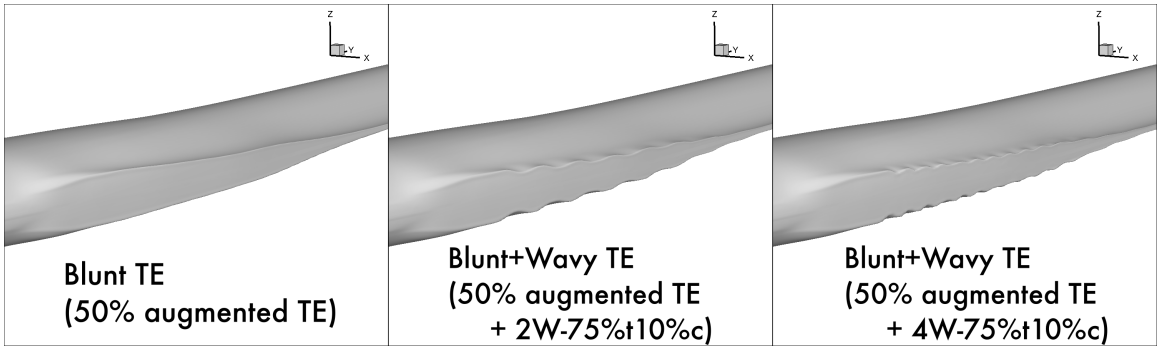

Figure 6.19: Comparisons of geometries between the 50% augmented trailing edge at span 0.11-0.30r/R, and adding 2W-75%t-10%c and 4W-75%-10%c wavy trailing edge

separation, but evolves the trailing edge vortex shedding which may cause a tonal noise emission. In the current step, it is expected that adding the span-wise wavy trailing edge modification on the trailing edge augmentation helps to break down the trailing edge vortex, and results in the tonal noise mitigation. This combination of the trailing edge modifications are named as '**Blunt-Wavy Combined (BWC)**' trailing edge modification in the current study.

For the test, two best aerodynamic and aeroacoustic performance designs, the '2W-75%t-10%c' and the '4W-75%t-10%c' wavy trailing edge designs are used for the current BWC modification. Geometries of the two BWC trailing edge modified blades are shown in Figure 6.19.

6.2.6.1 Aerodynamic performance of BWC trailing edge modification

Recalling the previous section, for the baseline blade inboard, two flow separations locate at r/R 0.1 and 0.15, and they causes the immediate power loss at the

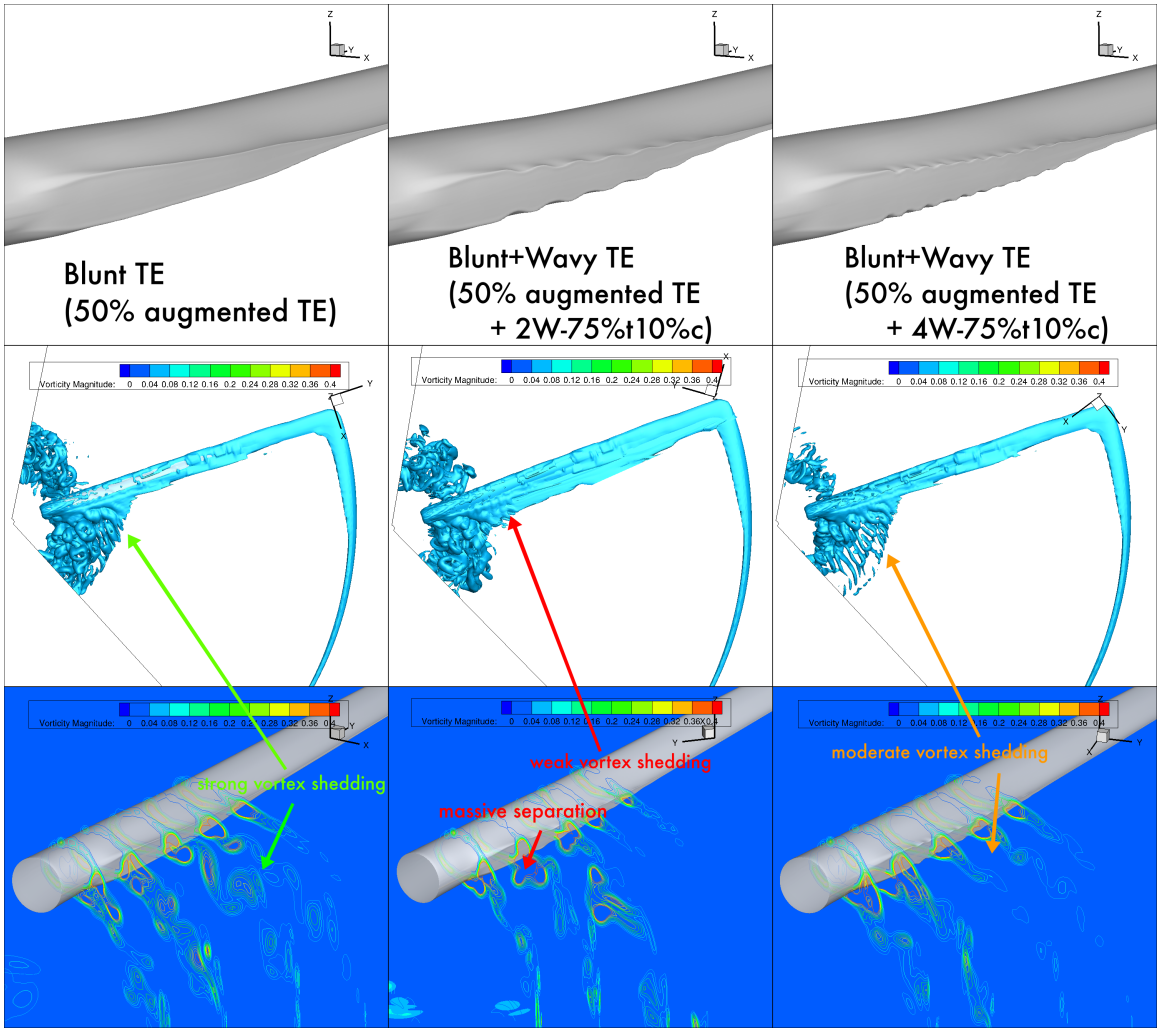

Figure 6.20: Trailing edge vortex structures of BWC trailing edge modified blade: (top) 2W-75%t-10%c, (bottom) 4W-75%t-10%c

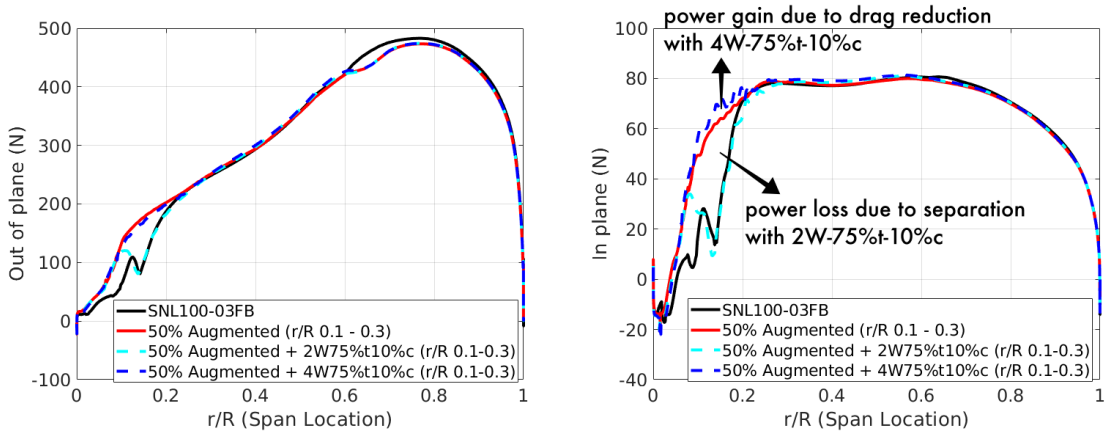

Figure 6.21: Comparisons of sectional airloads between Blunt trailing edge and Blunt-Wavy Combined modification

blade inboard region between r/R 0.1 and 0.25. As shown in the previous section, this power loss can be recovered by 50% of the trailing edge augmentation. However, it causes a tonal noise source, strong trailing edge vortex shedding. Adding the span-wise wavy modification on the 50% trailing edge augmented blade may help to break up the vortex shedding.

Figure 6.20 compares the trailing edge vortex shedding structures of the simulated blades. As we found in the previous section, the 50% augmented trailing edge prevents the massive separation at the blade span between 0.1 to 0.3 r/R, but generates the strong vortex shedding from its highly blunted trailing edge. With the longer wave length, 2W-75%t-10%c successfully suppresses the trailing edge vortex shedding, but can not prevent the massive flow separation at the transition region (airfoil transition between blade root and inboard). This massive separation will cause the inboard power loss of the BWC modification with 2W-75%t-10%c wavy

design, but the successful control of trailing edge vortex shedding must be a benefit in perspective of acoustic noise.

With adding on the shorter wave length, 4W-75%t-10%c design on the 50% augmented trailing edge, the massive separation at the blade root to inboard transition region is much suppressed. However, stronger trailing edge vortex shedding occurs at the inboard region. Now, the new modification gives the aerodynamic benefit and aeroacoustic disadvantage.

Figure 6.21 compares the sectional airloads. Two different types of the wavy modification shows the very different aerodynamic performance at the blade inboard. With the longer wave length design, 2W-75%t-10%, prevents the first separation (the one near the root), but the second separation is still occurred at the same location of the baseline blade. For the aerodynamic performance, using the shorter wave length, 4W-75%t-10%c, looks more efficient. This BWC modification prevents the both inboard separation flows, and also breaks up the standing vortex shedding at the trailing edge. It decreases the pressure drag at the blade inboard, thus the in plane sectional airloads increases at the region.

Table 6.6 compares the turbine thrust and power generation between the baseline blade, 50% augmented trailing edge and 50% augmented and blunt-wavy combined modification with 4W-75%-10%c. We have already figured out that the 50% trailing edge augmentation on 0.11 - 0.30 of span increases about 1.45% of the power generation at the rated wind speed. Now, adding the 4W-75%t-10%c wavy pattern on the blunt trailing edge increases additional 1.17% of the power generation. This is 2.62% higher power generation than the baseline blade.

Table 6.6: Comparisons of integrated turbine performance at rated wind speed, 11.3m/s

Modification type	Thrust(kN)	ΔT	Power(MW)	ΔP
SNL100-03FB	1858.4	N/A	14.52	N/A
50% augmented TE	1881.2	+1.23%	14.73	+1.45%
50% augmented TE + 4W-75%t-10%c	1887.3	+1.56%	14.90	+2.62%

at wind 11.3m/s

Revisiting the results of parametric study, the result above is interesting, since aerodynamic characteristics of those two wavy designs were almost identical in the parametric study. This difference may be caused by one of two main reasons such as three-dimensional effect of the blade geometry and centrifugal effect or both.

In addition, It figured out using the longer wavy patterns (2W-75%t-10%c wavy) at the root-inboard transition region does not help to suppress flow separation. Flow sensitivity is much higher at the region, since the local angular velocity is relatively lower than other outward span locations on the blade. Thus we might need a shorter wavy pattern for the transition location rather than the 2W-75%t-10%c. It is already figured out in the previous parametric study that the shorter wavy patterns are tend to get less separation.

6.2.6.2 Aeroacoustic performance of BWC trailing edge modification

To examine the inboard acoustic noise characteristics of the simulated trailing edge modifications, an acoustic analysis is conducted. Time history of the pressure fluctuation is measured at around the blade inboard. Details of the measurement

locations are shown in Figure 6.4. The Fast Fourier Transformation (FFT) is performed on the measured pressure fluctuation data with using the 1/3 octave band filter. Sound Pressure Level (SPL) in frequency frame of the measured data is plotted in Figure 6.22. The sound pressure level is expressed in decibel, and $20m\mu pa$ is used as reference pressure. The figure compares acoustic noise emissions of the baseline, blunt trailing edge modification (50% augmented) and both BWC trailing edge modifications with the short(4W-75%t-10%c) and long(2W-75%-10%c) wave patterns.

Most of significant noise is measured within a range of frequency between 0.2 to 15Hz. Reminding the rotor is at relatively slower rotation (Ω = 7.401 rpm), it seems reasonable such a lower frequency band noise. In the figure, the high amplitude acoustic noise is measured at the azimuth, $\psi = 135^\circ$ of the baseline blade. Re-visiting the vorticity magnitude contours shown in Figure 6.6, 6.16 and 6.20, the measurement locations of the azimuths, $\psi = 90^\circ, 135^\circ, 180^\circ$ and 225° are within the rotor inboard wake or near the wake. Acoustic noise is significantly higher in the rotor wake for all the tested blades. However, for the baseline (black-dot line), high amplitude noise is measured only at the azimuth, $\psi = 135^\circ$ in a broad band frequencies. The noise pattern is less tonal, but more broad band, thus it is a typical noise characteristics of the separated flow.

In contrasts, the noise of the blunt trailing edge modified blade (50% augmentation) looks more tonal (red-square line). At the azimuth location, $\psi = 90^\circ$, three of tonal peaks are clearly seen at the frequencies of 4, 7 and 11Hz. These peaks are also shown in the other measurement locations in the turbine wake.

Adding the wavy patterns on the blunt trailing edge helps to mitigate the amplitude of the tonal noise. Both BWC modifications decreases the tonal noise peaks of the trailing edge augmented blade by 5-10dB for the 4W-75%t-10%c (green-triangle line) and 15-20dB for the 2W-75%-10%c (blue-triangle line). This is reasonable results as recalling the trailing edge vortex structures shown in Figure 6.20. Now it is figured out acoustically the best design is not aerodynamically the best. Thus, it must be an interesting discussion how we make a trade-off the each modification design for the best performance.

Now, regarding the baseline blade, Figure 6.23 and 6.24 compare the vortex shedding off the tested blades' inboard. In Figure 6.23, one can easily notice there are two of massive flow separation occur in the baseline blade. These are no longer existed in the blunt trailing edge and the BWC trailing edge modifications. However, the periodic vortice shed off the blunt trailing edge at more broad blade inboard region. By applying the span-wise wavy design to the blunt trailing edge region, the periodic vortice of the blunt trailing edge is much weaken as shown in Figure 6.23.

The difference of these trailing edge vortex shedding can be found more clearly in the iso-vorticity contours and cross sectional view of vortex structures as described in Figure 6.24. Periodic formation of the strong vortex cores shed off the blunt trailing edge and much weaker vortex cores from the BWC modified blade are clearly captured in the figure. These two figures explain the power recovery of the blunt trailing edge and well designed BWC modified trailing edge, and the acoustic noise reduction by the BWC modified trailing edge blade.

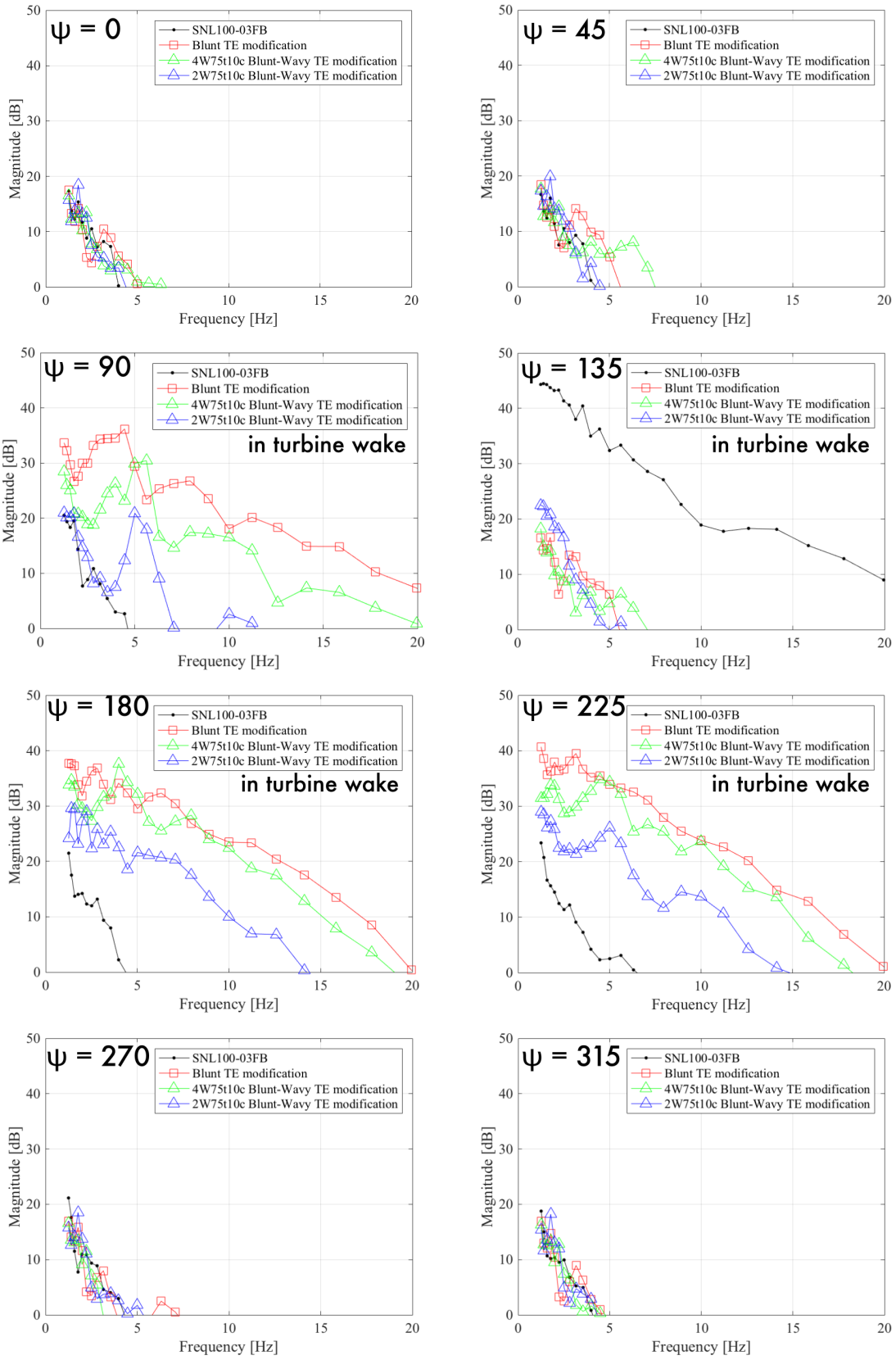

Figure 6.22: 1/3 octave band acoustic noise around the tested blades

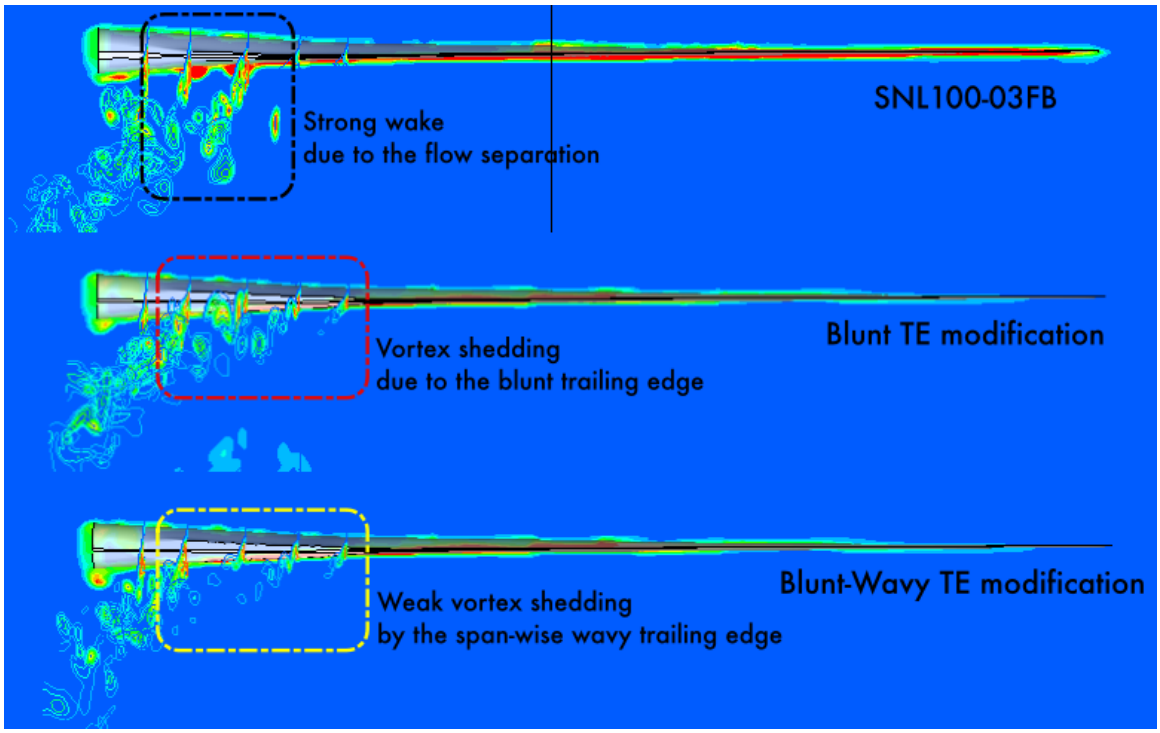

Figure 6.23: Comparison of trailing edge vortex structure between baseline, blunt trailing edge modification and blunt-wavy combined trailing edge modification in in-plane view

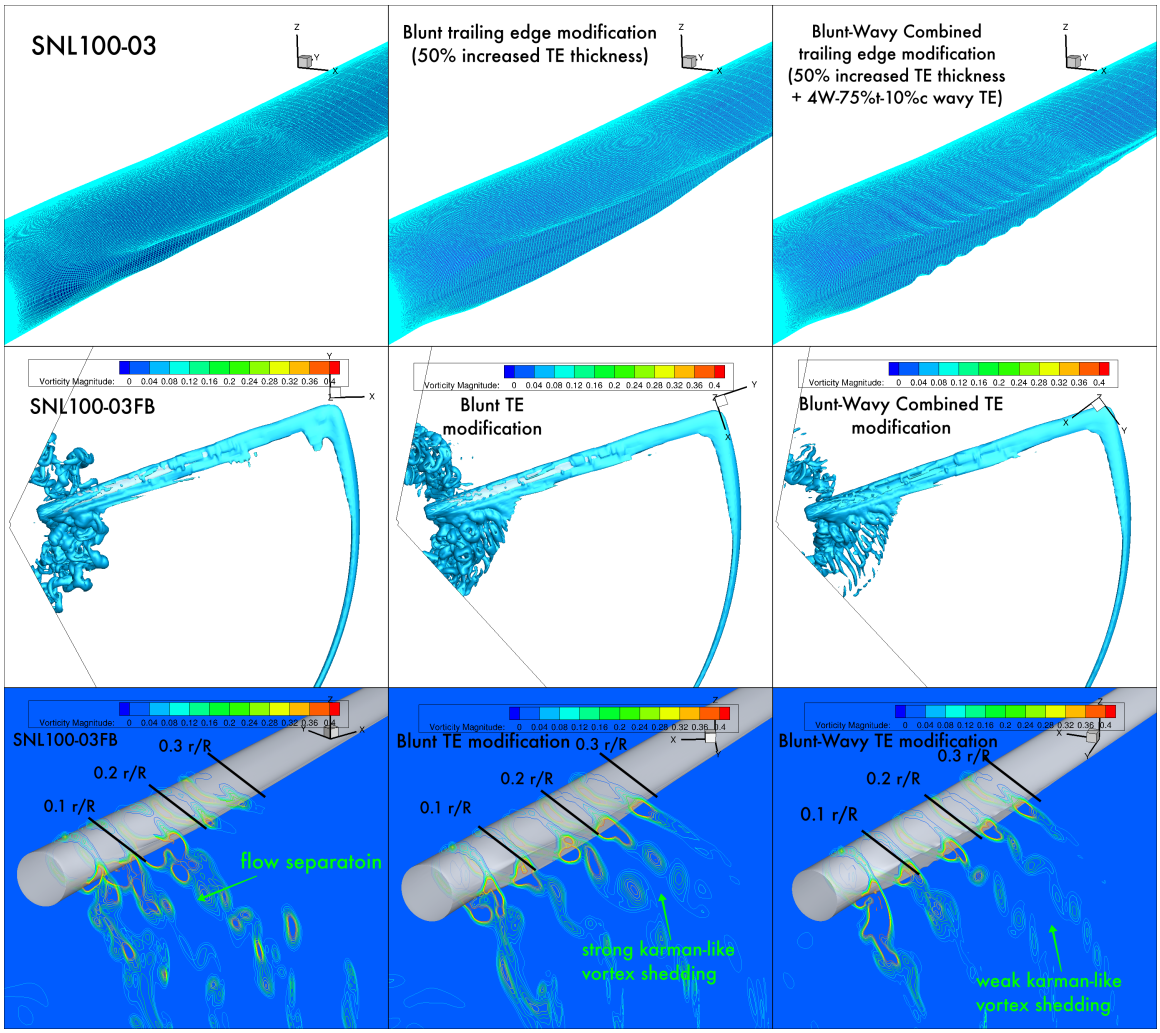

Figure 6.24: Comparison of inboard trailing edge vortex structure between baseline, blunt trailing edge modification and blunt-wavy combined trailing edge modification

6.3 Remarks of Span-wise Wavy Modified SNL100-03FB

The isolated rotor simulation considers only a rotor itself, and ignores the other wind turbine configurations such as a nacelle, tower and else. For more realistic wind turbine simulations, these parts should be included in a computational domain. However, in the current step of the study, numerous test cases were required, because of, the large numbers of trailing edge design candidates. Thus focusing on the isolated rotor assumptions are reasonable for the current study. However, if the thesis of this study becomes more realistic, a CFD of full configuration including a nacelle and tower should be followed.

Although the 2W-75%t-10%c wavy design reduces such a large amount of tonal noise, its power loss at inboard is significant comparing to the 4W-75%t-10%c. Reversely, the BWC with the 4W-75%t-10%c design provides about 2.62% of the power increase, and 5 to 10dB of the acoustic noise reduction as well. To satisfy benefits of both aerodynamic and aeroacoustic performance in the same time, the BWC modification with the 4W-75%t-10%c must be the best design selection.

Chapter 7: Conclusions

7.1 Summary

In the current study, the span-wise wavy trailing edge design has been proposed for the drag and noise reduction of flatback trailing edge airfoil. Use of the flatback trailing edge in blade designs, enhances the structural robustness of the blade, in the other hand, increases the sectional drag and tonal noise emission which mainly caused by large standing flow and span-wise vortex shedding at the trailing edge region. The span-wise wavy trailing edge creates small amount of local flow separations at the trailing edge which help to break up the standing flow and span-wise trailing edge vortex shedding, and results in the sectional drag and noise reduction.

To investigate its aerodynamic and aero-acoustic performance, a design parametric study of the wavy modified airfoils and isolated blade simulations were carried out, using the Delayed Detached Eddy Simulation technique. Regarding the structural benefit of the flatback airfoil, the best span-wise wavy trailing edge design should satisfy; minimizing changes from the flatback while maximizing the drag and noise reduction. Based on the current parametric study, the minimized modification span-wise wavy trailing edge airfoil (the 4W-75%t-10%c, only the last 10% of airfoil modified) reduce 60% of the sectional drag while only 7% lift loss (150% L/D

increase), and reduce the tonal noise about 25dB.

The isolated blade simulations were performed for the trailing edge augmented SNL 100 meter blade and its span-wise wavy trailing edge modification. 50% of trailing edge augmentation results in 1.45% of overall power increase (compared to the original blade), but generates low frequency tonal noise. Applying the best aerodynamic wavy trailing edge design (4W-75%t-10%c airfoil) on the trailing edge augmented blade, the overall power generation increases by 2.62% (compared to the original blade). In the meanwhile, applying the best aero-acoustic wavy trailing edge design (2W-75%t-10%c airfoil), the tonal noise caused by the trailing edge augmentation decreases by the maximum 50dB (SPL).

Conclusive summaries of the each chapters are presented as follows.

1. In Chapter 1, state of the art of the modern large wind turbine blade design and flatback airfoil for wind turbine blade applications was briefly introduced. It was mentioned that the current trend of commercial blade sizing up is critically depending on their blade mass reduction techniques. The flatback airfoil design is one of the promising mass reduction techniques. It was pointed out that the idea of a flatback airfoil works greatly to enhance the structural strength of turbine blade, but it increases the pressure drag and generates tonal acoustic noise. Thus it may require drag and noise reduction devices for future large wind turbine blade designs.

   Next in the chapter, background of the modern wind turbine noise was introduced. Environmental effect of the wind turbine noise isn't severe compared

to other electricity power plants, however its low frequency noise might be also harmful to the surrounding nature and human beings nearby. Main sources of the wind turbine blade noise are categorized. Focusing on the inboard noise, it will be deep stall (TBL-TE) noise if there is flow separation or blunt trailing edge noise if there is strong trailing edge vortex shedding rather than the separation. One may expect the blunt trailing edge noise which is tonal and low frequency, if the flatback airfoil is applied.

Towards the end of Chapter 1, currently existing solutions of the drag and noise reduction techniques for flatback airfoil were introduced. All of the current solutions are add-on type devices. It may require additional task and cost in the manufacturing or maintenance process. Also add-on type devices have more risk of failure, such as the part falling off. Developing a non add-on type drag and noise reduction design for the flatback airfoil must be a solution for these potential problems. This is the main motivation and objective of the current study.

2. In Chapter 2, aerodynamic performance of the current add-on devices were discussed. Based on the previous studies, splitter plates reduce the sectional drag of flatback airfoil by around 50% in the best cases. Trailing edge cavities reduce the sectional drag by around 20-25%, but if they are modified with ventilation slots, the sectional drag reduction is about 50-60%. Serrated trailing edge add-ons are probably the most interesting noise reduction design at the current time. Many different types of serrated trailing edges have been

tested. Based on previous research, the serrated trailing edges reduce the sectional drag by 35-65% depending on the design and flight conditions (Mach numbers, Reynolds numbers).

3. In Chapter 3, the proposed span-wise wavy trailing edge was described in detail. The wavy design is originally inspired by tubercles of humpback whales, which offer better maneuverability to the whale. Similarly, the span-wise wavy trailing edge is expected to reduce the airfoil drag by implementing span-wise wave patterns on the trailing edge.

4. In Chapter 4, numerical methods employed in the current study were explained. A hybrid RANS-LES method, Delayed Detached Eddy Simulation, was selected. For the baseline turbulence model, the Spalart-Allmaras one equation model was used. To resolve flow separation and turbulent eddies, the Medida-Baeder laminar-turbulent model is used with adverse pressure gradient correction. In the current study, in house developed flow solvers, GPURANS3D and OVERTURNS are used. GPURANS3D is a GPU-based solver, and it was mainly employed for the wavy design parametric study. OVERTURNS is a CPU-based solver, and it was mainly used for the isolated rotor cases.

5. In Chapter 5, a design parametric study of the proposed span-wise wavy trailing edge was discussed. Wave length, wave depth and wave portion were considered as key design parameters. A total of 16 designs variations of the wavy trailing edge airfoil have been created and simulated based on a flatback

airfoil, FB3500-1750.

Conclusive results showed the wave thickness should be larger than 50% of the original blunt trailing edge (50% - 75%), and the wave length should be longer than $0.25c$ to get maximum aerodynamic and aeroacoustic performance benefits. Two different types of the less portion wavy trailing edge were investigated.

Regarding potential structural benefit, the 10%c less portion wavy design must be a better choice, as compared to the halfway-cut wavy trailing edge. Interestingly, the 10%c less portion wavy design showed better aerodynamic and aeroacoustic performance compared to the maximum portion of wavy trailing edge design.

In order to figure out the main reason for these benefit, a relation between the local flow separation at the wave paves and trailing edge vortex shedding was investigated. Eventually, it turned out that the moderate amount of flow separation on the wave paves prevents the trailing edge vortex shedding, while massive flow separation causes vigorous vortical flow and full attached flow causes strong trailing edge vortex shedding. Compared to the maximum portion of wavy designs, the curved trailing edge (almost rounded trailing edge at a certain location) of 10%c less portion wavy designs stimulates the flow separation only at a very limited area.

Eventually, the properly designed span-wise wavy trailing edge is predicted to reduce the sectional drag by 60% and results in increasing the L/D about

100% at high angle of attack (12°).

In the next section, acoustic characteristics of the span-wise wavy trailing edge designs were investigated and discussed. Based on the 1/3 octave band filtered Sound Pressure Level (SPL) results, properly designed wavy trailing edges reduce the low and high frequency tonal noise (low: 120dB - 125Hz, high: 103dB - 400Hz) of the plain flatback trailing edge by -25dB and -23dB, respectively. Since in the current case, the tonal noise emission is directly related to the trailing edge vortex shedding (also source of pressure drag), aerodynamically the best wavy designs were aero-acoustically the best designs, too.

Compared to the add-on type drag and noise reduction devices, the span-wise wavy trailing edge reduces the drag the same as or slightly better than the best performance add-ons. Regarding to the disadvantages of add-on type devices (explained in Chapter 2), the idea of span-wise wavy trailing edge looks promising for the future wind turbine drag and noise reduction.

6. In Chapter 6, the best aerodynamic / aeroacoustic performance wavy trailing edge designs are applied as an inboard modification on the SNL100 meter blade, and simulated as an isolated rotor system. Power loss is observed at the inboard of the baseline blade (root - r/R 0.3), due to the massive flow separation at the region. Since the wavy trailing edge works with highly blunt trailing edge (no separation), there wasn't a notable performance improvement observed in this case.

To improve power performance at the inboard portion, its trailing edge was augmented by 50% of the original trailing edge thickness. The inboard trailing edge augmentation resulted in about 1.45% of total power increase (at the rated wind speed 11.3m/s). That is a significant power benefit, regarding Annual Energy Production (AEP).

A disadvantage of the trailing edge augmentation is, however an increase of tonal noise. 50% of trailing edge augmentation generated very low frequency (4Hz) tonal noise of about 35dB (in maximum). Adding the span-wise wavy trailing edge modification on the augmented trailing edge successfully reduced the tonal noise by -15dB (in maximum). In addition, the power generation also increased by reducing the pressure drag, thus a total 2.62% of power benefit was observed in the BWC (Blunt-Wavy Combined) trailing edge modified blade (at the rated wind speed 11.3m/s).

7.2 Observations

These are the main observations of the various studies.

- Parametric study
  - Wave sizing
    - Moderate flow separation is observed in the best aerodynamic and aero-acoustic performance wavy trailing edges.
    - Lift loss is proportional to the wave depth (deeper waves lose more lift), and very sensitive to the wave depth.

    * Wave length longer than 4 waves per chord length didn't affect much the lift and drag.
    * Drag reduction is proportional to the wave depth (deeper waves reduce more drag).
    * Drag reduction is proportional to the wave length between 12 and 4 waves per a chord length, but no longer depends on the wave length for longer wave length.
    * Between the two types of less portion wavy design, 10%c less portion wavy design is more efficient, regarding to the aerodynamic, aeroacoustic and structural performance.

– Aerodynamic performance
    * Aerodynamic performance of airfoils are strongly related to the trailing edge vortex structure.
    * Drag reduction of the properly designed wavy trailing edges is due to the breakup of Karman-like vortex structure and standing flow at the trailing edge.
    * Properly designed span-wise wavy trailing edge reduces at least 50% (maximum 60%) of drag while only 7% lift loss.
    * Properly designed span-wise wavy trailing edge increase maximum Lift/Drag ratio by 1.5-2.5 times compared to the plain flatback trailing edges.

– Aero-acoustic performance

    * Acoustic noise level is strongly related to trailing edge vortex structure.
    * Plain flatback trailing edge generates two major tonal sound (high frequency: 103dB at 400Hz, low frequency: 120dB at 125Hz)
    * Sound Pressure Level at the 3 chord length distance away from trailing edge, for a properly designed span-wise wavy trailing edge reduces both tonal sounds from the plain flatback trailing edge by 20 - 25dB(SPL).

- Isolated blade simulations
  - DDES of baseline blade
    * Massive inboard separation is a main noise source of the original blade
    * Strong broad band noise is observed at the blade inboard.
    * Notable amount of power loss is observed at the blade inboard, from r/R 0.1 to 0.3
  - DDES of wavy trailing edge modified blade
    * Less than 2% of power loss with span-wise wavy trailing edge modification
    * Blunt trailing edge of the original blade is not enough to prevent inboard separation
    * Massive inboard separation is main noise source of the wavy only

modified blade

* Most of high magnitude acoustic noise emitted less than 20Hz (very low frequency region)

– DDES of augmented (Blunt) trailing edge blade

* Appropriate Blunt trailing edge augmentation is 50% thickness increase from r/R 0.1 to 0.3.
* 50% augmented trailing edge prevents inboard separation, but strong trailing edge vortex shedding occurs
* Tonal noise at 7 and 12Hz appears because of the strong trailing edge vortex shedding
* Power generation due to the inboard augmented trailing edge increased by 1.45% compared to the original blade, due to the delay of flow separation

– DDES of Blunt-Wavy Combined(BWC) trailing edge blade

* Blunt with 2W-75%t-10%c modification shows better noise reduction, but not much power improvement.
* Blunt with 4W-75%t-10%c modification prevents massive flow separation very well, but weak trailing edge vortex shedding still exist.
* Best aerodynamic combination (50% augmentation + 4W-75%t-10%c) increases rotor power by 2.62% compared to the original blade.
* Best aero-acoustic combination (50% augmentation + 2W-75%t-10%c) results in 30-50dB of tonal noise reduction compared to the blunt only

trailing edge modification

7.3 Contributions

The current study may contribute to the future study of wind turbine aerodynamics and aero-acoustics, as listed below.

- Proposed new idea of low noise treatment (non add-on) for modern large wind turbine blade (Blunt-Wavy trailing edge modification).
- Design parametric study of the span-wise wavy trailing edge design.
- Provided physical and fundamental understandings of flatback / wavy trailing edge flow.
- Quantification of the best aerodynamic and acoustic performance wavy trailing edge airfoil.
- First attempt of RANS-LES hybrid simulation for over 100 meter length turbine blade (using SNL100 series).
- Provided aerodynamic and acoustic characteristics of flatback / wavy trailing edge wind turbine blade.
- GPU-accelerated computation for the 3-D turbine simulations.

7.4 Future Works

There are many potential future works would be considered.

First of all, the parametric study and its aerodynamic and acoustic analysis performed in the current study can be extended to much broader and larger kinds of airfoils and flow regimes. In the current study, the parametric study is performed for the FB3500-1750 airfoil only. To make the results more generally accepted, similar investigations for other flatback airfoils must be a good suggestion. In the meantime, relevant investigations in the different Mach number ranges could be also interesting.

Secondly, numerical simulation of the full turbine configuration including more realistic ABL (Atmospheric Boundary Layer) inflow and acoustic noise measurement at the further distance from the turbine must be a exiting future work. One limitation of the current isolated blade simulation is that the potential interactions between the wavy trailing edge and the other turbine configurations are remained as unknown. Also, since the current study focuses the noise level near the blades rather than the noise propagated to the further distance, this future work will provide the data which can be used in the practical turbine sitting projects.

Thirdly, the other limitation (better to be called an obstacle) of the current work is no experimental data was available. Although the numerical solver was validated with the experimental data for the flatback case (baseline case), no wind tunnel experiment data for the wavy trailing edge was available. Comparison between the wind tunnel data and the current numerical data will enhance the conclusions of the current study, and will give more credibility to the new trailing edge design.

Appendix A: Structural Concerns

A.1 Potential Structural Issues

There might be concerns about structural uncertainties of the proposed spanwise wavy trailing edge design. In this chapter, structural characteristics of the wavy modified SNL100-03FB blade have been discussed. As we discuss in Chapter 1 and 2, wind turbine blade inboard is the most important region in a blade structure design. Thus, any significant modification on the region will changes its structural characteristics or may cause a failure of the structure. Regarding this fact, blade geometry changes at inboard is better to be minimized and avoided changing blade spar regions. Among the proposed wavy trailing edge designs, the 75%t-10%c less portion wavy design requires the minimum changes on the original blade, and does not change any of the blade spar regions.

To examine probability of potential structural failure, the maximum deformation and linear eigen bucking test have been conducted.

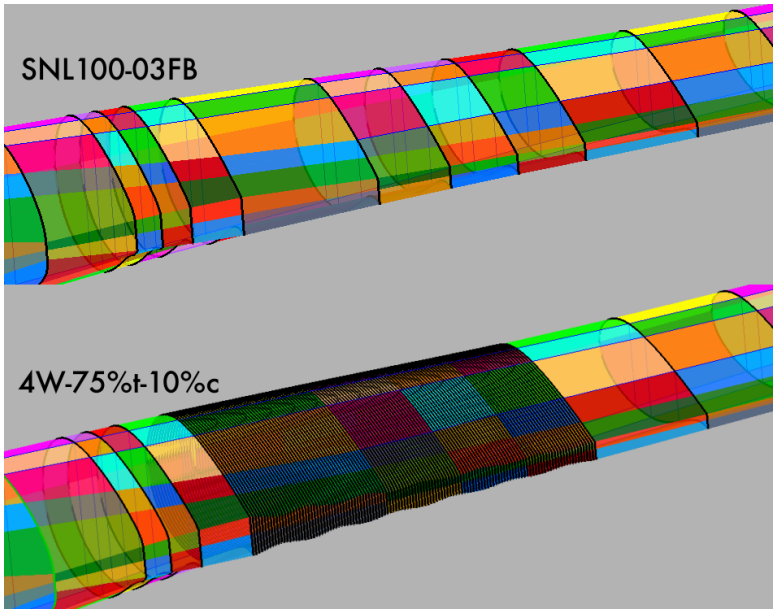

Figure A.1: Span-wise wavy trailing edge modification of the SNL100-03FB blade NuMad modeling

A.2 Structure Dynamics Test

The modified blade geometry and numerical solver input parameters have been created using NuMad software, which has been developed by Sandia National Lab. NuMad model geometries of the original SNL100-03FB and its wavy modified version of blade are shown in Figure A.1.

The same modified region and wave shape with the aerodynamics simulations have been applied to the structural analysis model. The Ansys APDL(Ansys Parametric Design Language) mechanical solver has been used for the current study. The aerodynamic force loadings on the blade model have been mapped as presented in Figure A.2. The two lines of forces have been applied on the blade. Normal forces

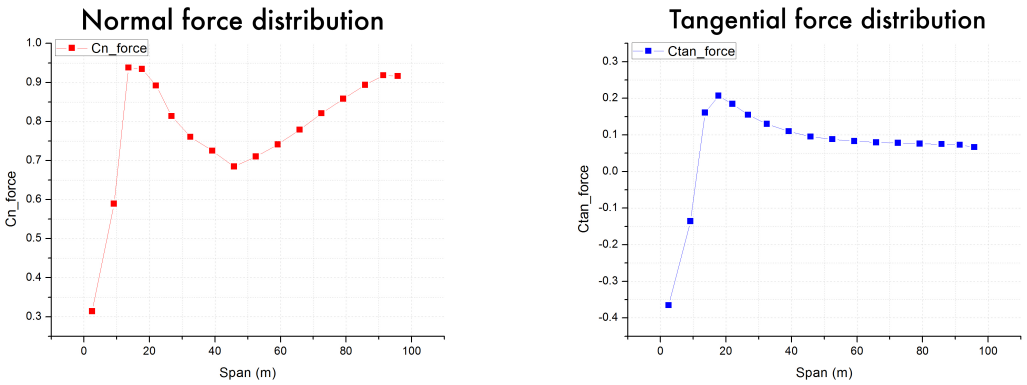

Figure A.2: Normal and tangential line force distribution on blade span

acting on the rotation plane have been applied on the spar cap where the shear web locates, and tangential forces acting on the rotation plain have been applied on the leading edge of the blade. The aerodynamic forces have been calculated using Aerodyn V15, the BEMT(Blade Element Momentum Theory) solver developed by Sandia National Lab. In the analysis, the blade rotation speed assumed as 9.5rpm, and the incoming wind speed set as 11.3 m/s. The open source original SNL100-03 model file has been used in the current study, and the turbine operation conditions have been set as much as same with Griffiths research [2]. Thus, as a reference, for the original SNL100-03 blade case, we only tried to duplicate his buckling result in the study.

A.2.1 Deformation

Maximum deformations of the original SNL100-03FB and wavy trailing edge modified blade are tested. No pre-bending on the blade design is assumed. Figure

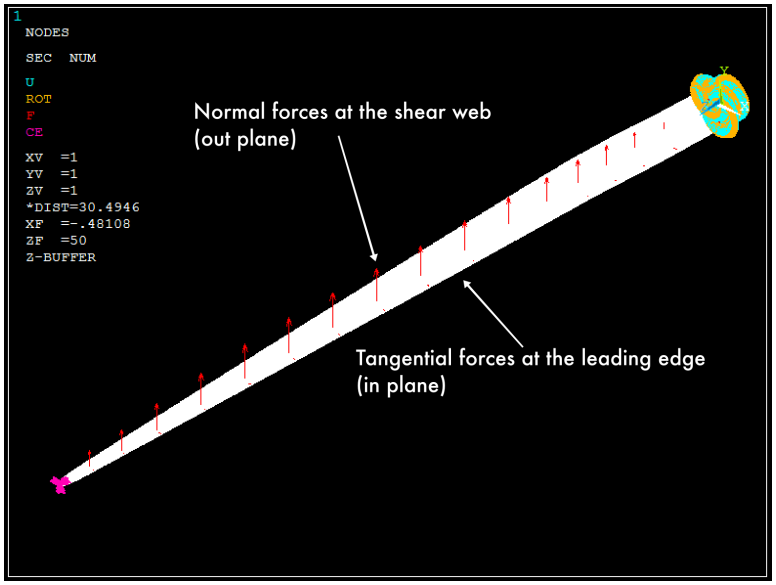

Figure A.3: Normal and tangential line force loading on the SNL100-03FB blade

A.4 and A.5 show maximum tip deflection of the blades. In Figure A.4, the maximum tip deflection of the original blade is approximately 6.5714 meter. In Figure A.5, the maximum tip deflection of the modified blade is approximately 6.5766. This is almost identical result between two blades. In addition, notable deflection begins at about 50% span on the both blades. Recalling the current wavy trailing edge modification plans, the modification will apply on the rest half of the blade span (where the deflection doesn't affect significantly).

A.2.2 Eigen Buckling

Eigen buckling analysis results have been presented in Figures A.6 and A.7. The lowest mode buckling results of the two blade models are nearly identical to each other, and also identical with Griffiths results [2]. Both the original SNL100-03

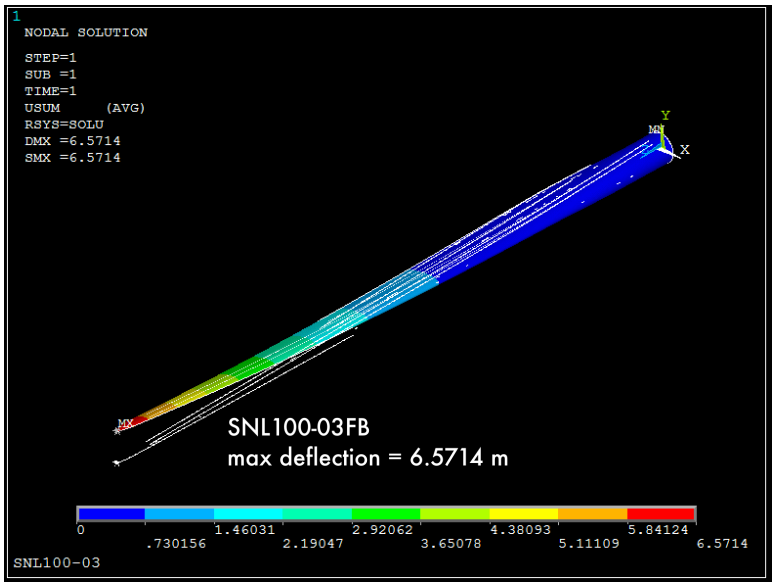

Figure A.4: Maximum tip deflection of the SNL100-03FB blade

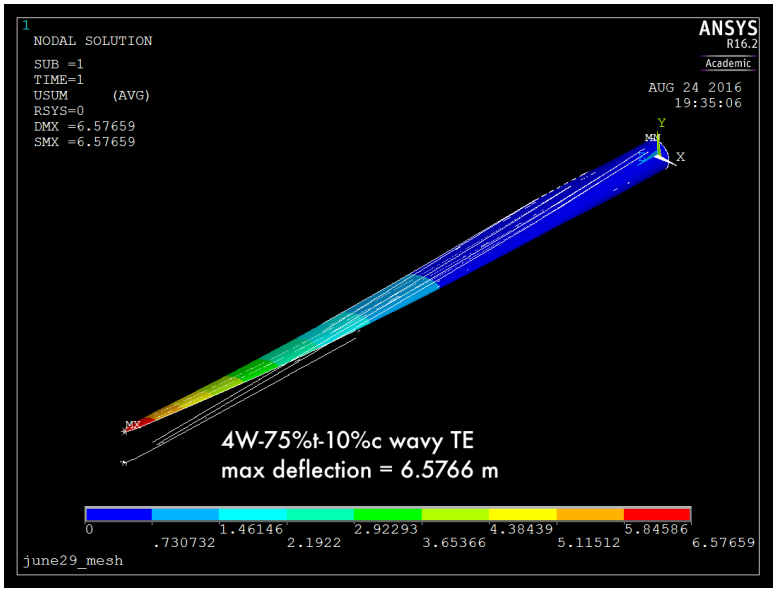

Figure A.5: Maximum tip deflection of the wavy trailing edge modified blade

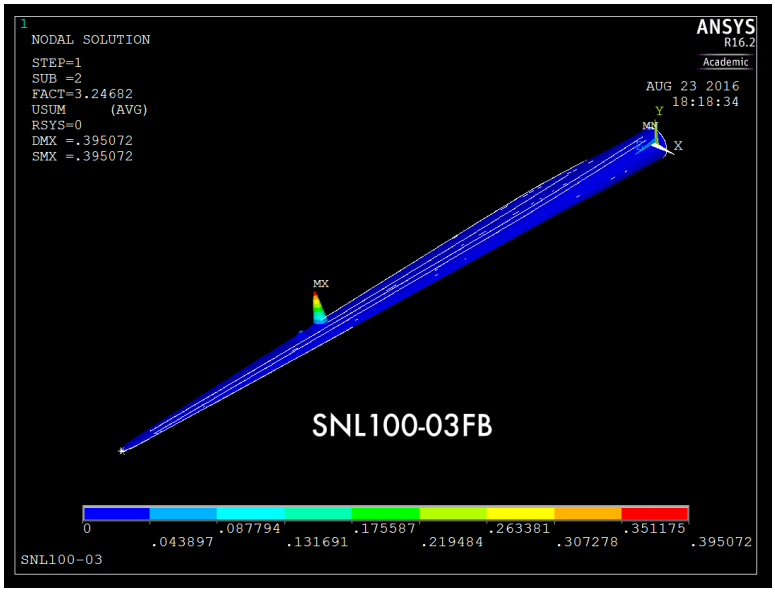

Figure A.6: Eigen Buckling of the SNL100-03FB blade

and the modified blade buckle at the blade outboard of mid span region, where the third shear web ends. Nonetheless, despite concerns of the structural failure at the wavy modified area, no significant buckling failure at the wavy modified region has been observed in the current study.

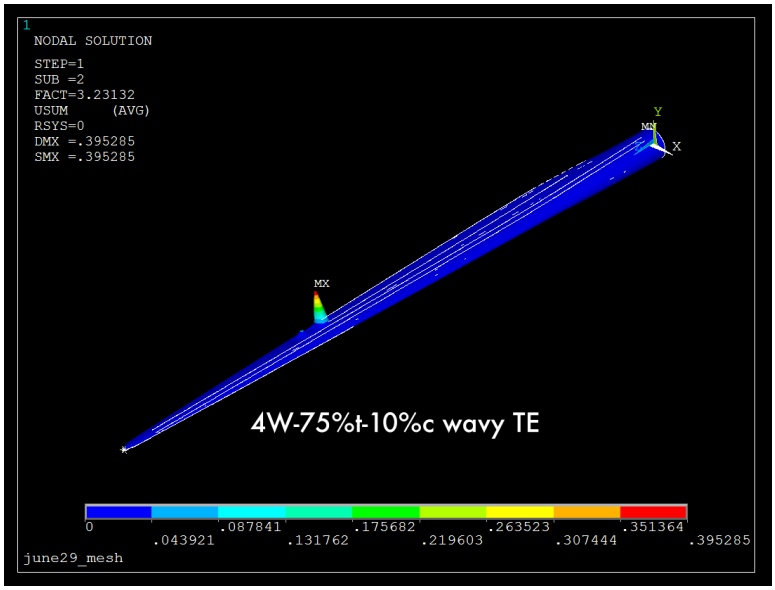

Figure A.7: Eigen Buckling of the wavy trailing edge modified blade

Bibliography

[1] R. Wiser and M. Bolinger, "2016 Wind Technologies Market Report: Summary," Office of Energy Efficiency and Renewable Energy, U.S. Department of Energy (2017).

[2] D.T. Griffith and P.W. Richards, "The SNL100-03 Blade: Design Studies ith Flatback Airfoils for the Sandia 100-meter Blade," Sandia Report, SAND-2014-18129, Sandia National Laboratory (2014).

[3] D. Lekou, D. Chortis, P. Chaviaropoulos, X. Munduate, A. Irisarri, H.Aa. Madsen, K. Yde, K. Thomsen, M. Stettner, M. Reijerkerk, F. Grasso, R. Savenije, G. Schepers, and C.F. Anderson, "AVATAR Deliverable D1.2 Reference Blade Design", AVATAR Deliverable D1.2, ECN Wind Energy (2015)

[4] "HALIADE-X OFFSHORE WIND TURBINE PLATFORM", https://www.ge.com/renewableenergy/wind-energy/turbines/haliade-x-offshore-turbine.

[5] J.F. Manwell, J.G. McGowan and A.L. Rogers, *Wind Energy Explained: Theory, Design and Application* (John Wiley & Sons, Ltd., 2011).

[6] F. Grasso, "Development of Thick Airfoils for Wind Turbines," 50th AIAA Aerospace Science Meeting, Nashville, Tennessee (2012).

[7] A. Munoz, B. Mendez and X. Munduate, "Thick airfoil designs for the root of the 10MW INNWIND.EU wind turbine," Journal of Physics: Conference Series 753 022046 (2016)

[8] J. Jonkman, S. Butterfield, W. Musial, and G. Scott, "Definition of a 5-MW Reference Wind Turbine for Offshore System Development," Technical Report, NREL/TP-500-38060, NREL (2009).

[9] D.T. Griffith and T.D. Ashwill, "The Sandia 100-meter All-glass Baseline Wind Turbine Blade: SNL100-00," Sandia Report, SAND-2011-3779, Sandia National Laboratory (2011).

[10] A. Roshko, "On the drag and shedding frequency of two-dimensional bluff bodies," NACA TN-3169 (1954).

[11] A. Roshko, "On the wake and drag of bluff bodies," Journal of Aerospace Science, Vol.22, pp.124-132 (1955).

[12] J.F. Nash, V.G. Quincy and J. Callinan, "Experiments on two-dimensional base flow at sub-sonic and transonic speeds," Aeronautical Research Council Report and Memoranda, No.3427 (1963).

[13] J.F. Nash, "A Discussion of Two-Dimensional Turbulent Base Flows," Aeronautical Research Council Report and Memoranda, No.3468 (1967).

[14] S.F. Hoerner, *Fluid Dynamic Drag* (Hoerner Fluid Dynamics, Chapter III.8.Base Drag (1965)).

[15] J.P. Baker, E.A. Mayda, and C.P. van Dam, "Experimental Analysis of Thick Blunt Trailing-Edge Wind Turbine Airfoils," ASME Journal of Solar Engineering, Vol.128, pp.421-423 (2006).

[16] O. Edenhofer, R. Pichs-Madruga, Y. Sokona, K. Seyboth, P. Matschoss, S. Kadner, T. Zwickel, P. Eickemeier, G. Hansen, S. Schlomer, and C. von Stechow, "2011: IPCC Special Report on Renewable Energy Sources and Climate Change Mitigation," prepared by Working Group III of the Intergovernmental Panel on Climate Change, Chapter. 7 Wind Energy, Cambridge University Press, Cambridge, United Kingdom and New York, pp.575, New York (2011).

[17] I.J. Onakpoya, J. O'Sullivan, M.J. Thompson, and C.J. Heneghan, "The effect of wind turbine noise on sleep and quality of life: A systematic review and meta-analysis of observational studies," Environment International 82, pp.1-9, Elservier (2015).

[18] S. Oerlemans and P. Fuglsang, "Low-noise wind turbine design," EWEA Noise Workshop, Oxford (2012).

[19] T.F. Brooks, D.S. Pope, and M.A. Marcolini, "Airfoil Self-Noise and Prediction," NASA Reference Publication 1218, NASA Langley Research Center (1989).

[20] M. Tanner, "Reduction of Base Drag," Aerospace Sci. 1975, Vol.16, No.4, pp.369-384 (1975).

[21] C.P. van Dam, D.L. Kahn, and D.E. Berg, "Trailing Edge Modifications for Flatback Airfoils," Sandia Report, SAND-2008-1781, Sandia National Laboratories (2008).

[22] M.F. Barone and D. Berg, "Aerodynamic and Aeroacoustic Properties of a Flatback Airfoil: An Update," 47th AIAA Aerospace Science Meeting Including The New Horizon Forum and Aerospace Exposition, Orlando, Florida, AIAA-2009-0273 (2009).

[23] P.J. Schubel and R.J. Crossley, "Wind Turbine Blade Design," Energies 2012, 5, pp.3425-3449, ISSN 1996-1073 (2012).

[24] R. Gasch and J. Twele *Wind Power Plants* (Solarpraxis, Berlin, Germany, 2002).

[25] T. Burton *Wind Energy Handbook* (John Wiley & Sons Ltd., Chichester, UK, 2011).

[26] P.W. Bearman, "Investigation of the flow behind a two-dimensional model with a blunt trailing edge and fitted with splitter plates," Journal of Fluid Mechanics, Vol.21, Part 2, pp.241-255 (1965)

[27] J.P. Baker, C.P."Case" van Dam, and B.L. Gilbert, "Flatback Airfoil Wind Tunnel Experiment," Sandia Report, SAND-2008-2008, Sandia National Laboratories (2008).

[28] D.C. Hazen, R.F. Lehnert, T.E. Sweeny and F.O. Ringleb, "Preliminary report on circulation control by means of trailing edge suction and the cusp effect," Princeton University, Aeronautical Engineering Report 234 (1953).

[29] M.J. Molezzi, and J.C. Dutton, "Study of Subsonic Base Cavity Flowfield Structure using Particle Image Velocimetry," AIAA Journal, Vol.33, No.2, pp.201-209 (1995).

[30] P.J. Deshpande and S.D. Sharma, "Spanwise vortex dislocation in the wake of segmented blunt trailing edge," Journal of Fluids and Structures, Vol.34, pp.202-217 (2012).

[31] R.F. Sargent, "Tests on NACA0012 with Various Thick Trailing Edges at High Speeds," Aeronautical Research Council Report and Memoranda, No.2209 (1942).

[32] F.E. Fish, P.W. Weber, M.M. Murray, and L.E. Howle, "The Tubercles on Humpback Whales," Flippers: Application Bio-inspired Technology, Vol.51, No.1, pp.203-213, Salt Lake City, UT (2011).

[33] C. Cai, Z. Zuo, and S. Liu, "Numerical Investigation of Hydrodynamic Performance of Hydrofoils with Leading-edge Protuberances," Advances in Mechanical Engineering, Vol.7,pp.1-11 (2015).

[34] P.R. Spalart, W.H. Jou, M.K. Strelets, and S.R. Allmaras, "Comments on the Feasibility of LES for Wings, and on a Hybrid RANS/LES Approach," 1st AFOSR International Conference on DNS/LES (invited), (1997).

[35] P.R. Spalart, S. Deck, M.L. Shur, K.D. Squires, M.K. Strelets, and A. Travin, "A new version of detached-eddy simulation, resistant to ambiguous grid densities," Theoretical and Computational Fluid Dynamics, Vol.20, No.3, pp.181-195, (2006).

[36] P.R. Spalart and S.R. Allmaras, "A One-Equation Turbulent Model for Aerodynamic Flows," La Rech. Aerosptiale 1, pp.5-21 (1992).

[37] S. Medida and J.D. Baeder, "Application of the Correlation-based $\gamma - \overline{Re_{\theta t}}$ Transition Model to the Spalart-Allmarass Turbulent Model," 20th AIAA Computational Fluid Dynamics Conference, Honolulu, HI (2011).

[38] S. Medida and J.D. Baeder, "Adverse pressure gradient modification to turbulence models for wall-bounded flows," 21th AIAA Computational Fluid Dynamics Conference, AIAA paper 2013-2426 (2013).

[39] F.R. Menter, "Zonal Two Equation $k - \omega$ Turbulent Models For Aerodynamic Flows," 24th AIAA Fluid Dynamics Conference, Orlando, FL (1993).

[40] R.B. Langtry and F.R. Menter, "Correlation-Based Transition Modeling for Unstructured Parallelized Computational Fluid Dynamics Codes," AIAA Journal, Vol.47, No.12, pp.2894-2906, (2009).

[41] T. Reinhart, "Contributions to the Understanding of Wind Turbine Aerodynamics Using a RANS Solver with Transition Modeling," MS Thesis, University of Maryland (2014).

[42] T. Reinhart, S. Medida, S. Thomas, and J.D. Baeder, "Computation of Two-dimensional Wind Turbine Airfoil Characteristics Using Advance Turbulence and Transition Modeling Methods and a GPU-Accelerated Navier-Stokes Solver," 32nd ASME Wind Energy Symposium at SciTech 2014, National Harbor, MD, AIAA-2014-1216 (2014).

[43] S. Thomas, "A GPU-accelerated, Hybrid FVM-RANS Methodology for Modeling Rotorcraft Brownout," PhD Thesis, University of Maryland (2013).

[44] "Deepthought2 HPC cluster," http://www.glue.umd.edu/hpcc/dt2.html

[45] "NVIDIA, TESLA K20 GPU ACCELERATOR," Board Specification, NVIDIA (2012).

[46] B. Van Leer, "Towards the ultimate conservative difference scheme. V. A second-order sequel to Godunovs method," Journal of Computational Physics, Vol.32, Issue 1, pp.101-136 (1979).

[47] B. Koren, "A robust upwind discretisation method for advection, diffusion and source terms," Numerical Methods for Advection-Diffusion Problems, Braunschweig, Vieweg, pp.118, ISBN 3-528-07645-3 (1993).

[48] S. Yoon and A. Jameson, "Lower-Upper Symmetric-Gauss-Seidel Method for the Euler and Navier-Stokes Equations," AIAA Journal, Vol.26, No.9, pp.1025-1026 (1988).

[49] P.L. Roe, "Approximate Riemann Solvers, Parameters Vectors, and Difference Schemes," Journal of Computational Physics, Vol.43, pp.357-372 (1981).

[50] E. Turkel, "Preconditioned Methods for Solving the Incompressible and Low Speed Compressible Equations," Journal of Computational Physics, Vol.72, pp.277-298 (1987).

[51] T. Kalra, CFD Modeling and Analysis of Rotor Wake in Hover Interacting with a Ground Plane, Ph.D. Dissertation, Department of Aerospace Engineering, University of Maryland at College Park (2014).

[52] "Aeronautical Wind Tunnel Specifications and Schematics," Mechanical and Aerospace Engineering, UC-Davis, https://flight.engr.ucdavis.edu/facilities/aeronautical-wind-tunnel/

[53] D.A. Corson, D.T. Griffith, T. Ashwill and F. Shakib, "Investigating Aeroelastic Performance of Multi-MegaWatt Wind Turbine Rotors Using CFD," 53rd AIAA/ASME/ASCE/AHS/ASC Structures, Structural Dynamics and Materials Conference, Honolulu, Hawaii, AIAA-2012-1827 (2012).

[54] R. Chow and C.P. van Dam, "Computational investigations of blunt trailing-edge and twist modifications to the inboard region of the NREL 5MW rotor," Wind Energy, Vol.16, pp.445-458, DOI: 10.1002/we.1505 (2013).

[55] J.C. Berg, J.A. Paquette and B.R. Resor, "Mapping of 1D Beam Loads to the 3D Wind Blade for Bucking Analysis," 52nd AIAA/ASME/ASCE/AHS/ASC Structures, Structural Dynamics and Materials Conference, Denver, Colorado, AIAA-2011-1880 (2011).